Title
Biomimetic Synthesis of Noble Metal Nanoparticles and Their Applications as Electrocatalysts in Fuel Cells

Author
Li, Yujing

Publication Date
2012

Peer reviewed|Thesis/dissertation

UNIVERSITY OF CALIFORNIA
Los Angeles

Biomimetic Synthesis of Noble Metal Nanoparticles and Their Applications as Electro-catalysts in Fuel Cells

A dissertation submitted in partial satisfaction of the
requirements for the degree Doctor of Philosophy
in Materials Science and Engineering

by

Yujing Li

2012.

ABSTRACT OF THE DISSERTATION

Biomimetic Synthesis of Noble Metal Nanoparticles
and Their Applications as Electro-catalysts in Fuel Cells

by

Yujing Li

Doctor of Philosophy in Materials Science and Engineering
University of California, Los Angeles, 2012
Professor Yu Huang, Chair

Today, proton electrolyte membrane fuel cell (PEMFC) and direct methanol fuel cell (DMFC) are attractive power conversion devices that generate fairly low or even no pollution, and considered to be potential to replace conventional fossil fuel based power sources on automobiles. The operation and performance of PEMFC and DMFC depend largely on electro-catalysts positioned between the electrode and the membranes. The most commonly used electro-catalysts for PEMFC and DMFC are Pt-based noble metal nanoparticles, so catalysts share close to 50% of the total cost of the fuel cell. The synthesis of such nanoscale electro-catalysts are commonly limited to harsh conditions (high temperature, high pressure), organic solvent, high amount of stabilizing agent, to achieve the size and morphological control. There is no rational guideline for the

selection of stabilizing agent for specific materials, leading to the current "trial and error" approach in selecting stabilizing agent.

This dissertation initially explores a new way to select material-specific stabilizing agents for the synthesis of the noble metal nanoparticles. With the help of phage display (PD) technique, a rational biomimetic approach can be used to select biomolecule (peptide) that specifically recognizes the surface of targeted material (use Pt as a case-study for this dissertation), and the selected peptides can be used as stabilizing agent to synthesize monodispersed Pt nanoparticles with tunable morphologies under mild synthetic conditions (atmospheric room temperature, aqueous solution). With fairly easy processing, the nanoparticles can be used as high surface area cathode electro-catalyst in fuel cells.

With the as-synthesized Pt nanoparticles, bimetallic nanoparticles containing Pt can be prepared for more electro-catalytic applications, such as the oxygen reduction reaction at the cathode of fuel cells, and the oxidation of methanol at the anode in DMFC. The materials synthesized include heterogeneously structured Pt-Pd core-shell nanoparticles, and homogenerously alloyed PtRu nanoparticles. The Pt-Pd core-shell nanoparticles, with Pd shell thickness controlled with atomic-layer precision, show almost 3-fold enhancement in catalytic activity for the ORR as well as better catalytic performance in oxidation of methanol, compared with commercially available catalysts. A specialized electrochemical tool, rotating disk electrode, is used to study the fundamental kinetics and their quantified catalytic activities in ORR. The seed-mediated synthesis of hyperbranched PtRu nanoparticles demonstrates the possibility of low-temperature

synthesis of well-alloyed material, and shows the enhanced catalytic activity in methanol oxidation compared with commercial catalysts, with its special formation mechanism studied.

The dissertation of Yujing Li is approved.

Bruce S. Dunn

Selim Senkan

Suneel Kodambaka

Yu Huang, Committee Chair

University of California, Los Angeles

2012

Table of Contents

List of Figures

List of Tables

Acknowledgments

I am profoundly grateful for all those people who provided their support throughout my Ph.D. at the University of California Los Angeles (UCLA).

I would like to thank my advisor Prof. Yu Huang for her remarkable guidance, support and continuous encouragement throughout my Ph.D. life at UCLA. Her enthusiasm and encouragement make her not only a great scientist but also a nice mentor to work with. Her keen scientific insights were indispensable for this dissertation and will always be a source of inspiration for my future career. On top of this, I have to thank Prof. Yu Huang for helping me keep faith in myself even at the most difficult moments. I feel really lucky to have her as my advisor.

I would also like to thank Prof. Bruce Dunn, Prof. Selim Senkan, and Prof. Suneel Kodambaka for serving my dissertation committee. I am very grateful for all the advice and support from them during my Ph.D. study. I also want to express my thanks to Prof. Xiangfeng Duan, Prof. Z. Hong Zhou, Prof. Yi Tang, Prof. Yunfeng Lu, Prof. Tatiana Segura, and Prof. Andrea M. Kasko from UCLA, Prof. Hong Yang from Rochester University (currently at University of Illinois at Urbana-Champaign), Prof. Xiaowei Teng from University of New Hampshire, Prof. Christopher B. Murray from University of Pennsylvania, Prof. Younan Xia from Washington University in St. Louis (currently at Georgia Institute of Technology), Prof. Jim DeYoreo and Dr. Roger Qiu from Lawrence Livermore National Laboratory, and Prof. Richard E Palmer from University of Birmingham, for their helpful suggestions or discussions during my Ph.D. study.

There are many collaborators to whom I would like to express my gratitude here. I was lucky to have Dr. Zheng Chen, Xiaolei Wang, Dr. Li-Min Chen, Wenbin Yang, Dr. Ignacio Martini, Marcus Yambot, Helena Chia, Dr. Donald R. Griffin, Dr. Jason Forse, Dr. Yanran Li, Dr. Kangjian Qiao, Dr. Xinkai Xie, Dr. Qi Chen, Dr. Jianbo Wu, Ivo Atanasov, Hoi Hui Wong, Dr. Xing Zhang, Dr. Sergey Ryazantsev, Dr. Matthew Mecklenburg, Dr. Talar Tokatlian, Jonathan Lam, Dr. Lei Liao, Dr. Yongquan Qu, Dr. Zhiwei Wang, and Xiaolu Kou work with. I really enjoyed working with these commendable colleagues and wish my best for their goals.

I would like to acknowledge all the group members in Prof. Huang's lab, including current members Dr. Xiaoqing Huang, Chin-Yi Chiu, Lingyan Ruan, Yu Chen, Yongjia Li, Kayla Roeser, Nathan Weiss, Hua Zhang, Teng Xue, Enbo Zhu, and Hao Wu, and former group members Dr. Leyu Wang, Dr. Jingwei Bai, Dr. Yung-Chen Lin, Gordon Whyburn, and Dr. Di Xu.

I want to acknowledge the funding sources that sponsored my Ph.D. research, which include Office of Naval Research (ONR), Army Research Office (ARO), and Center on Functional Engineered and Nano Architectonics (FENA), California NanoSystems Institute (CNSI).

I have been very lucky to have supportive and loving family members. I appreciate my parents, Suoming Li and Zhenping Wang, and their constant support and love from China. The person who also deserves my gratitude the most is my fiancee, Shan Xu. She has seen my worst moment but kept encouraging me and helping me in every possible

way, more amazingly, during such a long time with such a long distance across the Pacific Ocean. Without them, I would have no chance to accomplish this.

VITA

Yujing Li was born in Jiangsu Province, China. After completing his high school study in hometown, he entered the Department of Chemical Engineering of Tsinghua University in 2003, majoring in Polymer Materials and Engineering. In 2007, he received his Bachelor's degree in Materials Science and Engineering, and started his graduate study in the Department of Materials Science and Engineering, at University of California-Los Angeles. He immediately joined Prof. Yu Huang's research group ever since, and advanced to the doctoral candidate in November of 2008. During the graduate study in UCLA, he focused his research on the biomimetic synthesis of noble metal nanoparticles and their applications as electro-catalysts in fuel cell studies.

Education

University of California, Los Angeles Sep. 2007-June, 2012
Materials Science and Engineering
Ph.D. in Material Science and Engineering

Tsinghua University Aug. 2003-July, 2007
Chemical Engineering
B.S. in Polymer Material and Engineering

Chapter 1

1 INTRODUCTION

1.1 Synthesis of noble metal nanoparticles

In the past two decades, the trends of using 0-dimensional (0-D, nanoparticles), 1-D (nanowires, nanotubes, etc.), and 2-D (thin film, graphene, etc.) nanoscale materials in our real life, for example the electric, photonic, catalytic, thermoelectric, magnetic, and plasmonic applications, have attracted enormous interests from both the academia and industries.[1-7] Besides, when the lithography-based "top-down" approach has gradually reached its limit in creating patterns in the deep nanometer regime, the "bottom-up" approach, with which material structures are hierarchically assembled from individual nanoscale building blocks, can circumvent the limitations of lithography and lead to the formation of functional nanosystems with molecular precision. Up to now, 0-Dimensional nanoparticles (NPs), including metallic, metal oxide, semiconducting, and rare-earth-containing NPs, are considered as the most potential nanoscale materials to be incorporated in real products, due to the easiness of preparation, mass production and processing, as well as well-established property database.[8-12]

Among these various materials, the study of noble-meta-based NPs is an important branch because of their superior performances in catalysis, especially the Platinum (Pt)-based NPs that show excellent catalytic activities in organic synthesis, elimination of pollution-inducing gases, oil refining, and conversion of fuel molecules for the fuel cell applications.[13]

The synthesis of noble metal NPs have attracted chemists for the last several decades and recently emerged as an important field especially during the past two decades with the help of the fast development of advanced microscopic tools such as the transmission electron microscope (TEM), scanning electron microscope (SEM), and atomic force microscope (AFM), scanning tunneling microscope (STM), etc. which can visualize the structures in 2-D or 3-D in nanoscale or even sub-nanoscale. With these tools, it becomes easier for the scientists to understand formation mechanism, e.g. how synthetic conditions affect the growth, of NPs, so that it is possible to obtain more elaborate control over the sizes, morphologies, or structures of the NPs. For now, the understanding of the synthesis is far from the capability to explain the evolution pathways that a precursor compound may take to form metal atoms, nuclei, and then well-defined NPs at the atomic level. So at the current stage, compared with the development of classical and quantum physics, the synthesis of metal NPs remains an art rather than a science considering the limited generally accepted fundamental knowledge we have on growth mechanism of NPs. As a result, intensive efforts have been devoted to the exploration of how NPs evolve from atoms to nanoscale particles.

Borrowing the classical crystallization theory developed for bulk materials, the growth of noble metal NPs can be described in a typical process with three distinct stages: 1) nucleation, 2) nuclei into seeds, and 3) growth of seeds into NPs.[14] Due to the small size of the nuclei as well as the difficulty of capturing them, only seeds and well-developed NPs can be observed with electron microscope (EM). More recently, with the development of technologies in in-situ observations in TEM, special TEM sample cells can be designed to observe objects in solution. In this way, the formation of noble metal

NPs in solution can be directly visualized under TEM, which is one of the most important progresses in the synthesis study of NPs.[15,16] However, there is still a long way to go before a systematic theory can be developed as a guideline for the synthesis of NPs.

Currently, two types of noble metal NPs have been widely studied, mono-metallic NPs such as Pt, Pd, Ag, Au, Rh, etc., and multi-metallic NPs including alloy NPs such as PtPd, PtRu, PtAu, and PtNi, etc., and heterogeneously structured NPs such as core-shell and dumbbell structures.

1.1.1 Synthesis of mono-metallic nanoparticles and bimetallic nanoparticles

The synthesis of mono-metallic NPs usually starts with a precursor containing the metal species, commonly a salt, or an organometallic precursor dissolved in a solvent. If salt precursor is used, metal atoms are commonly extracted by using reducing agent. Commonly used reducing agent are sodium borohydride ($NaBH_4$), hydrazine (N_2H_4), (H_2), and carbon monoxide (CO), which are strong reductants, or polyol, ascorbic acid, citric acid, polyvinylpyrrolidone (PVP), etc, which are weak reductants, depending on the activity of the precursors, nature of the solvent, and the expected properties of the NPs.[17-23] While if organometallic precursor is used, the reaction is usually conducted in organic solvent at elevated temperature to extract the metal atoms by thermal decomposition.[24] In addition, stabilizing agent is also necessary in a typical synthesis if one expects to avoid aggregation and obtain NPs well dispersed in reaction solution. Commonly used stabilizing agents are some charged small molecules such as halides (KBr, NaI), citric acid, phosphine or polarized long-carbon-chain molecules and polymeric molecules such as cetyltrimethylammonium bromide (CTAB), alkanethiol, oleic acid, PVP, polyacrylic

acid (PAA).[19,25-32] The use of stabilizing agent will be described in detailed in Section 1.1.2.

Two mechanisms are commonly accepted on how metal species form nuclei and grow into NPs. It used to be assumed that metal ions exist as monomeric units through complexation with anions, ligands, or solvent molecules, and metal atoms are then reduced from the complex and aggregated to form nuclei.[13] Basically, in this theory, metal atoms are reduced first and then incorporated into the nuclei, which we called a "reduction-incorporation" mechanism. Later on, another pathway was found when studying the nucleation process of Ag NPs with $AgNO_3$ as precursor in aqueous solution.[33] It was confirmed with mass spectrometry (MS) that $[Ag_3(NO_3)_2]^+$ is the stable intermediate specie towards nucleation, which means that Ag species are not in the atomic state before forming the nuclei. It was also discovered by simulation that in the synthesis of Pt NPs, the energy barrier is lower if Pt complexes (with water molecule and the anions) adsorb onto the Pt cluster first and then get reduced to zero valence directly on the surface, which we can call an "incorporation-reduction" mechanism.[34] In the synthesis, mechanisms vary from case by case, depending on the material system and the synthetic condition. So far, the two mechanisms can explain most of the phenomena, so they are both accepted by the academia.

The synthesis of mono-metallic NPs is relatively straightforward with the above mechanisms, so it has been studied for various metals including all noble metals the materials listed in Table 1.1.

Table 1.1 Commonly used precursors for the synthesis of different mono-metallic noble metal NPs.[13]

Metal	Precursors	Applications
Au	$HAuCl_4$, AuCl	Catalyst, biological sensing, Electronics, Nanomedicine
Ag	$AgNO_3$	Jewelry, Catalyst, Photography,
Pd	Na_2PdCl_4, $Pd(NO_3)_2$, $Pd(acac)_2$	H_2 storage, Catalytic converter
Pt	H_2PtCl_6, K_2PtCl_4, $Pt(acac)_2$	Catalyst, Jewelry
Rh, Ir, and Ru	MCl_3, $M_x(CO)_y$	Catalysts
Fe, Co, and Ni	M_xCl_y, $M_x(CO)_y$	Ferro-magnetism

To overcome the drawbacks of certain elements or incorporate more functionalities into the NPs, two or more elements can be used to synthesize multi-metallic NPs. The more elements it contains, the more functionalities the NP obtains, but the more complicate the system will be in terms of synthesis and analysis. In my work, two elements are involved at most, so only bi-metallic NPs are discussed here. Generally, this type of NPs can be divided into two groups: alloy NPs, and hierarchically-structured NPs.

For bimetallic alloy NPs, the synthesis is more complicate due to the different natures or properties of individual components. They can be synthesized either by co-reduction of both precursor salts, or reduction of one precursor salt followed by the thermal decomposition of the other precursor and then annealed at elevated temperature in order for two species to fully mix and achieve a high alloying degree.[35,36] For some particular

applications, such as magnetism, it requires chemically ordered lattice to achieve expected properties, which requires a further step of post-annealing to obtain chemically ordered crystalline structures. Currently, commonly studied noble metal based bimetallic alloy NPs are listed in Table 1.2 categorized for different applications.

Table 1.2 Commonly studied bimetallic NPs for different applications.

Types of bimetallic NPs	Applications
Pt-Ni, Pt-Co, Pt-Fe, Pt-Cu, Pt-Rh, Pt-Ir	Cathode catalysts in fuel cells.
Pt-Pd, Pt-Ru, Pt-Mn, Pt-Au, Au-Pd	Anode catalysts in fuel cells.
Fe-Pt, Co-Pt, Co-Ni	Magnetic materials.
Au-Ag, Au-Cu	Plasmonic/Optical applications

For bimetallic NPs with heterogeneous structures, the driving force of synthesizing these structures is that the properties can be appropriately predicted and easily tuned by manipulating the individual component as long as each component is well studied. But the synthesis is even more complicate due to the fact that the they are usually synthesized with a two-step approach.[37,38] Generally, depending on how the second component is incorporated, the final morphologies of the bimetallic NPs include: core@shell structures, dumbbell structures, etc.[39] For the core@shell NPs, the synthesis attracts the most interests because there are more parameters or factors that can be tuned. Depending on how the shell material is formed, enormous work has been done to obtain core@shell NPs with fully covering shell with thickness elaborated to the atomic level, or partially covering shell which forms only on certain facets or locations of the core particle.[40,41] For example, Ag and Au receive wide interests due to their superior plasmonic responses.

Large amount of work has been done to synthesize Ag@Au or Au@Ag core@shell NPs, firstly to take advantage of the well-established surface chemistry of the shell material, and secondly, to retain the physical property of the core material.[42,43] However, it is quite possible that the core@shell NPs can show distinctly different, sometimes dramatically enhanced, behavior compared with individual materials because of the change of crystalline structure, interaction of electronic structure, or the change of lattice induced by the strain at the interface.

1.1.2 Morphology control of metallic nanoparticles

It has been confirmed that for catalytic materials, the catalytic activity depends strongly on the atomic arrangement on the exposed facets because the atomic arrangement affects the adsorption of reacting molecules.[44] Besides, it has also been reported that the atoms at the corners and edges show higher catalytic activity because atoms at these locations may possess more dangling bond which make them more active in binding with reacting molecules. For NPs which have high surface-to-volume ratio, both factors, the atomic arrangement on the facets, and the ratio of atoms at corners and edges, depend on the morphology. For instance, for the tetrahedrons, cuboctahedrons, and cubes of 5 nm in size, the ratios of atoms located at corners or edges are 35%, 13%, and 6%, respectively. As a result, synthesizing NPs with uniform morphology is of great interest to many chemists.

It has been introduced in Section 1.1.1 that the formation of a NP experiences three stages: nucleation, seeding, and growth. Although some early works claimed that the morphology of the seeds determine the final shape of the NP, more recent studies show that with the same seeds, NPs can grow into various shapes, which actually indicates that

the morphology is determined in the growth stage. For noble metal NPs with face cubic centered (FCC) crystal structure, it has been confirmed that different low-index facets show an energetic sequence of $\gamma(111) < \gamma(100) < \gamma(110)$.[13] This sequence implies that a single-crystal seed should take an octahedral or tetrahedral shape in order to maximize the expression of (111) facets and minimize the total surface energy. It can also be illustrated with Wulff's theorem as shown in a 2-D case in Fig. 1.1, which can be simply described as that a thermodynamically stable NP should be exposed with facets that advance at the slowest rate.[45] For 3-D NPs, the evolution of morphology in the growth stage follows the same principle.

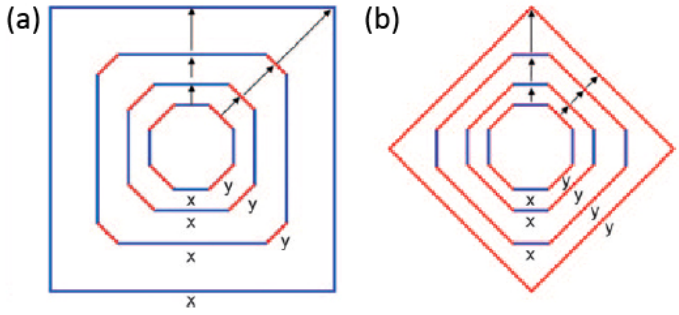

Figure 1.1 Shape evolution during the successive stages of growth for an imaginary 2-D crystal. (a) When y edges advance at a faster rate than x edges (advancing rate proportional to the length of the arrow), the final 2-D crystal will be enclosed with x edges. (b) vice versa.

The Wulff's theorem points out that it is the surface energies of different facets that determine the morphology of the NPs, in a thermodynamic-dominating environment, so if the surface energies can be modified, the morphology can also be tuned. Stabilizing agent is an important tool chemists use to modify the surface energy. It has been introduced that stabilizing agent can adsorb on the NP surface and lower the surface

energy to prevent the aggregation. However, for some stabilizing agents, their binding strength to different facets are distinctly different, which implies that they can lower the advancing rates of facets with different level. For example, Br- shows dramatically binding to (100) facet of Pd and lower its advancing rate dramatically, so that it produce Pd NPs with sharp cubic or rectangular morphologies.[25] As a result, looking for appropriate stabilizing agents or their combinations is an important objective for many chemists.

In addition, reaction conditions, such as temperature, precursors, and reductants, all of which can affect the kinetics of the reaction, can also be manipulated to tune the morphology of NPs.

1.2 Biomimetic synthesis of inorganic materials

Through millions-of-year evolution, nature has selected organisms that can create diversified and well-shaped structures with inorganic materials in nano- or micro-scale, which is known as biomineralization such as the calcification, silification in diatoms, and the formation of magnetite crystals in magnetotactic bacteria, as shown in Fig. 1.2.[46-48] These organisms are capable of organizing nano-scale building blocks into large scale hierarchical structures to form hard tissues serving different functions, such as the mechanical support, filtration, light harvesting, gravity sensing, and locomotion.[49-51] Scientists have long been exploring the approaches and mechanisms by which nature adopts with the hope to mimic and achieve the possibility of the bottom-up assembly scheme for technical applications.[52,53] In specific, in vitro biomimetic studies have revealed that the proteins play an important role in controlling the size and morphology of hard tissue minerals, as well as help controlling the biomaterial assembly through their

specific interactions with inorganic crystal surfaces evolved through millions of years.[54-56]

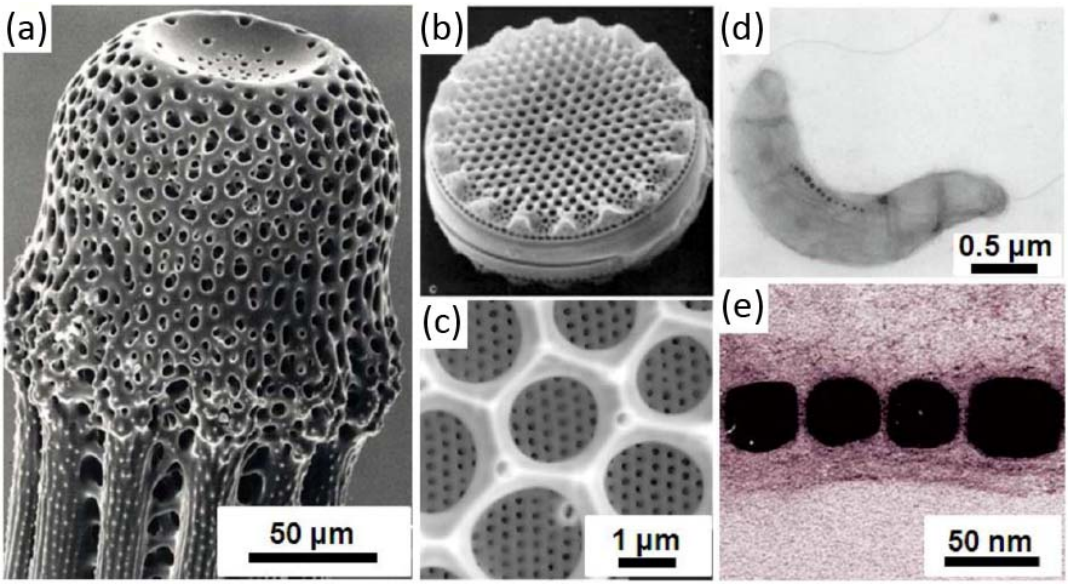

Figure 1.2 (a) Scanning electron micrograph (SEM) of a mature sea urchin spine, which is a composite of organic macromolecules and oriented $CaCO_3$ (calcite).[46] (b) SEM image of cell walls from diatom. (c) High magnification SEM image of diatom silica cell walls.[57] (d) A magnetospirillum gryphiswaldense cell. (e) Magnetite crystals observed at the ends of the chain in magnetotactic bacteria.[48]

1.2.1 Phage display technique

The biomolecules responsible for controlling the minerization of materials vary in their composition, conformation and origins.[58-61] The chemical and physical properties of biomolecules contribute to their unique specificity in binding on materials or mediating materials assembly.[62-64] To obtain the specific biomolecules, the most straightforward method is to extract them from the organisms, during which complicated procedures including growing organisms and purification are involved.[65-67] The extracted

biomolecules usually can only be used in reproducing the materials they are originally associated with and are difficult to be modified or engineered, limiting their practical uses. Recently, the in vitro evolutionary selection technique emerged as a general route for identifying biomolecules that show specific affinities for various arbitrary materials of interest.[68]

The so called phage display (PD, schematic is shown in Fig. 1.3) has been well-developed and used for identifying peptide sequences exhibiting affinity for various inorganics.[68,69] The libraries are generated by inserting random oligonucleotides into phage genome or bacterial plasmids. The resultant surface of organisms such as the coating protein of phage or the outer membrane of a cell is incorporated and displayed with a random polypeptide sequence.[70] During the biomimetic evolution process, libraries are exposed to inorganic substrates and several washings can exclude non-binders. In the case of a phage display library, bound phage are eluted and amplified by re-infecting their host. The amplified phages are then used as the sub-library in the next round of selection. This complete process is called biopanning. Usually three to five rounds of biopanning are repeated to select strong binders. Eventually, clones are sequenced to identify the inorganic substrate-binding peptide sequences. The identified peptide sequences show specific and selective binding affinity to surface of a particular material.

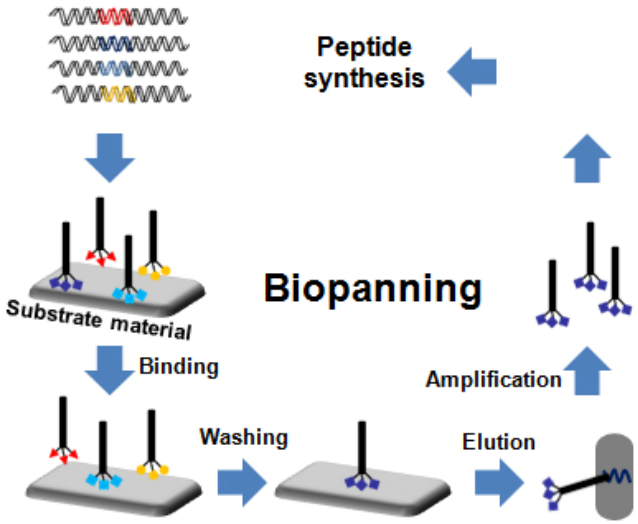

Figure 1.3 Schematic of phage display technique.

1.2.2 Fmoc solid phase peptide synthesis (Fmoc-SPPS)

The fundamental premise of this technique involves the incorporation of N-a-amino acids into a peptide of any desired sequence with one end of the sequence remaining attached to a solid support matrix. While the peptide is being synthesized usually by stepwise methods, all soluble reagents can be removed from the peptide-solid support matrix by filtration and washed away at the end of each coupling step. After the desired sequence of amino acids has been obtained, the peptide can be removed from the polymeric support.

The general scheme for solid phase peptide synthesis is outlined in Fig. 1.4. The solid support is a synthetic polymer that bears reactive groups such as -OH. These groups are made so that they can react easily with the carboxyl group of an N-a-protected amino acid, thereby covalently binding it to the polymer. The amino protecting group (X) can then be removed and a second N-a-protected amino acid can be coupled to the attached amino acid. These steps are repeated until the desired sequence is obtained. At the end of the synthesis, a different reagent is applied to cleave the bond between the C-terminal

amino acid and the polymer support; the peptide then goes into solution and can be obtained from the solution.

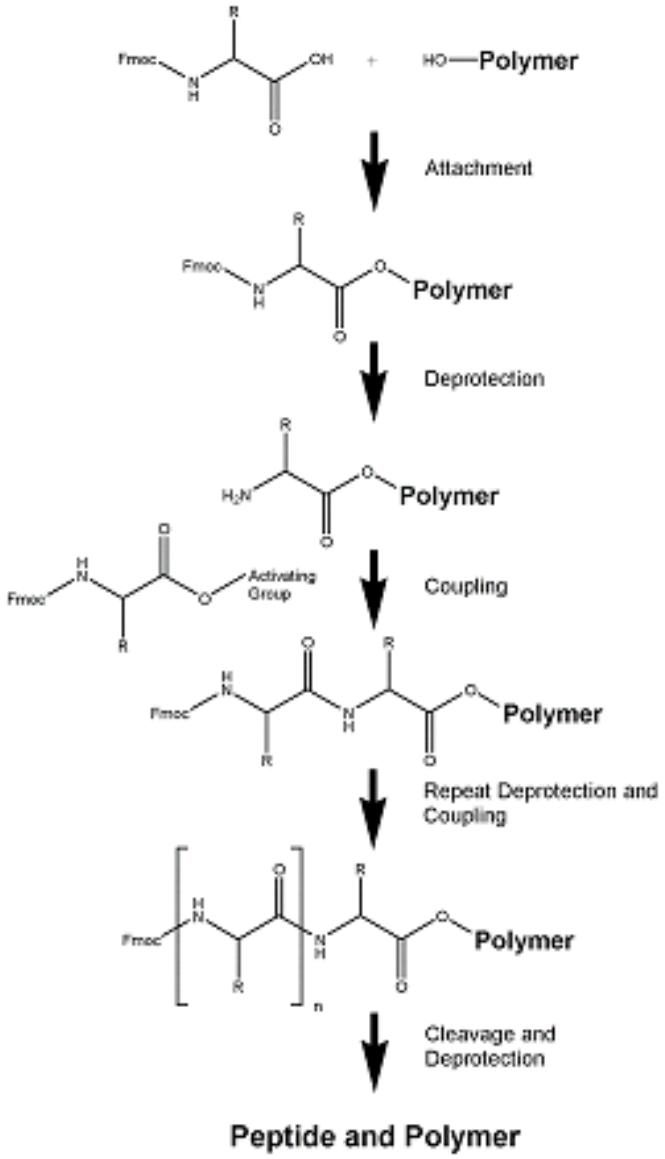

Figure 1.4 General scheme for the peptide synthesis. In this figure, the amino protecting group (X) is the Fmoc group.

The crucial link in any polypeptide chain is the amide bond, which is formed by the condensation of an amine group of one amino acid and a carboxyl group of another.

Generally, an amino acid consists of a central carbon atom (called the a-carbon) that is attached to four other groups: a hydrogen, an amino group, a carboxyl group, and a side chain group. The side chain group, designated R, defines the different structures of amino acids. Certain side chains contain functional groups that can interfere with the formation of the amide bond. Therefore, it is important to mask the functional groups of the amino acid side chain. For Fmoc Strategy in SPPS, the functional groups of the amino acid side chain are all masked by Fmoc group.

1.2.3 Biomimetic synthesis of nanoparticles

Biomimetic synthesis of nanostructures of technically important materials have been studied extensively during the past decade due to their possible applications in sensing, catalysis, imaging, cancer therapy and environmentally friendly synthetic routes.[11,71] The synthesis of nanostructures, especially NPs of different sizes and morphologies of various materials such as semiconductors, metals and minerals, using the conventional chemical approaches have achieved great success after tens of years of development.[13,72] However, elaborate control over the NCs was mostly achieved at rigorous synthetic conditions such as high temperatures, organic solvents, or high pressures, etc. In addition, the synthetic control by the chemical approaches is usually achieved through the trial-and-error process by testing different conditions and chemicals used therein. For example, the colloidal NP growth is believed to be a kinetically controlled process, in which the low energy facets persist while the high energy facets vanish, leading to a particular resultant shape enclosed by the low energy surfaces.[13,72] Therefore, it is important to identify a surfactant that can specifically bind to a particular crystal facet, lowering its surface energy, and lead to NPs with well-controlled shapes. In conventional chemical synthetic

routes, shape control is achieved by employing various surfactants identified through the trial-and-error process. On the other hand, biomolecules can be specifically selected to recognize a chosen surface through a biomimetic molecular evolution process and therefore have the potential to be explored for generalizing the nanomaterial synthesis process. There has been some success in employing the surface-specific biomolecules identified using the PD technique as the stabilizing agent in generating NPs.[73-82]

Earlier work on using selected biomolecules to mediate the formation of various technically important inorganic NCs have demonstrated some exciting results (Fig. 1.5). ZnO (Fig. 1.5 (a)) and TiO_2 (Fig. 1.5 (b)) NPs have been synthesized in solution with ZnO-1 and Ti-1peptides which were selected against ZnO particle surface and rutile TiO_2 single crystal surface, respectively.[80,82] In addition, when ZnO-1 was immobilized on gold plate via an added cysteine onto the C terminus, it could induce the nucleation and formation of flower-like ZnO NPs on gold plates (Fig. 1.5 (a)).[82] Gold NPs in Fig. 1.5 (c) was synthesized with A3-Flg peptide where the A3 is selected with PD technique and found to bind to both silver and gold. Flg is a commonly used biomolecular recognition domain for tagging proteins and, in this case, fused to the A3 to stabilize the Au NCs on substrate through the anti-Flg linker.[75] Another work by Naik et. al. demonstrated that well-shaped silver NPs, as shown in Fig. 1.5(d), can be synthesized with AG4 peptide selected by silver crystal without reductant. It is proposed that the free peptide AG4 bind to the (111) face of silver nuclei and provides a chemically reducing environment around the cluster, thereby allowing further accelerated reduction of silver ions at the interface between peptide and metal.[74]

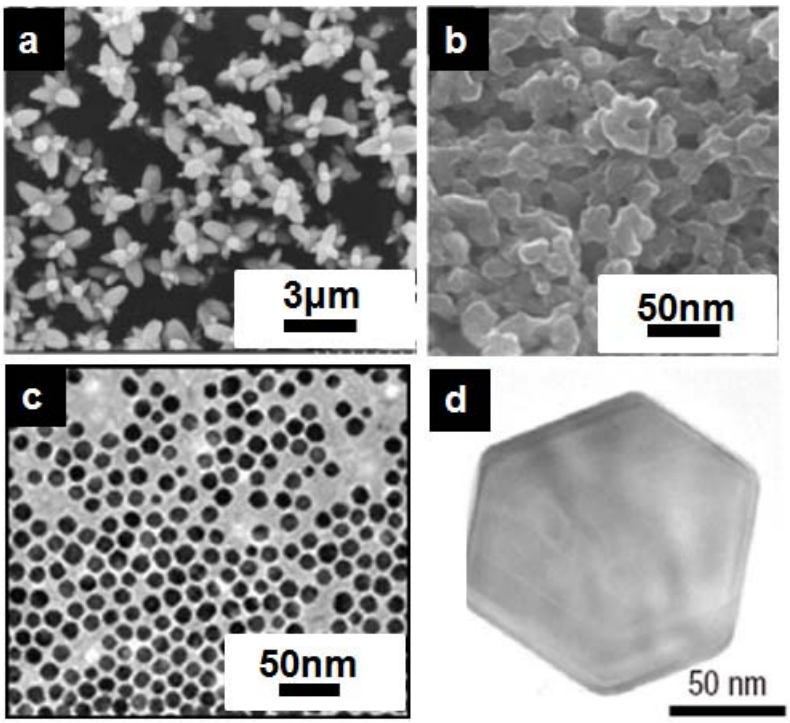

Figure 1.5 (a) TEM images of the solid particles precipitated by the GGGSC-conjugated ZnO-1 peptide.[80] (b) Secondary electron images of titania particles generated in the presence of Ti-1 peptide.[82] (c) TEM image of gold nanoparticles synthesized by the reduction of $HAuCl_4$ by A3-Flg peptide.[75] (d) TEM image of silver nanoparticles obtained using AG4 peptide.[74]

1.3 Catalysts in fuel cells

Fuel cells (FCs) are electrochemical devices that convert chemical energy stored in fuel molecules directly into electricity. The rise of FCs echoes the growing concern on the global environment and efficiency of energy usage. Specifically, unlike the combustion process that produces polluting gasses such as SO_2, NO, and greenhouse gasses such as CO_2, NO_2, and CH_4, FCs produce power with minimal pollutants. In addition, since the intermediate steps of producing heat and mechanical work, which are typical of conventional power generation technologies, are avoided, FCs are not limited

by thermodynamic limitations of traditional heat engines such as the Carnot efficiency. However, in FCs, fuel molecules and oxidants (typically oxygen from air) have to be continuously replenished to allow continuous operation.

1.3.1 Basics of fuel cells

Unit cells form the core of a FC. The basic physical structure, or building block, of a FC consists of an electrolyte layer in contact with an anode and a cathode on either side. A schematic representation of a unit cell with the fuel molecules and the ion conduction flow directions through the cell is shown in Fig. 1.6.

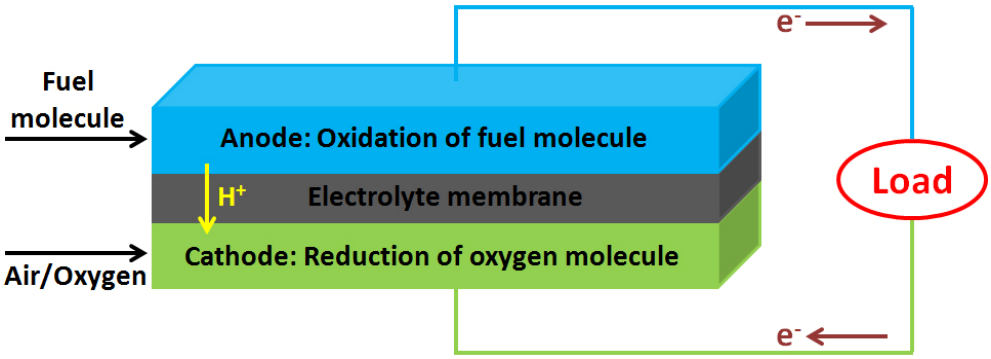

Figure 1.6 Schematic of a unit cell of fuel cell. Theoretically, fuel molecules can be all chemicals that can be oxidized, including gaseous and liquid organic molecules, metals, etc. The membrane conduct only ions.

In an unit cell, fuel molecules are oxidized on anode and oxygen molecules are reduced on cathode. The theoretical voltage of a FC unit is the difference between standard reduction potentials of the fuel molecules and oxygen. Driven by the cell potential, the flow direction of electrons is, as highlighted in the schematic, from anode to cathode, doing work on load devices. Electrolyte can be either liquid or solid, conducting ions to supply the reactants on the other electrode.

Depending on the type of electrolyte, commonly used FCs include: (1) polymer electrolyte fuel cell (PEFC), (2) alkaline fuel cell (AFC), (3) phosphoric acid fuel cell (PAFC),(4) molten carbonate fuel cell (MCFC), and (5) solid oxide fuel cell (SOFC). The characteristics of these FCs are listed in Table 1.3.

Table 1.3 Summary of major differences of the fuel cells with different electrolyte.

	PEFC	**AFC**	**PAFC**	**MCFC**	**SOFC**
Electrolyte	Hydrated Polymeric Ion Exchange Membranes	Mobilized or Immobilized Potassium Hydroxide in asbestos matrix	Immobilized Liquid Phosphoric Acid in SiC	Immobilized Liquid Molten Carbonate in $LiAlO_2$	Perovskites (Ceramics)
Electrodes	Carbon	Transition metals	Carbon	Nickel and Nickel Oxide	Perovskite and perovskite/metal cermet
Catalyst	Pt	Pt	Pt	Electrode material	Electrode material
Operating Temperature	40-80 ^{o}C	65-220 ^{o}C	205 ^{o}C	650 ^{o}C	600-1000 ^{o}C
Charge Carrier	H^+	OH^-	H^+	CO_3^{2-}	O^{2-}
External Reformer for hydrocarbon fuels	Yes	Yes	Yes	No, for some fuels	No, for some fuels and cell designs
Product Water Management	Evaporative	Evaporative	Evaporative	Gaseous product	Gaseous product

According to the type of fuel molecules used, FCs can be classified as proton exchange membrane fuel cell (PEMFC), direct methanol fuel cell (DMFC), direct ethanol fuel cell (DEFC), which can be used with PEFC configuration, and direct carbon fuel cell

(DCFC), which is currently developed with AFC, MCFC, and SOFC configurations. The thermodynamics of the reactions in DCFC allow very high efficiency conversion. Therefore, if this technology can be developed into practical system, it could have significant impact on coal-based power generation.

From the comparison, it can be seen that PEFC can be operated at temperature under 80 ^{o}C, which makes it most potential and attracting for real application on automobiles. In my work, only PEMFC and DMFC are involved, so some more detailed information about the two types of FCs are further introduced.

1.3.1.1 Proton exchange membrane fuel cells (PEMFC)

In PEMFC, hydrogen is used as fuel chemical, which makes it more special than other types of FCs because the final product is only water with absolutely no polluting or greenhouse gasses. Currently, as the cleanest power conversion tool, it receives the most attentions from all auto manufacturers to be employed as the most potential next-next-generation power source to generate automobiles.

On anode, hydrogen gas is filled continuously onto the electrode and oxidized at low temperatures on Pt-based electrocatalysts into protons, and meanwhile electrons are released out of the cell. The reduction of oxygen molecues occurring on the cathode is the same as all other fuel cells, but also at low temperature similar to the anode. The standard reduction potentials of anode reaction and cathode reaction are 0 and 1.23 V, respectively, so the theoretical cell voltage of the cell is 1.23 V. Considering overpotential and the real condition in which PEMFC is working, the common working cell voltage is around 1.0 V. In addition, for a real FC device, kinetic-wise, hydrogen oxidation reaction rate on anode is much faster than oxygen reduction reaction rate on cathode, so the rate limiting step is

on cathode. This explains over 90% of the research on PEMFC reaction kinetics is focused on cathode.

With the same configuration as shown in Fig. 1.6, the PEMFC uses a proton exchange membrane as the electrolyte and operates at temperatures normally less than 100 ^{o}C. Nafion membranes are the most widely used membranes in PEMFC, which are perfluorosulfonic acid membranes and are chemically stable in PEMFC at working temperatures with the chemical structure shown in Fig. 1.7.

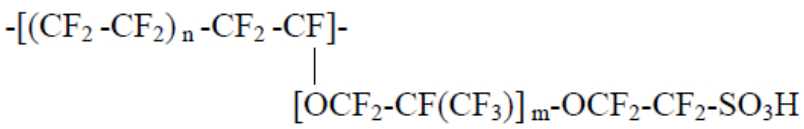

Figure 1.7 Chemical structure of Nafion. Compared with hydrocarbon-based polymer, all hydrogen atoms are substituted with fluorine atoms.

The advanced perfluorosulfonic acid membranes synthesized by the Dow Chemical Company and Asahi Chemical Company, which have shorter side chains and a higher ratio of SO_3H to CF_2 groups, exhibit significant improvement in the FC performance.[83]

1.3.1.2 Direct methanol fuel cells (DMFC)

Industries are interested in the development of DMFC due to several advantages: (1) DMFC uses liquid methanol as the fuel. Therefore, the fuel-processor sub-system to produce hydrogen on-board or the pressure hydrogen-storage system in vehicles can be avoided, which will increase the volumetric power and energy densities of the power source, and decrease the possible danger induced by the hydrogen processor system. (2) methanol itself is a liquid fuel with high gravimetric and volumetric energy density; (3) methanol can be obtained from more abundant sources such as the steam-reformed coal and biomass. However, due to the hydrocarbon nature of methanol, the final products of DMFC

contain CO_2, H_2O and sometimes polluting gases such as CO that originate from partial oxidation of the methanol. Therefore, DMFC is a more appropriate portable power source for electronic devices such as laptop, cellular phones, etc.

Similar to PEMFC, Nafion membrane is also the most commonly used solid electrolyte for DMFC. However, a common issue for the current DMFC technology is the methanol crossover from anode to cathode through the membrane, which causes significant performance loss during the operation. To avoid it from happening, several approaches have been tried, including (1) using a lower concentration of methanol and operating at higher current density; (2) developing composite membrane materials like Nafion-Oxide composite or new membranes that suppress the methanol crossover.[84]

1.3.2 Electro-catalysts in fuel cells

As can be seen from the above discussion, PEMFC and DMFC are the most promising candidates for transportation applications due to the lower working temperature. However, in a typical unit cell, neither of the half reactions on anode or cathode can proceed spontaneously because the energy barriers are too high. As a result, electro-catalysts are necessarily used to lower the energy barriers and accelerate the reaction rates. Various types of materials are capable of serving as electro-catalysts in PEMFC and DMFC, but only noble-metal-based catalysts are currently being employed by the industry due to their high activity and high stability.

1.3.2.1 Electro-catalysts in PEMFC

The commercially available electro-catalysts for hydrogen oxidation reaction (HOR) at anode is mostly carbon supported Pt. Compared with cathode reaction, the HOR is much easier and faster, so the overpotential induced on anode is fairly small.[85] Due to the technological difficulty of storing H_2 on the vehicle as well as the transportation and the

infrastructure, it has been proposed that H_2 can be generated on the vehicle by reforming other fuel molecules such as methanol, propane, natural gas, etc.[86] Therefore, CO residue is usually mixed in the reformed fuel, which is difficult to be removed. The main problem of pure Pt electro-catalyst is that it is not tolerant to CO impurity, fundamentally because CO is preferentially adsorbed on Pt surface which prevents the dissociative adsorption of H_2 on Pt and the subsequent reaction.[87]

To overcome the issue while at the same time maintain the catalytic activity, Pt-based alloy materials have been extensively explored recently. Among various Pt alloys, it has been confirmed by many both academia and industry that Pt-Ru shows much better tolerance to CO than pure Pt.[88] It originates from the lower CO oxidation (CO dissociation) potential on PtRu alloy surface, which is the result of a bi-functional mechanism.

Bi-functional mechanism was originally proposed by Gasteiger et al. to explain the oxidation of methanol molecule on a alloy surface containing two elements.[89] Please refer to Section 1.3.2.2 for the detail of the mechanism. The dissociative oxidation of CO involves the adsorption of CO on Pt atoms, as well as the adsorption of oxygen-containing species (such as hydroxyl group, OH) on Ru atoms, followed with the reaction between the two binding groups as illustrated below.

$$Pt\text{-}(O\text{-}H)^{+} + Ru\text{-}(C\text{-}O) \rightarrow Pt\text{-}O(H^{+})\text{-}C(\text{-}O)\text{-}Ru \rightarrow Pt + Ru + CO_2 + H^{+}$$

It can be inferred from the reaction route that the reaction requires both groups to be present and adjacent to proceed. On pure Pt surface, the adsorption potential of CO (<0.3 V) is much lower than OH (0.7 V), while on PtRu surface, the adsorption of OH is only 0.2 V, which dramatically lowers the potential where CO and OH can simultaneously

adsorb on the surface and thus lowers the energy barrier of the C-O bond formation. Therefore, the oxidation potential of CO on PtRu alloy surface is lower than pure Pt surface, a bi-functional mechanism version for the CO oxidation. So PtRu has become a commercially available anode electro-catalyst for the PEMFC.

For oxygen reduction reaction occurring at the cathode, its kinetic is much lower than the HOR. The exchange current density for oxygen reduction is approximately 10^6 times lower than that of HOR (10^{-3} A/cm^2). As a result, the overpotential in PEMFC is mainly induced by the oxygen reduction at the cathode. The actual cell voltage of PEMFC around 1.0 V, lower than the theoretical value 1.23 V, which is caused mainly by the low exchange current density for oxygen reduction and partially by some competing anodic reactions (oxide formation, oxidation of organic impurities) that leads to a mixed potential.

Oxygen reduction is a multi-electron process that may include a number of sub-steps involving various series-parallel pathways.[90] Due to its complexity, even after half-a-century research, there is still hardly a conclusive mechanism for the mechanism. The generally accepted theory indicates that the O_2 molecule adsorb on the surface with a bridge configuration in which the two bonded oxygen atoms adsorb to different surface metal atoms sitting next to each other. Therefore, the nearest neighbour distance on the surface of the catalyst, as well as the electronic structure, plays an important role in the adsorption and reduction of O_2.[91] Carbon supported Pt NPs has been recognized as the best electro-catalyst for the cathode. But due to the confirmed effects of neighbouring atomic distance and the electronic structure, alloying Pt with transition metal (e.g. Fe, Co, Ni, Mn, etc.) is currently a very hot approach to engineer these parameters to enhance

activities.[92] A large amount of publications are released on cathode electro-catalysts. More detailed introduction can be found in Section 1.3.3.

1.3.2.2 Electro-catalysts in DMFC

The main difference of DMFC from PEMFC is the anode reaction. The kinetic of methanol oxidation is much slower than the HOR in PEMFC because it involves the adsorption of larger molecule and much more complicated oxidation mechanism. As mentioned in the above section, the oxidation of methanol molecule is proceeding with a bi-functional mechanism. The pathway of the whole oxidation process on anode is as follows.

$$CH_3OH + Pt \rightarrow Pt\text{-}(CH_3OH)_{ads} \quad (1)$$

$$Pt\text{-}(CH_3OH)_{ads} \rightarrow Pt\text{-}(CO)_{ads} + 4H^+ + 4e^- \quad (2)$$

$$H_2O + M \rightarrow M\text{-}(OH)_{ads} + H^+ + e^- \quad (3)$$

$$Pt\text{-}(CO)_{ads} + M\text{-}(OH)_{ads} \rightarrow Pt + M + CO_2 + H^+ + e^- \quad (4)$$

M stands for Pt in pure Pt catalyst, or other metals in alloy catalysts. The bi-functional mechanism, as what it literally means, involves two parallel processes. In the methanol oxidation case, it involves: (1) the adsorption of methanol molecule and the subsequent dehydration to CO; (2) the adsorption of hydroxyl group, and then the subsequent bond formation between O (in OH) in C (in CO). From the equations, it can be seen that after the dehydration of methanol into CO, the following steps are similar to the oxidation of CO which has been discussed in last section. In total, the process involves a six-electron transfer, and huge amount of CO intermediate which are capable

of poisoning the electro-catalysts. The complicate mechanism contributes significantly to the overpotential in DMFC. Currently, PtRu alloy is the state-of-the-art anode electro-catalyst for DMFC anode, which shows significantly higher electro-catalytic activity than pure Pt. This is because the hydroxyl group adsorption (Step 3) occurs at much lower potential on Ru than on Pt, which dramatically lowers the energy barrier for the oxidation pathway on PtRu alloy surface.[89] In addition, with the existence of Ru (or another metal), the electronic structure of Pt 5d band can be altered for a modified adsorption behavior of methanol, also enhancing the reaction rate.[93]

As can be seen, for both PEMFC and DMFC, the improvement in performance will largely depend on the development of more active, CO-resistent cathode electro-catalysts as well as new membranes that are able to reduce the crossover of fuel molecules. Particularly for DMFC, highly active electro-catalysts that can tolerate methanol need to be developed to enhance the lifetime.

1.3.3 Cathode in fuel cells: Oxygen reduction reaction

As mentioned previously, in most FCs, a large portion of the overpotential come from the low exchange current density of oxygen reduction reaction (ORR) at cathode. Today, in the generally accepted theory of ORR kinetics, an oxygen molecule will experience the following steps:[94]

$$Pt + O_2 + H^+ + e^- \rightarrow Pt\text{-}(O_2H)_{ads} \quad (5)$$

$$Pt\text{-}(O_2H)_{ads} + H_2O \rightarrow 3\ Pt\text{-}(OH)_{ads} \quad (6)$$

$$Pt\text{-}(OH)_{ads} + H^+ + e^- \rightarrow Pt + H_2O \quad (7)$$

The whole reaction involves four-electron transfer per O_2 molecule, among which the step illustrate by Equation 5, i.e. the dissociative adsorption of O_2, is the rate limiting step. There are generally three models describing how O_2 adsorbs on metal surface as shown in Fig. 1.8.

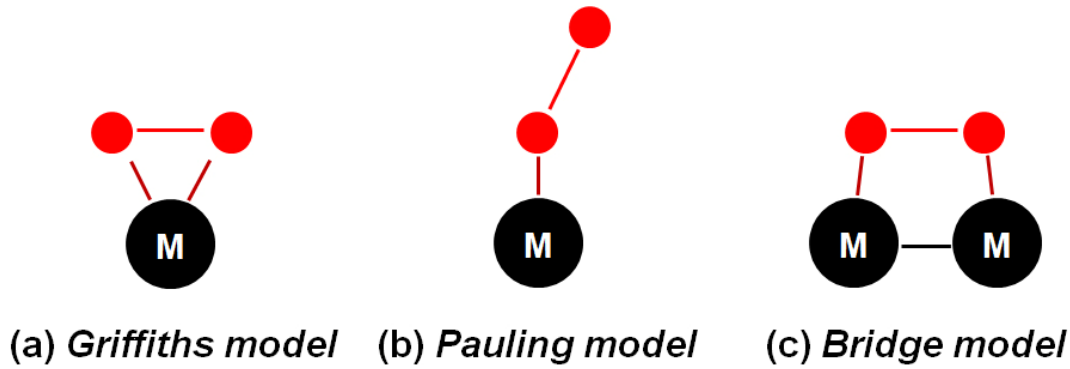

Figure 1.8 Commonly used models for O_2 molecule chemisorbed on metal sites before the first electron is introduced.

The bridge model proposed by Yeager, is the commonly accepted model for Pt-based electro-catalysts.[95] According to the bridge model, when O_2 adsorbs laterally on the surface, it requires two adsorption sites with partially filled d-orbital for bonding with the π^* orbital of the O_2, so the oxygen adsorption on metal is related to the number of unpaired electrons, or d-band vacancy. Metals with high number of unpaired electrons are expected to have high oxygen coverage. Also, the bond strength between oxygen and the surface atom is related to the density of states (DOS) in the d-band, i.e. the electronic structure of the d-band.[96,97] Theoretical model has been proposed by Hammer and Noskov to correlate the binding energy in the dissociative oxygen adsorption with the DOS in d-band, and it has been generally accepted by the academia that for metals with similar crystal structure, there is a semi-linear relationship between the binding energy and the energy center of the d-band.[98] When the d-band center is sitting at higher energy

level, the binding energy is usually high, vice versa, with the linear relationship shown in Fig. 1.9.

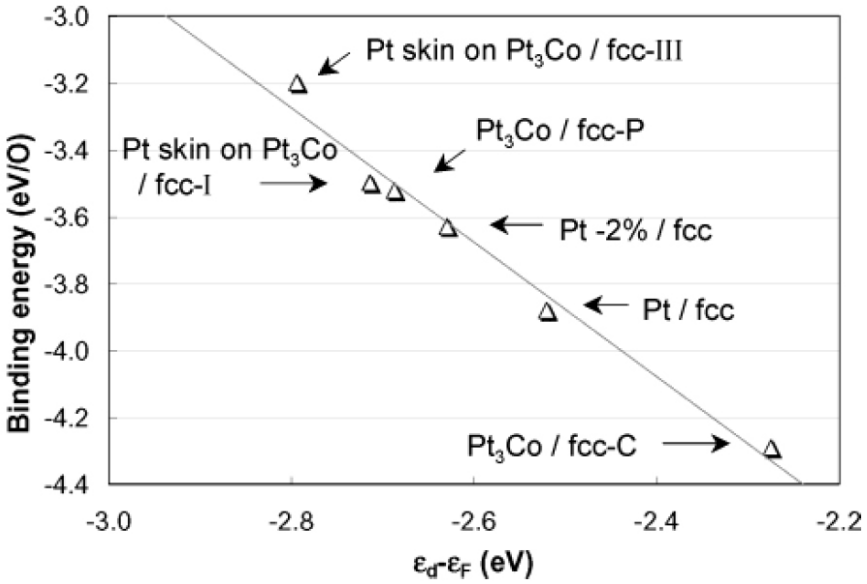

Figure 1.9 Binding energies of Oxygen vs. d-band centers (ε_d) of the four clean surfaces. Labels identify the adsorption sites. The best linear fit is drawn.[99]

The relationship between the oxygen binding energy and the DOS in d-band has been obtained. It was then further found that the ORR activities (on-set potential) of metals show a volcano relationship with the d-band center, which means that only intermediate oxygen binding energies generate highest ORR activities.[100] Neither high or low oxygen binding energies can benefit the ORR activity because if the binding is too strong, oxygen cannot dissociate after the O-O bond breaks, while if it is too weak, the O_2 can dissociate even before the O-O bond breaks. As a result, the appropriate interaction between the O_2 and the surface atoms is critical for the ORR rate.

Currently, non-Pt based electro-catalysts that can be used for the ORR include transition metal oxide, such as $Mn_xCo_{3-x}O_4$, CrO_2, etc.; metal-containing macrocyclic

compounds, such as cobalt phthalocyanine, iron porphyrin composited with carbon blacks;[101] Chevrel phase-type compounds, such as $Mo_{6-x}M_xX_8$ (M=transition metal, X=chalcogen);[102] Transition metal sulfides, such as NiS, and $Mo_2Ru_5S_5$;[103,104] Ruthenium-based chalcogenides, such as $Ru_xMo_{2-x}SeO_4$.[105] In addition to the pure Pt, Pt-based ORR electro-catalysts include: binary Pt alloys, such as Pt-M (M=first-row transition metal, e.g. Ti, V, Cr, Mn, Fe, Co, Ni, Cu, Zn) with Pt_3M ordered structure;[106] ternary Pt alloys, such as Pt-Fe-M (M=Cr, Mn, Co, Ni, Cu), and Pt-Co-M (M=Cr, Ni);[107,108] Pt (or Pt alloy)/oxide composites, such as Pt/WO_3, Pt/TiO_2.[109-112] But so far, according the several criteria for the choice of ORR catalysts in industry, including: (1) stability in acidic electrolyte under 100 ^oC; (2) activity in operating condition after repeated cycling; (3) cost compared with current commercialized Pt/C catalyst, none of the non-Pt based electro-catalysts can achieve the standards of commercialization while Pt alloys are very potential in replacing Pt/C catalyst for PEMFC and DMFC applications.

1.3.4 Method to study ORR: Rotating disk electrode (RDE)

Prior to the population of RDE, ORR was studied with dropping mercury electrode (DME). For DME measurement, the area is changing during the measurement, which complicated the analysis with the change in pseudo-steady state current. It is quite understandable that the natural convection will vary easily due to a variety of noises during experiment, but by using RDE with forced convection, the repeatability in the specific activity measurements and limiting current density measurements improved dramatically.

A typical RDE set-up is shown in Fig. 1.10 (a) and the convection applied to the solution in the vicinity of the electrode is shown in Fig. 1.10 (b). The electrolyte

containing the reactant species flow near the electrode and then spiral out from the middle to the periphery of the electrode. In a rotating ring disk electrode (RRDE) configuration, the electroactive species move from the disk electrode to the ring electrode. When varying the rotating rate and the overpotential, the reaction rate of reactant species on electrode for a controlled half-cell can be evaluated. It can be seen from Fig. 1.10 (a) that similar to most of the electrochemical system, a three-electrode configuration with reference electrode (standard hydrogen electrode (SHE), saturated calomel electrode (SCE), and Ag/AgCl, etc.), a working electrode and a counter electrode are used in RDE measurement.

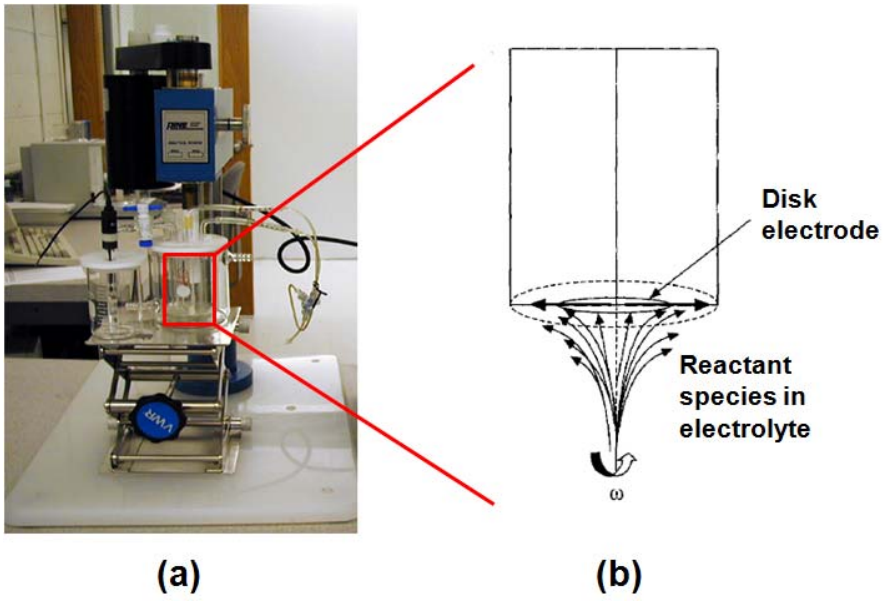

Figure 1.10 (a) Experimental setup of a RDE measurement. (b) Schematic of convection occurring in the vicinity of a RDE.

Linear sweep voltammetry (LSV) is often used to study the intrinsic kinetics of the catalyst provided the current is a fraction of the mass transport limited current density. Any current measured in LSV with rotating disc electrode has contributions from two

main sources: an intrinsic kinetic current of the electrochemical reaction on the surface of the electrode, and diffusional current of reactant through space above the surface of the electrodes. This current i is governed by the Koutecký-Levich (L-K) equation listed in Equation (8)

$$\frac{1}{i} = \frac{1}{i_d} + \frac{1}{i_k} \tag{8}$$

where i_k refers to the kinetic current and i_d refers to the diffusion limiting current.[113,114] According to the definition of i_d, it can be seen that when the rotating rate is higher, i_d will go up. It can be implied from Equation (8) that when i_d goes far below the kinetic current i_k, the total current i will be dominated by i_d, which means that at very low rotating rates (or static state which is the lowest rotating rate) i_k can hardly contribute to the measured current i. It explains why the rotating disk electrode needs to be used if the real kinetic current needs to be studied. When the rotating rates goes up to a level at which the diffusion limiting current i_k is much higher than kinetic current i_k, the diffusion current factor in Equation (8) can be eliminated and the measured current i will be dominated by i_k. Theoretically, ik is only related to the potential following the Butler-Volmer equation, and i_d is only related to rotating rate ω, following the equation as follows

$$i_d = B\omega^{1/2}, \text{ where } B = 0.62nFC_0D_0^{2/3}/\eta^{1/6} \tag{9}$$

where n is the overall number of electrons transferred in oxygen reduction, F is the Faraday constant, C_0 is the bulk concentration of O_2 saturated in the electrolyte, D_0 is the diffusion coefficient of O_2, and η is the kinematic viscosity of the electrolyte.[113,115]

For ORR, the commonly seen LSV (also called polarization curve) is shown in Fig. 1.11. It can be divided into 4 regions from left to right: Diffusion control region (stabilized current, also called diffusion limiting current); Mixed Diffusion-Kinetics control region; Kinetic control region; Corrosion region. Typically, the stabilized current, which is only related to the rotating rate, can be treated as diffusion current i_d in Equation (8). In the diffusion control region, kinetic current is very large so the factor containing the i_k can be neglected. But in Region 2 and 3, since kinetic current i_k starts to drop to the level which falls into the same magnitude as the id or even smaller than id, the factor containing the i_k needs to be taken into account.

If polarization curves are taken at different rotating rates, the measured current i can be taken at a certain potential in the mixed diffusion-kinetic control region at different rates and be plot to corresponding rotating rates ω in the form of i^{-1} vs. $\omega^{-1/2}$, and the slope is 1/B (which is the L-K plot). More importantly, According to L-K plot, the intercept of the curve (supposed to be a linear curve) with the i^{-1} axis is the kinetic current at that potential. In this way, the kinetic current can be calculated by extrapolation. The kinetic current can then be treated as the natural property of the material and compared between different materials.

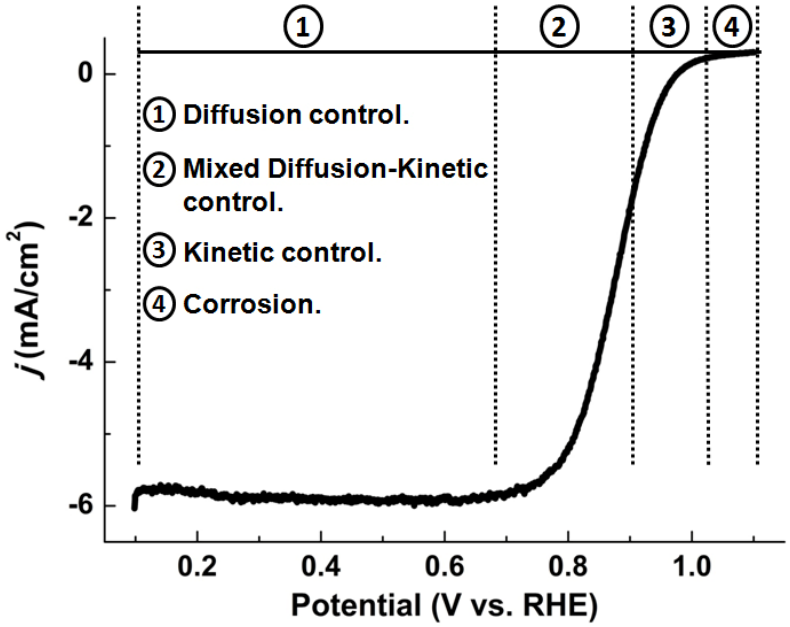

Figure 1.11 Typical polarization curve for ORR measured in O_2 saturated 0.1 M $HClO_4$ electrolyte at the rotating rate of 1600 rpm.[116]

1.4 Objectives

Today, PEMFC and DMFC are attractive power conversion devices that generate much lower pollution than that of fossil fuel, therefore they are considered to be potential replacement of conventional power sources on automobiles. The operation and performance of PEMFC and DMFC depend largely on electro-catalysts positioned between the electrode and the membranes. The most commonly used electro-catalysts for PEMFC and DMFC are Pt-based noble metal nanoparticles, so catalysts take almost 50% of the total cost of the fuel cell. The synthesis of such nanoscale electro-catalysts are commonly limited to harsh conditions (high temperature, high pressure), organic solvent, high amount of stabilizing agent, to achieve the size and morphological control. There is no rational guideline for the selection of stabilizing agent for specific materials, leading to the current "trial and error" approach in selecting stabilizing agent.

The objectives of this dissertation are (1) to develop a bimomimetic approach to select material-specific biomolecules as capping agent for the synthesis of Pt nanoparticles, (2) morphology and size controlled synthesis of Pt nanoparticles, (3) to use as-synthesized Pt nanoparticles as starting material for the synthesis of Pt-based bimetallic nanoparticles, (4) to improve the electrocatalytic activities of the bimetallic nanoparticles in ORR and methanol oxidation reaction.

With the above objectives, first, phage display (PD) technique was used to select peptide that specifically recognizes the surface of Pt, and the selected peptides can be used as stabilizing agent to synthesize monodispersed Pt nanoparticles with tunable morphologies under mild synthetic conditions (atmospheric room temperature, aqueous solution). With fairly easy processing, the nanoparticles can be used as high surface area cathode electro-catalyst in fuel cells. Then, with the as-synthesized Pt nanoparticles, bimetallic nanoparticles containing Pt, including heterogeneously structured Pt-Pd core-shell nanoparticles, and homogenerously alloyed PtRu nanoparticles were synthesized and tested in electrochemical half cells for applications in PEMFC and DMFC. The Pt-Pd core-shell nanoparticles, with Pd shell thickness controlled with atomic-layer precision, show good enhancement in catalytic activity for the ORR as well as better catalytic performance in oxidation of methanol, compared with commercially available catalysts. RDE was used to study the fundamental kinetics and quantified catalytic activities in ORR. The seed-mediated synthesis of hyperbranched PtRu nanoparticles demonstrates the possibility of low-temperature synthesis of well-alloyed material, and shows the enhanced catalytic activity in methanol oxidation compared with commercial catalysts, with its special formation mechanism studied.

[References/Bibliography]

(1) Hao, R.; Xing, R.; Xu, Z.; Hou, Y.; Gao, S.; Sun, S. *Adv. Mater.* **2010**, *22*, 2729.

(2) Law, M.; Goldberger, J.; Yang, P. D. *Annual Review of Materials Research* **2004**, *34*, 83.

(3) Lewis, L. N. *Chem. Rev.* **1993**, *93*, 2693.

(4) Allen, M. J.; Tung, V. C.; Kaner, R. B. *Chem. Rev.* **2010**, *110*, 132.

(5) Hagfeldt, A.; Gratzel, M. *Chem. Rev.* **1995**, *95*, 49.

(6) Bianchini, C.; Shen, P. K. *Chem. Rev.* **2009**, *109*, 4183.

(7) Bae, C.; Yoo, H.; Kim, S.; Lee, K.; Kim, J.; Sung, M. A.; Shin, H. *Chem. Mater.* **2008**, *20*, 756.

(8) Niu, W.; Xu, G. *Nano Today* **2011**, *6*, 265.

(9) Mazumder, V.; Lee, Y.; Sun, S. *Adv. Funct. Mater.* **2010**, *20*, 1224.

(10) Jun, Y. W.; Choi, J. S.; Cheon, J. *Angewandte Chemie-International Edition* **2006**, *45*, 3414.

(11) Daniel, M. C.; Astruc, D. *Chem. Rev. (Washington, DC, U. S.)* **2004**, *104*, 293.

(12) Yan, Z. G.; Yan, C. H. *J. Mater. Chem.* **2008**, *18*, 5046.

(13) Xia, Y.; Xiong, Y.; Lim, B.; Skrabalak, S. E. *Angewandte Chemie-International Edition* **2009**, *48*, 60.

(14) Lamer, V. K.; Dinegar, R. H. *J. Am. Chem. Soc.* **1950**, *72*, 4847.

(15) Zheng, H.; Smith, R. K.; Jun, Y.-w.; Kisielowski, C.; Dahmen, U.; Alivisatos, A. P. *Science* **2009**, *324*, 1309.

(16) Yuk, J.; Park, J.; Ercius, P.; Kim, K.; Hellebusch, D. J.; Crommie, M. F.; Lee, J.; Zettl, A.; Alivisatos, A. P. *Science* **2012**, *336*, 61.

(17) Lee, H.; Habas, S. E.; Kweskin, S.; Butcher, D.; Somorjai, G. A.; Yang, P. *Angewandte Chemie-International Edition* **2006**, *45*, 7824.

(18) Fu, X.-Z.; Liang, Y.; Chen, S.-P.; Lin, J.-D.; Liao, D.-W. *Catal. Commun.* **2009**, *10*, 1893.

(19) Ahmadi, T. S.; Wang, Z. L.; Green, T. C.; Henglein, A.; ElSayed, M. A. *Science* **1996**, *272*, 1924.

(20) Huang, X.; Tang, S.; Mu, X.; Dai, Y.; Chen, G.; Zhou, Z.; Ruan, F.; Yang, Z.; Zheng, N. *Nature Nanotechnology* **2011**, *6*, 28.

(21) Chen, J. Y.; Herricks, T.; Geissler, M.; Xia, Y. N. *J. Am. Chem. Soc.* **2004**, *126*, 10854.

(22) Lim, B.; Wang, J.; Camargo, P. H. C.; Jiang, M.; Kim, M. J.; Xia, Y. *Nano Lett.* **2008**, *8*, 2535.

(23) Huang, X.; Zhao, Z.; Fan, J.; Tan, Y.; Zheng, N. *J. Am. Chem. Soc.* **2011**, *133*, 4718.

(24) Sun, S. H.; Murray, C. B.; Weller, D.; Folks, L.; Moser, A. *Science* **2000**, *287*, 1989.

(25) Xiong, Y.; Cai, H.; Wiley, B. J.; Wang, J.; Kim, M. J.; Xia, Y. *J. Am. Chem. Soc.* **2007**, *129*, 3665.

(26) Bigall, N. C.; Haertling, T.; Klose, M.; Simon, P.; Eng, L. M.; Eychmueller, A. *Nano Lett.* **2008**, *8*, 4588.

(27) Chen, Y.-H.; Hung, H.-H.; Huang, M. H. *J. Am. Chem. Soc.* **2009**, *131*, 9114.

(28) Weare, W. W.; Reed, S. M.; Warner, M. G.; Hutchison, J. E. *J. Am. Chem. Soc.* **2000**, *122*, 12890.

(29) Brust, M.; Walker, M.; Bethell, D.; Schiffrin, D. J.; Whyman, R. *Journal of the Chemical Society-Chemical Communications* **1994**, 801.

(30) Wang, C.; Daimon, H.; Lee, Y.; Kim, J.; Sun, S. *J. Am. Chem. Soc.* **2007**, *129*, 6974.

(31) Huang, X.; Tang, S.; Zhang, H.; Zhou, Z.; Zheng, N. *J. Am. Chem. Soc.* **2009**, *131*, 13916.

(32) Chen, M.; Wu, B.; Yang, J.; Zheng, N. *Adv. Mater.* **2012**, *24*, 862.

(33) Xiong, Y.; Washio, I.; Chen, J.; Sadilek, M.; Xia, Y. *Angewandte Chemie-International Edition* **2007**, *46*, 4917.

(34) Ciacchi, L. C.; Pompe, W.; De Vita, A. *J. Phys. Chem. B* **2003**, *107*, 1755.

(35) Sun, S. H.; Anders, S.; Thomson, T.; Baglin, J. E. E.; Toney, M. F.; Hamann, H. F.; Murray, C. B.; Terris, B. D. *J. Phys. Chem. B* **2003**, *107*, 5419.

(36) Shevchenko, E. V.; Talapin, D. V.; Schnablegger, H.; Kornowski, A.; Festin, O.; Svedlindh, P.; Haase, M.; Weller, H. *J. Am. Chem. Soc.* **2003**, *125*, 9090.

(37) Lim, B.; Jiang, M.; Camargo, P. H. C.; Cho, E. C.; Tao, J.; Lu, X.; Zhu, Y.; Xia, Y. *Science* **2009**, *324*, 1302.

(38) Habas, S. E.; Lee, H.; Radmilovic, V.; Somorjai, G. A.; Yang, P. *Nat. Mater,* **2007**, *6*, 692.

(39) Wang, C.; Daimon, H.; Sun, S. *Nano Lett.* **2009**, *9*, 1493.

(40) Zeng, J.; Zhu, C.; Tao, J.; Jin, M.; Zhang, H.; Li, Z.-Y.; Zhu, Y.; Xia, Y. *Angewandte Chemie-International Edition* **2012**, *51*, 2354.

(41) Zhang, J. L.; Vukmirovic, M. B.; Sasaki, K.; Nilekar, A. U.; Mavrikakis, M.; Adzic, R. R. *J. Am. Chem. Soc.* **2005**, *127*, 12480.

(42) Cao, Y. W.; Jin, R.; Mirkin, C. A. *J. Am. Chem. Soc.* **2001**, *123*, 7961.

(43) Huang, C. C.; Yang, Z. S.; Chang, H. T. *Langmuir* **2004**, *20*, 6089.

(44) Narayanan, R.; El-Sayed, M. A. *Nano Lett.* **2004**, *4*, 1343.

(45) Wulff, G.; Kristallogr, Z. *Miner.* **1901**, *34*, 449.

(46) Douglas, T. *Science* **2003**, *299*, 1192.

(47) Veis, A. *Science* **2005**, *307*, 1419.

(48) Bazylinski, D. A.; Frankel, R. B. *Nat. Rev. Microbiol.* **2004**, *2*, 217.

(49) Aizenberg, J.; Muller, D. A.; Grazul, J. L.; Hamann, D. R. *Science* **2003**, *299*, 1205.

(50) Calvert, P. *Mrs Bulletin* **1992**, *17*, 37.

(51) Lowenstam, H. A.; Weiner, S. *On biomineralization*; Oxford University Press: New York, 1989.

(52) Seeman, N. C.; Belcher, A. M. *Proc. Natl. Acad. Sci. U. S. A.* **2002**, *99*, 6451.

(53) Zhang, S. G. *Nat. Biotechnol.* **2003**, *21*, 1171.

(54) Mann, S.; Archibald, D. D.; Didymus, J. M.; Douglas, T.; Heywood, B. R.; Meldrum, F. C.; Reeves, N. J. *Science* **1993**, *261*, 1286.

(55) Cha, J. N.; Stucky, G. D.; Morse, D. E.; Deming, T. J. *Nature* **2000**, *403*, 289.

(56) Douglas, T.; Strable, E.; Willits, D.; Aitouchen, A.; Libera, M.; Young, M. *Adv. Mater. (Weinheim, Ger.)* **2002**, *14*, 415.

(57) Kroger, N. *Curr. Opin. Chem. Biol.* **2007**, *11*, 662.

(58) Crookes-Goodson, W. J.; Slocik, J. M.; Naik, R. R. *Chem. Soc. Rev.* **2008**, *37*, 2403.

(59) Katz, E.; Willner, I. *Angewandte Chemie International Edition* **2004**, *43*, 6042.

(60) Whyburn, G. P.; Li, Y. J.; Huang, Y. *J. Mater. Chem.* **2008**, *18*, 3755.

(61) Estroff, L. A.; Hamilton, A. D. *Chem. Mater.* **2001**, *13*, 3227.

(62) Niemeyer, C. M. *Angewandte Chemie International Edition* **2001**, *40*, 4128.

(63) Dameron, C. T.; Reese, R. N.; Mehra, R. K.; Kortan, A. R.; Carroll, P. J.; Steigerwald, M. L.; Brus, L. E.; Winge, D. R. *Nature* **1989**, *338*, 596.

(64) Wainwright, S. A. *Mechanical Design in Organisms*; Princeton University Press: Princeton, 1982.

(65) Xie, J.; Lee, J.; Wang, D. I.; Ting, Y. *Small* **2007**, *3*, 672.

(66) Chandran, S. P.; Chaudhary, M.; Pasricha, R.; Ahmad, A.; Sastry, M. *Biotechnol. Prog.* **2006**, *22*, 577.

(67) Shankar, S. S.; Rai, A.; Ankamwar, B.; Singh, A.; Ahmad, A.; Sastry, M. *Nat. Mater.* **2004**, *3*, 482.

(68) Sarikaya, M.; Tamerler, C.; Jen, A. K. Y.; Schulten, K.; Baneyx, F. *Nat. Mater.* **2003**, *2*, 577.

(69) Whaley, S. R.; English, D. S.; Hu, E. L.; Barbara, P. F.; Belcher, A. M. *Nature* **2000**, *405*, 665.

(70) Barbass, C. F.; Burton, D. R.; Scott, J. K.; Silverman, G. J. *Phage Display, A Laboratory Manual* Cold Spring Harbor Laboratory Press: Cold Spring Harbor, 2001.

(71) Jain, P. K.; El-Sayed, I. H.; El-Sayed, M. A. *Nano Today* **2007**, *2*, 18.

(72) Jun, Y. W.; Choi, J. S.; Cheon, J. *Angew. Chem., Int. Ed.* **2006**, *45*, 3414.

(73) Banerjee, I. A.; Yu, L.; Matsui, H. *Proc. Natl. Acad. Sci. U. S. A.* **2003**, *100*, 14678.

(74) Naik, R. R.; Stringer, S. J.; Agarwal, G.; Jones, S. E.; Stone, M. O. *Nat. Mater.* **2002**, *1*, 169.

(75) Slocik, J. M.; Stone, M. O.; Naik, R. R. *Small* **2005**, *1*, 1048.

(76) Naik, R. R.; Jones, S. E.; Murray, C. J.; McAuliffe, J. C.; Vaia, R. A.; Stone, M. O. *Adv. Funct. Mater.* **2004**, *14*, 25.

(77) Li, Y. J.; Huang, Y. *Adv. Mater. (Weinheim, Ger.)* **2010**, *22*, 1921.

(78) Chiu, C. Y.; Li, Y. J.; Huang, Y. *Nanoscale* **2010**, *2*, 927.

(79) Lee, S. W.; Belcher, A. M. *Nano Lett.* **2004**, *4*, 387.

(80) Dickerson, M. B.; Jones, S. E.; Cai, Y.; Ahmad, G.; Naik, R. R.; Kroger, N.; Sandhage, K. H. *Chem. Mater.* **2008**, *20*, 1578.

(81) Unocic, R. R.; Zalar, F. M.; Sarosi, P. M.; Cai, Y.; Sandhage, K. H. *Chem. Commun. (Cambridge, U. K.)* **2004**, 796.

(82) Umetsu, M.; Mizuta, M.; Tsumoto, K.; Ohara, S.; Takami, S.; Watanabe, H.; Kumagai, I.; Adschiri, T. *Adv. Mater. (Weinheim, Ger.)* **2005**, *17*, 2571.

(83) Mauritz, K. A.; Moore, R. B. *Chem. Rev. (Washington, DC, U. S.)* **2004**, *104*, 4535.

(84) Jia, N. Y.; Lefebvre, M. C.; Halfyard, J.; Qi, Z. G.; Pickup, P. G. *Electrochemical and Solid State Letters* **2000**, *3*, 529.

(85) Mello, R. M. Q.; Ticianelli, E. A. *Electrochim. Acta* **1997**, *42*, 1031.

(86) Alejo, L.; Lago, R.; Pena, M. A.; Fierro, J. L. G. *Applied Catalysis a-General* **1997**, *162*, 281.

(87) Gottesfeld, S.; Pafford, J. *J. Electrochem. Soc.* **1988**, *135*, 2651.

(88) Gasteiger, H. A.; Markovic, N. M.; Ross, P. N. *J. Phys. Chem.* **1995**, *99*, 8290.

(89) Gasteiger, H. A.; Markovic, N.; Ross, P. N.; Cairns, E. J. *J. Phys. Chem.* **1994**, *98*, 617.

(90) Markovic, N. M.; Schmidt, T. J.; Stamenkovic, V.; Ross, P. N. *Fuel Cells* **2001**, *1*, 105.

(91) Min, M. K.; Cho, J. H.; Cho, K. W.; Kim, H. *Electrochim. Acta* **2000**, *45*, 4211.

(92) Xiong, L.; Manthiram, A. *J. Electrochem. Soc.* **2005**, *152*, A697.

(93) Igarashi, H.; Fujino, T.; Zhu, Y. M.; Uchida, H.; Watanabe, M. *Phys. Chem. Chem. Phys.* **2001**, *3*, 306.

(94) Markovic, N.; Gasteiger, H.; Ross, P. N. *J. Electrochem. Soc.* **1997**, *144*, 1591.

(95) Yeager, E. *Electrochim. Acta* **1984**, *29*, 1527.

(96) Norskov, J. K.; Rossmeisl, J.; Logadottir, A.; Lindqvist, L.; Kitchin, J. R.; Bligaard, T.; Jonsson, H. *J. Phys. Chem. B* **2004**, *108*, 17886.

(97) Stamenkovic, V.; Mun, B. S.; Mayrhofer, K. J. J.; Ross, P. N.; Markovic, N. M.; Rossmeisl, J.; Greeley, J.; Norskov, J. K. *Angewandte Chemie-International Edition* **2006**, *45*, 2897.

(98) Hammer, B.; Norskov, J. K. In *Advances in Catalysis, Vol 45: Impact of Surface Science on Catalysis*; Gates, B. C. K. H., Ed. 2000; Vol. 45, p 71.

(99) Xu, Y.; Ruban, A. V.; Mavrikakis, M. *J. Am. Chem. Soc.* **2004**, *126*, 4717.

(100) Lima, F. H. B.; Zhang, J.; Shao, M. H.; Sasaki, K.; Vukmirovic, M. B.; Ticianelli, E. A.; Adzic, R. R. *J. Phys. Chem. C* **2007**, *111*, 404.

(101) Vasudevan, P.; Santosh; Mann, N.; Tyagi, S. *Transition Met. Chem.* **1990**, *15*, 81.

(102) Alonsovante, N.; Tributsch, H.; Solorzaferia, O. *Electrochim. Acta* **1995**, *40*, 567.

(103) Kishi, T.; Shimizu, F.; Nagai, T. *Surface Technology* **1984**, *21*, 109.

(104) Reeve, R. W.; Christensen, P. A.; Hamnett, A.; Haydock, S. A.; Roy, S. C. *J. Electrochem. Soc.* **1998**, *145*, 3463.

(105) Schmidt, T. J.; Paulus, U. A.; Gasteiger, H. A.; Alonso-Vante, N.; Behm, R. J. *J. Electrochem. Soc.* **2000**, *147*, 2620.

(106) Mukerjee, S.; Srinivasan, S. *J. Electroanal. Chem.* **1993**, *357*, 201.

(107) Shim, J.; Yoo, D. Y.; Lee, J. S. *Electrochim. Acta* **2000**, *45*, 1943.

(108) Neergat, M.; Shukla, A. K.; Gandhi, K. S. *J. Appl. Electrochem.* **2001**, *31*, 373.

(109) Chiu, H. C.; Tseung, A. C. C. *Electrochemical and Solid State Letters* **1999**, *2*, 379.

(110) Savadogo, O.; Beck, P. *J. Electrochem. Soc.* **1996**, *143*, 3842.

(111) Shim, J.; Lee, C. R.; Lee, H. K.; Lee, J. S.; Cairns, E. J. *J. Power Sources* **2001**, *102*, 172.

(112) Tamizhmani, G.; Capuano, G. A. *J. Electrochem. Soc.* **1994**, *141*, 968.

(113) Paulus, U. A.; Schmidt, T. J.; Gasteiger, H. A.; Behm, R. J. *J. Electroanal. Chem.* **2001**, *495*, 134.

(114) Bard, A. J.; Faulkner, L. R. *Electrochemical Methods: Fundamentals and Applications*; Wiley: New York, 2001.

(115) Chen, W.; Chen, S. *Angewandte Chemie-International Edition* **2009**, *48*, 4386.

(116) He, T.; Kreidler, E. *Phys. Chem. Chem. Phys.* **2008**, *10*, 3731.

Chapter 2

2 GENERAL EXPERIMENTAL TECHNIQUES

2.1 Materials Preparation

All the materials investigated in this dissertation were synthesized by either low temperature aqueous solution based procedures such as chemical reduction, precipitation, or intermediate temperature (<80 ^{o}C) procedures. The detailed synthesis conditions and procedures will be presented in the respective chapters.

2.2 Characterization

Synthesized electrocatalysts were characterized by the following techniques. More specific procedures for each technique are given in the individual chapters.

2.2.1 Transmission Electron Microscopy (TEM)

The size and morphology of nanoparticles were carried out with Phillips CM120 transmission electron microscopy (TEM) operated at 120 kV. The high resolution TEM (HRTEM) images showing the nanoparticle lattice were captured at FEI TITAN operated at 300 kV.

2.2.1.1 High Angle Annular Dark Field Scanning Transmission Electron Microscopy (HAADF-STEM)

Scanning transmission electron microscopy (STEM) operated at high angle annular dark field (HAADF) mode, which is also called z-contrast STEM mode, can be used to resolve the contrast between different elements due to their differences in atomic weights.

The data were captured on FEI TITAN STEM operated at 300 kV, the same equipment where HRTEM images were captured.

2.2.1.2 Energy-Dispersive X-ray Spectroscopy (EDS)

EDS can be used to measure the localized element ratio in bimetallic nanoparticles. Basically, it can measure the composition of a single nanoparticle or combination of several nanoparticles. The EDS detector was attached to the TITAN STEM, and can be operated in both TEM and STEM modes. The line scanning EDS profile was captured under STEM mode, and the point EDS spectra were captured under TEM mode.

2.2.2 X-ray Diffraction (XRD)

XRD patterns of the prepared electro-catalysts were captured by X'pert diffractometer on zero-background quartz or silicon sample plate.

2.2.3 X-ray photoelectron spectroscopy (XPS)

XPS spectra were captured on Omicron XPS/UPS (ultraviolet photoelectron spectroscopy) system under ultra-high vacuum. Electro-catalysts were casted on silver-coated silicon substrate.

2.2.4 Inductively Coupled Plasma Optical Emission Spectrometry (ICP-OES)

For Pt-based bimetallic electro-catalysts, ICP is the best way to measure the ratio of elements in bulk by dissolving the powders of nanoparticles in known volumes of diluted HNO_3 or HCl.

2.2.5 Zeta potential measurement

Zeta potential (ζ-potential) is a scientific term for electrokinetic potential. From a theoretical viewpoint, zeta potential is electric potential in the interfacial double layer

(DL) at the location of the slipping plane versus a point in the bulk fluid away from the interface. Basically, zeta potential is the potential difference between the dispersion medium and the stationary layer of fluid attached to the dispersed particle. Zeta potential measurement was carried out on Malvern Zetasizer.

2.2.6 Liquid chromatography–mass spectrometry (LC-MS)

LC-MS was used to characterize the peptide molecules synthesized with peptide synthesizer. More specifically, it could be used to determine the molecular weight of the molecules and partly used to analyze their chemical structure.

2.2.7 Ultraviolet–visible spectroscopy (UV-Vis)

All UV-Vis data were captured on Beckman DU 800 Spectrophotometer. Details will be provided in respective chapters.

2.3 Electrochemical characterization

The electrochemical characteristics of the electro-catalysts were examined in a home-made three electrode setup with liquid electrolyte, as shown in Fig. 2.1.

The hydrogen and oxygen adsorption characteristics, and electrochemical surface area were determined by cyclic voltammetry (CV). A commercial Ag/AgCl electrode and platinum wire were employed, respectively, as the reference electrode and counter electrode. For static CV measurement, a glassy carbon (GC) electrode with an area of 0.071 cm^2 was employed as the working electrode. For RDE study, a glassy carbon electrode with an area of 0.196 cm^2 was employed as the working electrode.

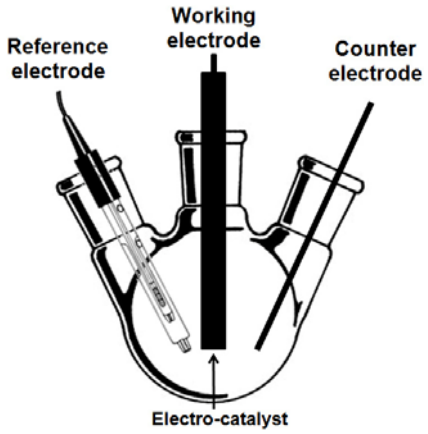

Figure 2.1 Configuration of the home-made three electrode electrochemical cell used for all electrochemical measurement. The difference between static CV and RDE relies on the different working electrode.

Chapter 3

3 SPECIFIC PEPTIDE REGULATED SYNTHESIS OF ULTRASMALL PLATINUM NANOCRYSTALS

3.1 Introduction

Platinum (Pt) nanocrystals (NCs) have been extensively explored because of their excellent catalytic performance in applications such as fuel cell and hydrogen generation.[1,2] Pt NCs of variable sizes have been synthesized using different stabilizing agents.[3-9] Systematic studies have shown that the size of Pt NCs has obvious effect on their catalytic activity and selectivity, especially for sub-10 nm NCs with the high ratio of atoms at corners and edges.[7,10-13] Ultrasmall Pt NCs with size under 5 nm are found to have particularly high catalytic performance in some reactions.[14] To date, the synthesis of ultrasmall Pt NCs under 5 nm involves rigorous synthetic conditions such as high temperature and hazardous organic solvent. The resulting Pt NCs are often not water soluble and make them less accessible for catalytic reactions in aqueous solution. There has been a few reports describing synthesis of water soluble Pt NCs in the sub-5 nm regime, but only with limited control of size and size distributions.[15-17]

Here we report a rational approach to synthesize well dispersed ultrasmall Pt NCs with sizes ranging from ca. 1.7 to 3.5 nm, using specifically selected peptide molecules as the stabilizing agent. We further demonstrated that the strong binding of peptides to Pt NC surface is reversible by either pH modulation or peptide photolysis. The reported Pt NCs are synthesized in aqueous solution at room temperature, which has not been reported for such small Pt NCs. The NCs show good size distribution with size variation

within 10% based on statistical analysis. Using biomolecules, such as peptides, proteins, RNA and DNA, to regulate the formation of inorganic NCs has been an emerging field in recent years.[18] Biomolecules can be specifically selected or designed to recognize a chosen target material through the rational biomimetic evolution approach.[19] As a result, the selected biomolecules can be used as stabilizers to regulate crystal nucleation and growth, and therefore control the size and morphology of the resulting NCs.[20-22]

3.2 Experimental

3.2.1 Selection of peptide molecules specifically binding to Pt

In this study, we used phage display (PD) technique to identify peptide sequences that specifically bind to Pt surface.[19] The biopannings were carried out using Ph.D -7mer peptide library (New England Biolabs) with a 0.25mm diameter, 99.99% pure platinum wire (Sigma Aldrich) as the target. Each wire was cut to be 1 cm long and a fresh wire was used for each round of biopanning. The wire was sterilized in 99% ethanol for fifteen minutes with gentle rocking followed by washing with sterilized water and TBS buffer solution. The biopannings were carried out with established protocol (New England Biolab, Ph.D 7 manual) briefly described below.

~$2x10^{11}$ library phages were diluted in 1ml of 0.1% Tris-Buffered Saline Tween-20 (TBST) and allowed to bind to the target for one hour with gentle rocking. The wire was then washed ten times using 0.1% TBST for the first round and 0.3% and 0.5% TBST for the following two rounds. After washing, the bound phages were eluted using 0.2 M Glycine-HCl (pH 2.2) for seven minutes with gentle rocking followed by neutralization with 1M Tris-HCl (pH 9.1). The eluted phage were then amplified through infecting *Escherichia coli* ER2738 in 25 ml of lysogeny broth (LB) and allowed to grow for 4.5 h

on an incubating shaker. The resulting phage were then purified and used in the following round. After the third round the elution was plated and 10 plaques were collected and sequenced to determine the binding peptide sequence.

The sequence Thr-Leu-His-Val-Ser-Ser-Tyr (TLHVSSY, termed P7A, MW: 805.9) emerged as the specific binder after three rounds of biopanning, which shares the similar hydroxyl group rich motif with previously reported sequences.[18] Free P7A were then synthesized with F-moc solid phase peptide synthesis (SPPS) technique with peptide synthesizer purchased from C.S.Bio Co. The liquid chromatography mass spectrometry (LC-MS) confirmed the high purity and validity of the synthesized sequence. The molecular structure and the characterization with LC-MS show that the purity is higher than 95% (Fig. 3.1).

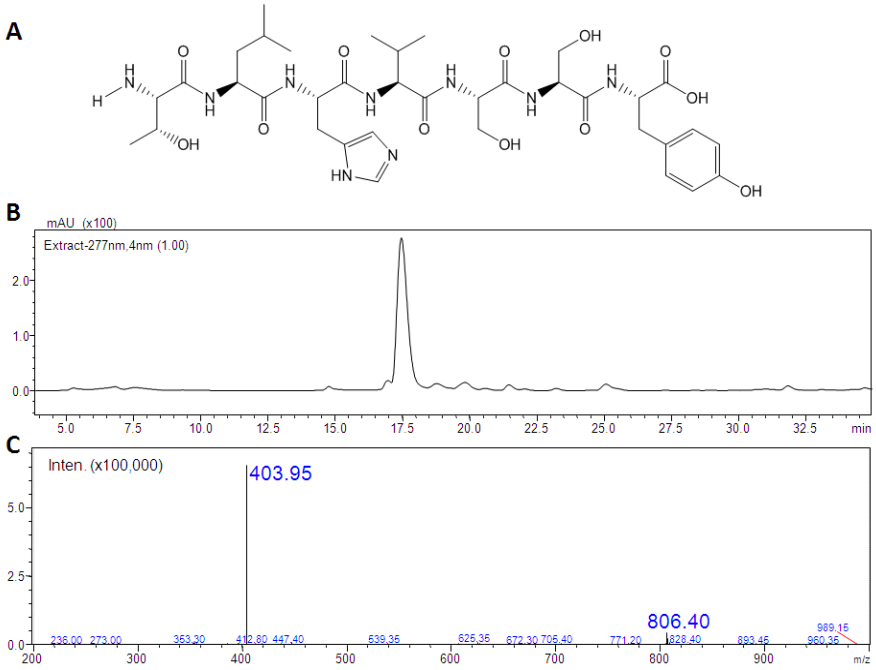

Figure 3.1 (a) Molecular structure of the peptide P7A. (b) LC chromatogram of the 1μg/mL P7A sample. (c) MS spectrum of the eluted sample at 17.5 min. Peaks at 806.40 and 403.95 on m/z axis are for z=1 and z=2, respectively.

3.2.2 Integrity study of the peptide

Peptide P7A was incubated with reactants sodium borohydride ($NaBH_4$, 99.99%, Sigma Aldrich) and potassium tetrachloroplatinate (II) (K_2PtCl_4, purer than 99.9%, Sigma Aldrich) K_2PtCl_4 separately for up to 3 hours. In the mixed solution of P7A and $NaBH_4$, the concentrations of P7A and $NaBH_4$ are 1 mg/mL and 1 mM, respectively. In mixed solution of P7A and K_2PtCl_4, the concentrations are 1 mg/mL and 1 mM, respectively. The salt concentrations were chosen to match the synthetic conditions. The LC-MS results shown in Fig. 3.2 indicates that the peptide did not degrade or react with the reactants prior to the reaction (Fig. 3.2 a, b), and that most peptide stayed intact after the reaction (Fig. 3.2 c). We note although that additional impurity peaks appear in the

LC chromatogram at around 10min, 15min and 31 min (Fig. 3.2 a-c) no observable corresponding peaks are present in mass chromatogram (Fig. 3.2 d), indicating that majority species existing in the solution are still the intact peptides. We suggest the strong signals at these places may come from trace amount of possible peptide-ion complexes existing in the salt solutions.

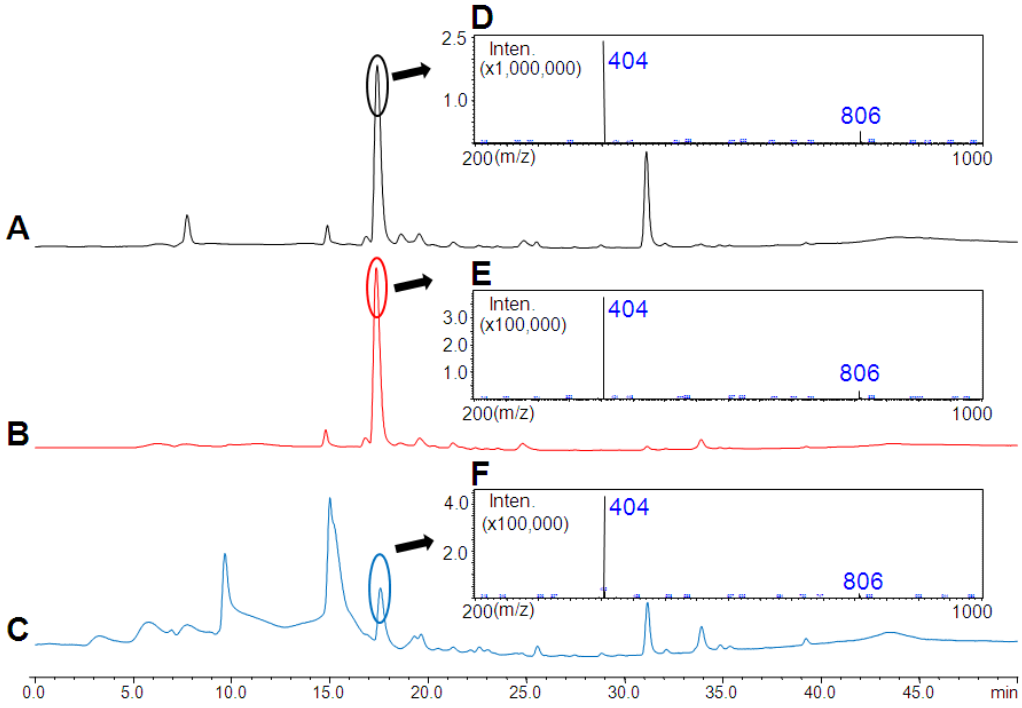

Figure 3.2 (a) is the LC chromatogram of the mixed solution of 1 mg/mL P7A and 1 mM $NaBH_4$ after incubation of 3 h. (b) is the LC chromatogram of the mixed solution of 1 mg/mL P7A and 1 mM K_2PtCl_4. (c) is the LC chromatogram of the supernatant of a post-reaction solution. (d) is the typical mass chromatogram for the above three samples. The impurity peaks in LC chromatograms do not have observable corresponding peaks in mass chromatogram, indicating that majority species existing in the solution are still the intact peptides. Insets are the mass spectra at the time when the characteristic P7A peptide peaks appeared.

3.2.2 Synthesis of platinum (Pt) nanocrystals (NCs)

All experiments were conducted at room temperature. 200 μL of 1 mg/mL P7A aqueous stock solution and 400 μL of 10 mM K_2PtCl_4 aqueous stock solution were added into 3.4 mL of de-ionized (DI) water. The final concentrations of peptide and K_2PtCl_4 are 50 μg/mL and 1mM, respectively. The solution is strongly stirred for at least 5 min. A fresh 40mM $NaBH_4$ aqueous solution was prepared by dissolving 15 mg of $NaBH_4$ into 10 mL of DI water. $NaBH_4$ decomposed quickly in water so the fresh $NaBH_4$ solution should be used soon after preparation. A total of 100 μL $NaBH_4$ solution was injected into the precursor/peptide solution in a single shot. The color of the solution evolves from light brown to black under strong stirring. Reaction solution was taken out to prepare the TEM samples by pipetting droplets of solution onto grids followed by quick drying. The grids were then rinsed with DI water to remove the precursor residues. As a blank control, reactions without the addition of peptides are conducted with the same procedure and TEM samples were prepared with the same method. The imaging of Pt NCs was conducted on Philips CM120 with 120 kV operation voltage. High resolution TEM (HRTEM) was operated on FEI TITAN with 300 kV operation voltage.

3.3 Results and discussion

3.3.1 Synthesis of ultrasmall Pt NCs

For the synthesis of Pt NCs, a mixed aqueous solution of K_2PtCl_4 and P7A peptide was first prepared, into which a fresh 40 mM $NaBH_4$ solution was injected in a single shot. The reaction was strongly stirred at room temperature until no color change can be observed. TEM samples were prepared on copper grids. Blank reactions without adding peptides as well as negative control reactions with a nonrelevant peptide sequence were

also performed. Fig. 3.3 shows the color evolution and TEM images of the afore-mentioned reactions.

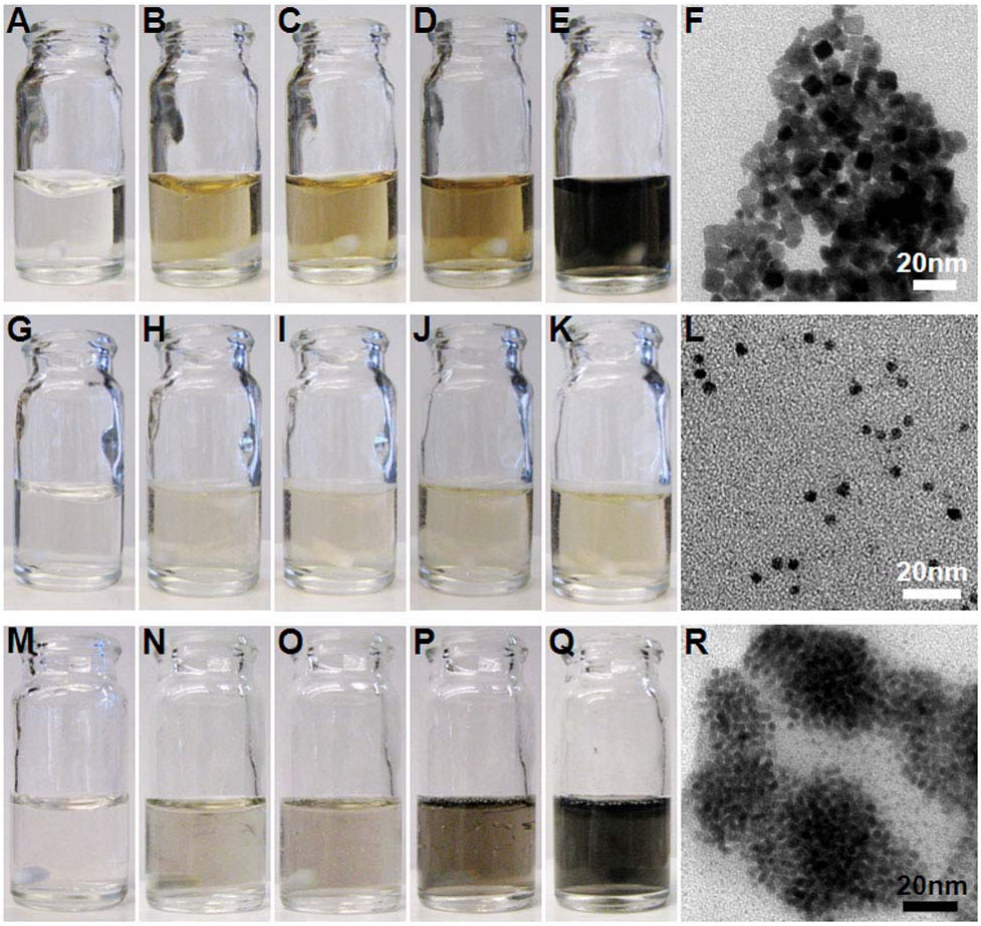

Figure 3.3 Color evolution of blank reaction (a-e), 50 μg/mL peptide reaction (g-k) and negative control reaction (m-q). (a), (g) and (m) are before $NaBH_4$ addition. (b-e), (h-k) and (n-q) are photos taken at 10s, 30s, 1min and 3min after reductant injection. TEM images of the obtained NCs from blank reaction at 10s (f), P7A peptide reaction after 36 hours (l) and C12 peptide reaction at 10s (r).

The quickly darkening color observed in the blank reaction indicates the reaction evolved very fast (Figs. 3.3 a-e). After a couple hours, there were obvious precipitations.

TEM studies show NCs from blank reaction typically have large sizes (> 10 nm) with wide size distribution, and are usually aggregated together even at the very early stage (Fig. 3.2 f). In contrast, the reaction with P7A peptide present evolved much more slowly and is highly controllable (Figs. 3.2 g-k). The resulting solution was stable for up to a few months, indicating NCs were well dispersed in solution. TEM studies show these NCs typically have nearly spherical shapes, with a narrow size distribution, and remain well dispersed in solution even after long duration of aging (Fig. 3.2 l). The comparison with blank reaction implies that the peptides suppress the crystal growth at very early stage and change the growth kinetics of Pt NCs. The negative control experiment with sequence His-Ser-Val-Asn-Lys-Leu-Pro-Thr-Pro-Leu-Arg (HSVNKLPTPLR, termed C12, MW: 1439.7) was carried out to confirm the specificity of P7A to Pt NCs. It was observed that reaction with C12 sequence evolves much faster than that with P7A. At 3 min, obvious precipitation was observed in solution. The TEM image in Fig. 1r shows the aggregations of small NCs. The observations suggest that the free standing peptide P7A, although selected against platinum surface as a part of M13 phage coat protein, retains the strong and specific binding ability to the Pt crystal surface. Although there has been no conclusive answer to date regarding the exact origin of the specific binding of peptide to material surface, the strong binding ability of P7A to Pt observed here might be attributed to the interaction between hydroxyl (i.e. Threonine, Tyrosine and Serine) and/or polar (i.e. Histidine) residue groups and Pt surface.[23] The amino acid sequence while some molecular geometrical factor may also contribute by fitting the functional groups with binding abilities to the atomic arrangements on certain crystallographic facets.[18,24-26]

We tentatively attribute the effects that peptides exert on Pt NC size and shape to its strong binding ability to Pt surface. After the addition of $NaBH_4$, the reduced Pt atoms may form extremely small clusters or nuclei, consisting of only tens of atoms. We suggest that peptides bind to reduced Pt atoms or Pt nuclei and form a peptide coating on Pt NC through the functional residue groups.[27] The coverage of peptides prevents NC growth from particle coalescence and slows down monomer attachment onto the NC surface.[28,29] Hence the Pt NC growth rate with peptide present is greatly reduced when compared to the blank reaction, resulting in much smaller NC sizes. In the meanwhile, when peptides bind to Pt NC surface, it changes the Pt NC surface energy landscape and hence its growth kinetics, which may lead to the observed different morphologies compared to blank reactions.[30]

With the greatly reduced growth rate, we were able to achieve ultrasmall NCs of variable sizes with narrow size distribution by stopping the reaction at different times. In this experiment, aliquots of reaction solution of different time, e.g. 10 s, 60 s, and up to 36 h, were taken out and immediately put into ice bath. Then droplets of different samples were taken to prepare TEM samples. Figs. 3.4 a-f show the TEM images of NCs taken out from reaction at 10 s, 60 s and 5 h. In Fig. 3.4 a, the Pt NCs at 10 s after reductant injection have an average size of 1.73 nm, which is much smaller than the NCs formed at the same time in blank reaction (Fig. 3.4 f). Fig. 3.4 b shows the Pt NCs taken out at 60 s, which have an average size of 2.68 nm. The Fig. 3.4 c shows the NCs obtained from reaction solution 5 h after the injection with an average size of 3.54 nm. High resolution TEM (HRTEM) images in Figs. 3.4 d-f show that the atomic layers in <111> direction, as marked by the arrows, grow from 7 to 12, and finally to 16 layers.

With this approach, ultrasmall Pt NCs of variable sizes below 5 nm can be synthesized in a highly controllable fashion.

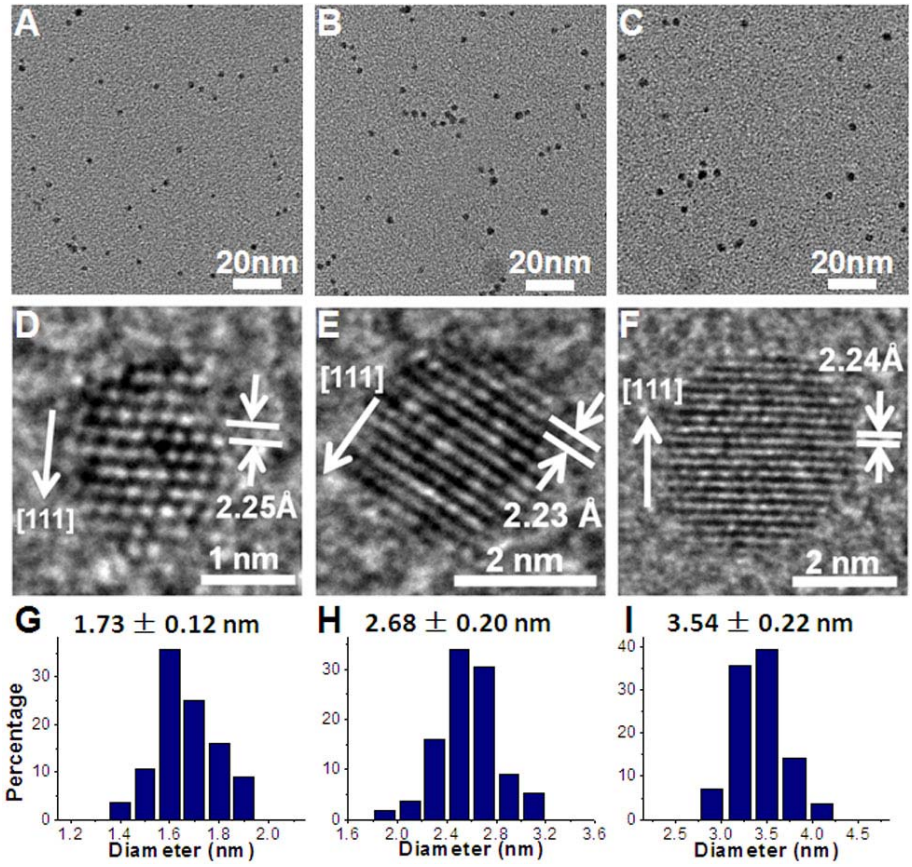

Figure 3.4 (a-c) are the TEM images of reaction samples taken at 10s, 60s and 5h. (d-f) and (g-i) are high resolution images and size distributions of the samples in (a-c), respectively.

Histogram of Pt NC sizes shows highly uniform size distribution, typically with standard deviation less than 10% or less than one atomic layer variation on average (Figs. 3.4 g-i).

3.3.2 Recovery of Pt surface

The purpose of this study is to demonstrate the possibility of removing the peptide molecules from Pt NCs to recover bare Pt NC surface, which is important for catalytic studies.

3.3.2.1 Peptide elution at low PH

The pH value is also known to affect the the peptide-material interaction, i.e. in biopanning, low pH is used to elute (or unbind) phage off the target materials. This very character offers a natural route to unbind the peptide from Pt NC surface by tuning the PH value. In this experiment, we demonstrated that lowering the pH value of the solution had led to the aggregation of Pt NCs, as shown in Fig. 3.5. After the Pt NCs were formed, the pH of the solution was modulated to around 2 by adding appropriate amount of hydrochloric acid (HCl). In Fig. 3.5, vials A and B are Pt NCs with solution pH modulated to 2, and without pH modulation, respectively. Obvious aggregations of Pt NCs appeared in solutions at low pH range, suggesting the removal of P7A from the NCs. LC-MS experiments were further carried out to confirm the elution of peptides from NCs. The experimental procedure is described below.

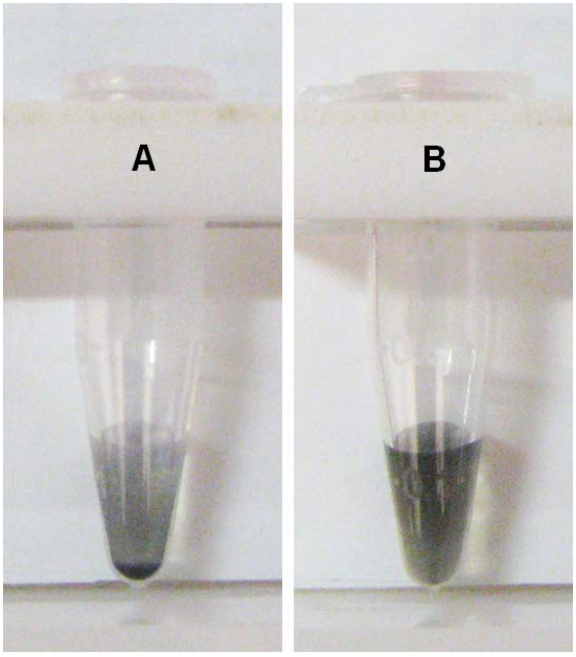

Figure 3.5 (a) Pt NC solution with pH tuned to 2. (b) Pt NC solution without pH tuning. Both photos are taken after 1 hour of aging.

After the synthesis of Pt NCs, the Pt NCs were centrifuged down and the supernatant was removed. The NCs were washed with deionized water (DI water) for 3 times and redispersed in 1 mL of DI water. Two aliquots (of 250 μL each) were taken out from the solution stock. One of them was added with 3 μL of 0.883 M hydrochloric acid (HCl) to obtain a pH=2 solution and the other was added with 3 μL of DI water as a blank control experiment. After vortexing for 10 min, both solutions were centrifuged to obtain the supernatants. The pH 2 supernatant was neutralized to 7 with 1 M of sodium hydroxide (NaOH). And the supernatant from the blank control experiment was tuned to pH=2 (3 μL of 0.883 M HCl), rocked for 3 min, the solution was then transferred into a new tube and neutralized pH of 7 with 2.649 μL of 1 M NaOH. This step is done to eliminate the possible effect of adjusting pH value on peptide concentrations. Both samples were

characterized with LC-MS as shown in Fig. 3.6. It was found that the mass signal of P7A in pH=2 supernatant is higher, indicating more P7A peptide molecules in this solution. We attribute the excess peptide molecules appeared in the low pH solution to those eluted off the Pt NC surfaces. These experiments confirm that the strong binding between peptide and Pt surface is reversible.

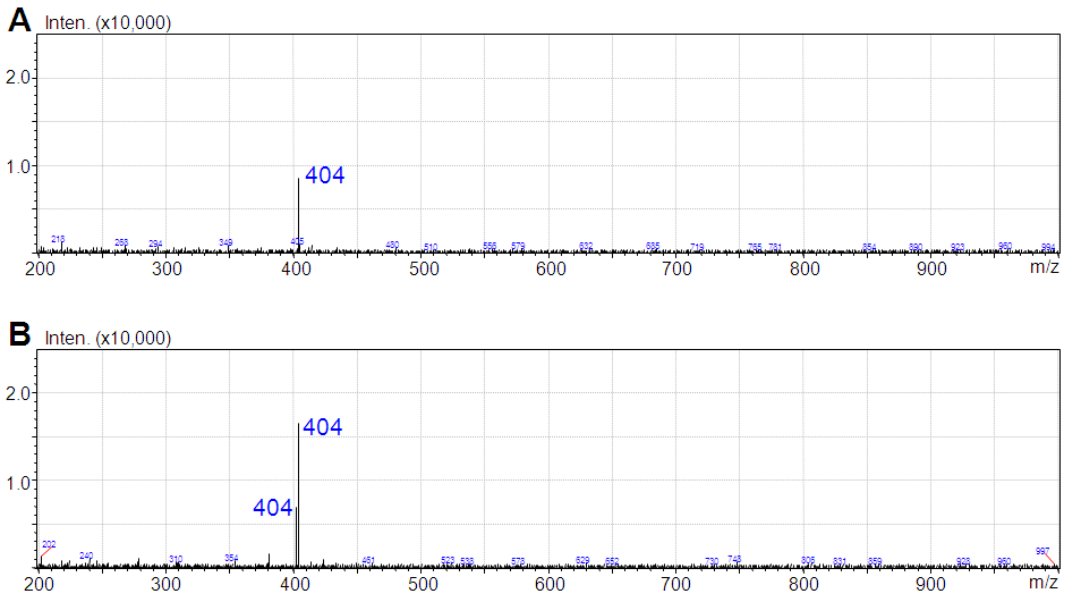

Figure 3.6 (a) and (b) are mass spectra of the supernatants of the blank control experiment and from eluted solution with pH=2, respectively.

3.3.2.2 Photolysis of peptides

UV irradiation can be used to break down the peptide molecules on NC surface. The solution of as-synthesized Pt NCs became obviously darker after UV irradiation (UVP, LLC, 302nm, 8W) (Fig. 3.7 a-c) when compared to that without (Fig. 3.7 e-g). TEM images confirmed that Pt NCs in UV irradiated samples experience severe aggregation, while those in the non-irradiated solution remain well suspended. The result indicated the removal of effective peptide coating on Pt NC surface. Further experiment with LC-MS

on UV irradiated peptide solutions confirmed the decomposition of peptide molecules (Fig. 3.8) due to photolysis. No P7A peptide signal can be found in mass spectrum of post-irradiated samples (Fig. 3.8 c), indicating that the decomposition of P7A peptide may lead to the aggregation of Pt NCs.

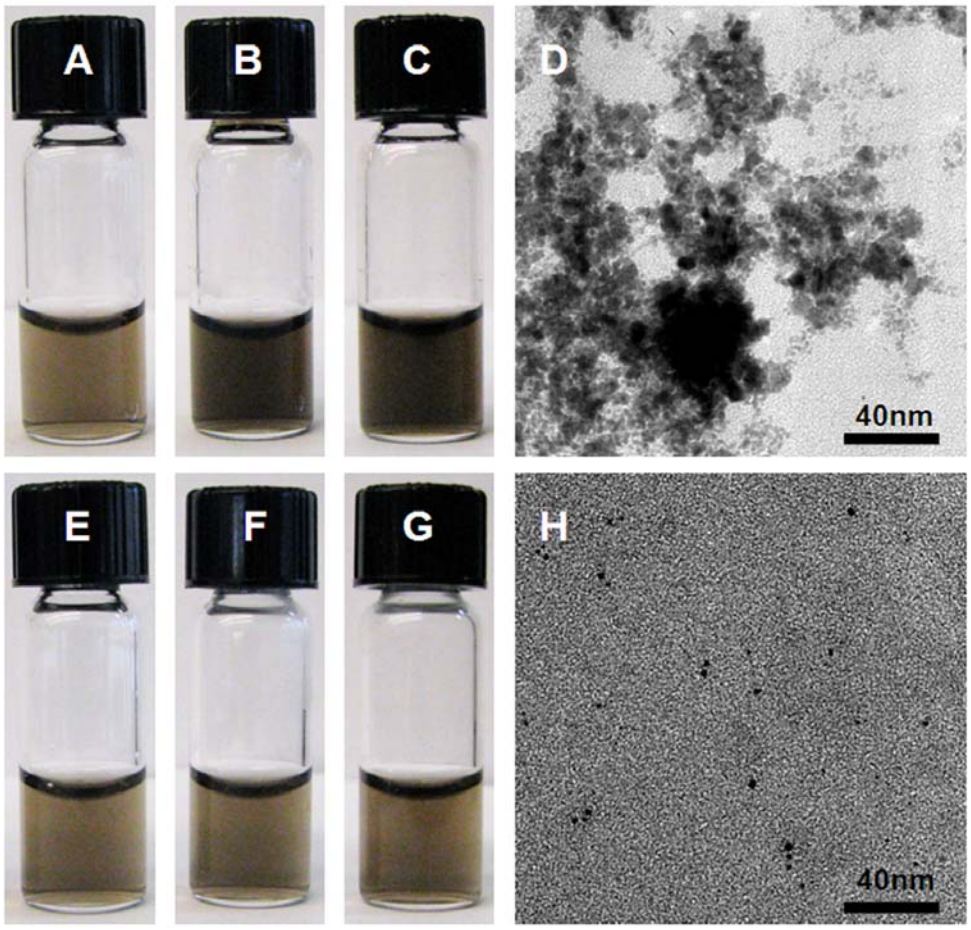

Figure 3.7 (a, b, c) and (e, f, g) are photos of UV illuminated NC solution and non-UV illuminated solution at 0s, 3h and 9h, respectively. (d) and (h) are TEM images of NCs from samples (c) and (g).

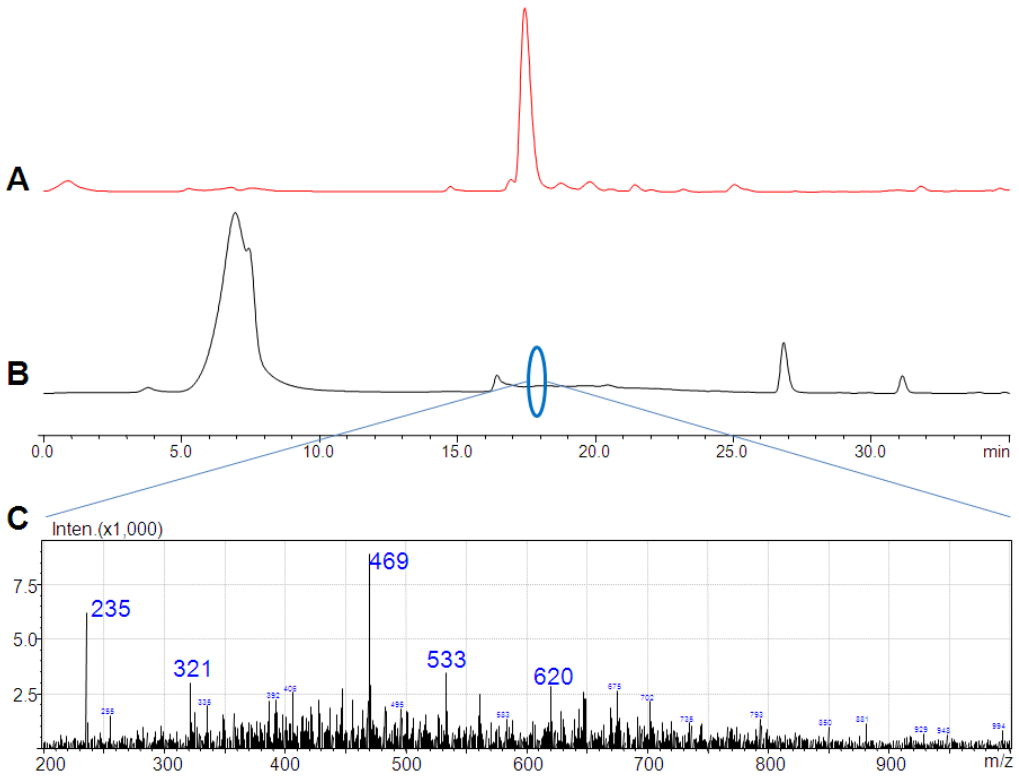

Figure 3.8 (a) and (b) are LC chromatograms of pure P7A peptide solution and UV illuminated peptide solution after 9h. (c) is the mass spectrum of the UV illuminated sample at about t=17.5 min.

It is important to note that the strong interaction between P7A and Pt can be readily tuned or reversed. Our studies have demonstrated that peptide can be unbound from the NC surface by simply lowering the pH of the solution. Alternatively, the peptide can also be degraded through a photolysis process.[31] The results indicate possible approaches to recover Pt NC surface, which is important for catalytic reactions.

3.4 Conclusion

In short, we have reported the rational synthesis of monodisperse ultrasmall Pt NCs, in aqueous solution at room temperature, with specifically selected peptide molecules as

stabilizers. The selected peptide molecule P7A is able to bind to the Pt NC surface and thus can function as stabilizer to regulate Pt crystal nucleation and growth, and therefore control both the morphology and size of the final Pt NCs. Uniform near-spherical Pt NCs with size from 1.73 to 3.54 nm were achieved with very narrow size distribution. It has also been demonstrated that peptide can be unbound from the NC surface by simply lowering the pH of the solution or degraded through a photolysis process.

[References/Bibliography]

(1) Chen, Z. W.; Xu, L. B.; Li, W. Z.; Waje, M.; Yan, Y. S. *Nanotechnology* **2006**, *17*, 5254.

(2) Kojima, Y.; Suzuki, K.; Fukumoto, K.; Sasaki, M.; Yamamoto, T.; Kawai, Y.; Hayashi, H. *Int. J. Hydrogen. Energ.* **2002**, *27*, 1029.

(3) Ahmadi, T. S.; Wang, Z. L.; Green, T. C.; Henglein, A.; ElSayed, M. A. *Science* **1996**, *272*, 1924.

(4) Song, Y. J.; Yang, Y.; Medforth, C. J.; Pereira, E.; Singh, A. K.; Xu, H. F.; Jiang, Y. B.; Brinker, C. J.; van Swol, F.; Shelnutt, J. A. *J. Am. Chem. Soc.* **2004**, *126*, 635.

(5) Jana, N. R.; Peng, X. G. *J. Am. Chem. Soc.* **2003**, *125*, 14280.

(6) Herricks, T.; Chen, J. Y.; Xia, Y. N. *Nano Lett.* **2004**, *4*, 2367.

(7) Tsung, C. K.; Kuhn, J. N.; Huang, W. Y.; Aliaga, C.; Hung, L. I.; Somorjai, G. A.; Yang, P. D. *J. Am. Chem. Soc.* **2009**, *131*, 5816.

(8) Teng, X. W.; Yang, H. *Nano Lett.* **2005**, *5*, 885.

(9) Wang, X.; Li, Y. *Chemical Communications* **2007**, 2901.

(10) Lee, H.; Habas, S. E.; Kweskin, S.; Butcher, D.; Somorjai, G. A.; Yang, P. D. *Angew. Chem.-Int. Edit.* **2006**, *45*, 7824.

(11) Narayanan, R.; El-Sayed, M. A. *J. Phys. Chem. B* **2003**, *107*, 12416.

(12) Wang, C.; Daimon, H.; Lee, Y.; Kim, J.; Sun, S. *J. Am. Chem. Soc.* **2007**, *129*, 6974.

(13) Tian, N.; Zhou, Z. Y.; Sun, S. G.; Ding, Y.; Wang, Z. L. *Science* **2007**, *316*, 732.

(14) Plomp, A. J.; Vuori, H.; Krause, A. O. I.; de Jong, K. P.; Bitter, J. H. *Applied Catalysis a-General* **2008**, *351*, 9.

(15) Huang, J. C.; He, C. B.; Liu, X. M.; Xiao, Y.; Mya, K. Y.; Chai, J. W. *Langmuir* **2004**, *20*, 5145.

(16) Duff, D. G.; Edwards, P. P.; Johnson, B. F. G. *Journal of Physical Chemistry* **1995**, *99*, 15934.

(17) Teranishi, T.; Hosoe, M.; Tanaka, T.; Miyake, M. *J. Phys. Chem. B* **1999**, *103*, 3818.

(18) Sarikaya, M.; Tamerler, C.; Jen, A. K. Y.; Schulten, K.; Baneyx, F. *Nature Materials* **2003**, *2*, 577.

(19) Whaley, S. R.; English, D. S.; Hu, E. L.; Barbara, P. F.; Belcher, A. M. *Nature* **2000**, *405*, 665.

(20) Naik, R. R.; Stringer, S. J.; Agarwal, G.; Jones, S. E.; Stone, M. O. *Nature Materials* **2002**, *1*, 169.

(21) Klem, M. T.; Willits, D.; Solis, D. J.; Belcher, A. M.; Young, M.; Douglas, T. *Advanced Functional Materials* **2005**, *15*, 1489.

(22) Gugliotti, L. A.; Feldheim, D. L.; Eaton, B. E. *Science* **2004**, *304*, 850.

(23) Gray, J. J. *Current Opinion in Structural Biology* **2004**, *14*, 110.

(24) Oren, E. E.; Tamerler, C.; Sarikaya, M. *Nano Lett.* **2005**, *5*, 415.

(25) Seker, U. O. S.; Wilson, B.; Dincer, S.; Kim, I. W.; Oren, E. E.; Evans, J. S.; Tamerler, C.; Sarikaya, M. *Langmuir* **2007**, *23*, 7895.

(26) Goede, K.; Busch, P.; Grundmann, M. *Nano Lett.* **2004**, *4*, 2115.

(27) Ciacchi, L. C.; Mertig, M.; Seidel, R.; Pompe, W.; De Vita, A. *Nanotechnology* **2003**, *14*, 840.

(28) Murray, C. B. *Science* **2009**, *324*, 1276.

(29) Zheng, H. M.; Smith, R. K.; Jun, Y. W.; Kisielowski, C.; Dahmen, U.; Alivisatos, A. P. *Science* **2009**, *324*, 1309.

(30) Qiu, S. R.; Wierzbicki, A.; Orme, C. A.; Cody, A. M.; Hoyer, J. R.; Nancollas, G. H.; Zepeda, S.; De Yoreo, J. J. *Proc. Natl. Acad. Sci.* **2004**, *101*, 1811.

(31) Meybeck, A.; Windle, J. J. *Photochemistry and Photobiology* **1969**, *10*, 1.

Chapter 4

4 MORPHOLOGY-CONTROLLED SYNTHESIS OF PLATINUM NANOCRYSTALS WITH SPECIFIC PEPTIDES

4.1 Introduction

The physical and chemical properties of nanocrystals (NCs) strongly depend on their sizes and morphologies.[1-3] One notable example is that noble metal NCs of various shapes have been reported to demonstrate different catalytic properties as a result of the distinct crystallographic facets displayed on the NC surfaces, which have been proven to exhibit distinct catalytic properties by affecting the molecular adsorption and desorption processes in a reaction.[4-19] For example, Pt NCs have attracted enormous interest due to their excellent catalytic activity in a wide range of reactions. It has been reported that the Pt NC morphology has significant effect on the oxygen reduction (ORR) activity due to different adsorption rates of sulfate ions on different low index facets such as (100), (110) and (111) faces;[20-22] and that Pt NCs of distinct morphologies exhibit different specific electrochemical surface areas (ECSAs) that affect the ORR efficiency.[23] Various synthetic strategies have been developed to obtain Pt NCs with different morphologies. Using low molecular surfactants or polymers as stabilizing agents and H_2 or $NaBH_4$ as the reducing agent, Pt NCs of different morphologies such as cubes and tetrahedrons have been synthesized at room temperature.[24-27] Pt NCs of novel shapes with high index facets have also been demonstrated with excellent catalytic activities.[14,16,28-31] More recently biomacromolecules, including proteins, peptides, RNAs and DNAs that have specific binding ability to target inorganic materials, have been demonstrated to have the

capability to direct the formation of inorganic NCs.[32-37] Notably, peptide sequence selected from a random peptide library has been shown to have specific binding ability to target materials,[38] thus can perform as capping agent in the NC synthesis. The synthesis of Ag, Pd and some semiconductor NCs have been studied by using specific peptides as the capping agents, although the degree of synthetic control in biomimetic approaches has yet to be improved. Our group has recently demonstrated peptide-regulated synthesis of ultrasmall Pt NCs with atomic layer control.[39-42]

Here we demonstrate the synthesis of water dispersable Pt NCs with controllable multipod structure under mild reaction conditions. The stabilizing agent used was a peptide selected with phage display technique against Pt wires. Using potassium tetrachloroplatinate (K_2PtCl_4) as the precursor and sodium borohydride ($NaBH_4$) as the reducing agent, the reaction was conducted in an aqueous solution at room temperature. We note that multipod Pt NCs had been reported before using chemical capping agents, and at much higher temperatures.[18,19] In our synthetic process, the addition of $NaBH_4$ was achieved by slow injection through a computer controlled syringe pump, so that the growth kinetics of NCs was controllable and observable. The as-synthesized Pt NCs displayed a uniform multipod-like morphology with high yield. It was also observed that the pod length could be tuned by altering the reaction kinetics. Electrochemical characterizations were also carried out to evaluate the electrocatalytic activity of the as-synthesized multipod Pt NC and compared with commercial Pt black.

4.2 Experimental

4.2.1 Selection, synthesis and characterization of peptide

The peptide was selected against Pt wire (Diameter: 0.25mm, 99.99%, Aldrich) from Ph.D.-7 library (New England Biolabs) as described in detail in Refs. 18b and 19. After the 3rd round selection, the sequence BP7A emerged as a strong binder. Peptides of the selected sequences were synthesized with a CS 336X synthesizer (C S Bio), characterized using a Shimadzu 2010 EV Liquid Chromatography Mass Spectrometer (LC/MS) and purified on a Beckman–Coulter Gold High Performance Liquid Chromatography (HPLC).

4.2.2 Synthesis, growth kinetics and characterization

In a typical Pt NC synthesis, potassium tetrachloraplatinate (II) (K_2PtCl_4, 99.9+%, Aldrich) stock of aqueous solution (10 mM) was prepared and aged for 2 days before use. K_2PtCl_4 stock solution (400 μL) and peptide solution (depending on the concentration) were mixed and diluted with deionized water (Aqua, 18 MΩ) to keep the K_2PtCl_4 concentration at 1 mM. The solution was stirred for at least 5 min before the reaction. Reductant solution was prepared by dissolving sodium borohydride ($NaBH_4$, 99.99%, 8 mg, Aldrich) in deionized water (10 mL). The $NaBH_4$ solution was immediately used after preparation due to the fast decomposition of $NaBH_4$. Computer programmed syringe pump was used to inject the $NaBH_4$ solution with injection rate at 10 μL/min. All of the above procedures were conducted at room temperature. Aliquots of reaction solution (60 μL) were taken out at different time points and immediately used to prepare TEM samples by pipetting the solution onto the carbon coated copper grids. The TEM samples were dried in atmosphere before taking images. TEM images were taken on FEI CM 120

microscope operated at 120 kV. High resolution TEM images were captured on FEI TITAN microscope operated at 300 kV.

4.2.3 Electrochemical characterization

In the electrochemical study of the NCs' catalytic property, Pt NCs were centrifuged for 3 times and then redispersed in water. The weight concentration of Pt in solution was determined by ICP-OES. According to the obtained Pt concentrations, solutions were diluted to similar concentrations and pipetted (4 μL) onto the glassy carbon electrode. Loading amount of Pt can be calculated with the Pt concentration and volume of the solution. After the solution totally dried, Nafion 117 aqueous (Aldrich, 0.1 wt.%, 8 μL) solution was pipetted onto the GCE (Bioanalytical Systems, Inc.), covering the electrode of 3 mm in diameter. The solution was then dried in a 85 °C oven followed with a 10 min cooling at room temperature before testing. The CV was carried out in oxygen saturated 0.5 M H_2SO_4 electrolyte in a three electrode electrochemical cell with Ag/AgCl electrode (Bioanalytical Systems, Inc.) as reference electrode and 0.25 mm Pt wire (Aldrich) as counter electrode. The electrode was activated by potential sweeping between -0.2 V and 1.6 V in 0.5 M H_2SO_4 electrolyte at the sweep rate of 100 mV/s to remove impurities on the working electrode. The CV curves were recorded between -0.18 V and 1.2 V at the sweep rate of 50 mV/s. The current in I-E curve was normalized with calculated ECSA and used to obtain the j-E curve.

4.3 Results and discussion

4.3.1 Peptide molecules

4.3.1.1 Characterization of peptide molecules

The peptide Ac-Thr-Leu-His-Val-Ser-Ser-Tyr-$CONH_2$ (termed BP7A, MW: 846.93) was selected from a Ph.D. 7 Library after the 3rd round selection against Pt wire,[42] and synthesized using solid state peptide synthesizer in a modified protocol with N-terminal acylation and C-terminal amidation.

The peptide was characterized by Shimadzu 2010 EV Liquid Chromatography Mass Spectrometer (LC/MS) and was purified with Beckman-Coulter Gold high performance liquid chromatography (HPLC). From the LC and MS spectra shown in Fig. 4.1, the purity is higher than 95%.

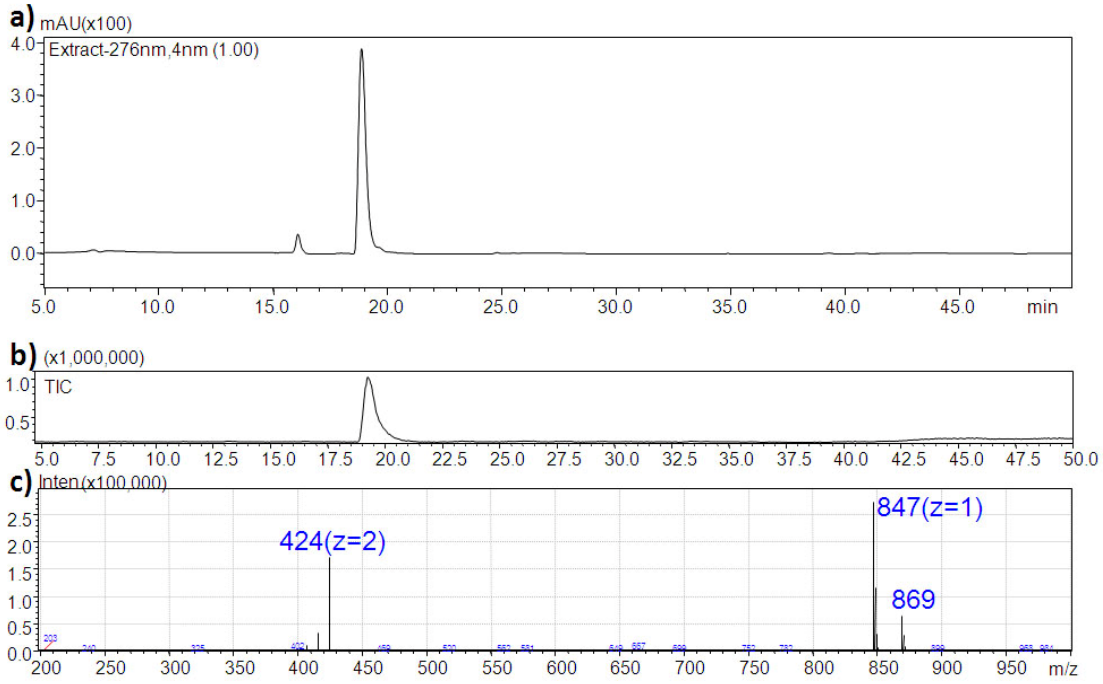

Figure 4.1 (a) Liquid chromatography (LC) of the BP7A peptide. (b) Mass detected of samples eluted from LC. (c) Mass spectrum of the samples eluted at about 19.5 min.

4.3.1.2 Integrity of peptide molecules

Peptide BP7A was incubated with reactants $NaBH_4$ and K_2PtCl_4 separately for up to 3 hours. In the mixed solution of BP7A and $NaBH_4$, the concentrations of BP7A and $NaBH_4$ are 1 mg/mL and 1 mM, respectively. In mixed solution of BP7A and K_2PtCl_4, the concentrations are 1 mg/mL and 1 mM, respectively. The LC-MS results shown in Fig. 4.2 indicate that the peptide did not degrade or react with the reactants prior to reaction (Fig. 4.2 a-e), and that most peptides stayed intact after the reaction (Fig. 4.2 c, f).

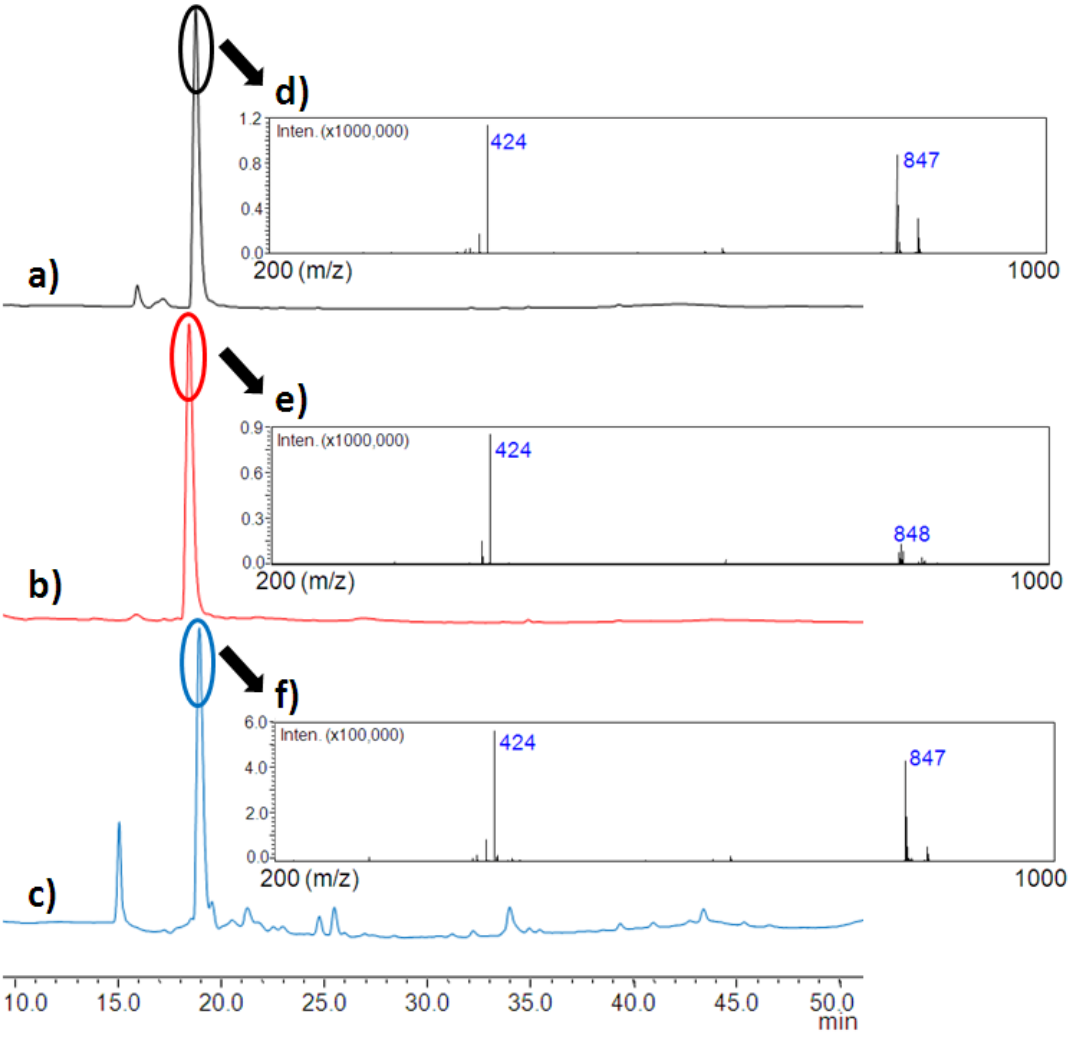

Figure 4.2 (a) is the LC chromatogram of the mixed solution of 1 mg/mL BP7A and 1 mM $NaBH_4$ after incubation of 3 h. (b) is the LC chromatogram of the mixed solution of 1 mg/mL BP7A and 1 mM K_2PtCl_4. (c) is the LC chromatogram of the supernatant of a post-reaction solution. (d, e, f) are the mass spectra at the time when peaks appeared.

4.3.2 Synthesis of Pt NCs

The highly uniform multipod Pt NCs were synthesized by slowly injecting $NaBH_4$ solution into the K_2PtCl_4/BP7A mixed solution with a syringe pump at controllable rates, while at the same time keeping the reaction solution strongly stirred. The color of the solution evolved from clear to light brown and finally to dark black. The molar ratio between precursor K_2PtCl_4 and peptide was changed to achieve different morphologies. The Fig. 4.3, a-d, shows the as-synthesized Pt NCs with different molar ratios between K_2PtCl_4 and peptide (i.e., by varying the peptide concentration while keeping the K_2PtCl_4 concentration constant). The transmission electron microscope (TEM) samples were prepared after 1 h of reaction. The control reaction without adding peptide is shown in Fig. 4.4. The typical crystals obtained without peptide added are polycrystalline and with hyperbranched morphologies with an average size around 20 nm. Negative controls with non-relevant peptides were demonstrated to exhibit no effect on Pt NC growth.[42] With the introduction of BP7A peptide, typical crystals observed have a multipod morphology with the average size down to 10 nm, as shown in Fig. 4.3 a. The term multipod is used because bi-pod, tri-pod and tetra-pod NCs coexist. With the increasing peptide concentrations (Fig. 4.3, a-c, 22.5-100 μg/mL), it was found that the length of the pods decreased from ca. 6 nm to ca. 1 nm. At sufficiently high peptide concentrations (e.g., 250 μg/mL, Fig. 4.3 d) multipod NCs ceased to exist, instead, the typical Pt NCs at high

peptide concentrations displayed a nearly spherical shape with an average size around 2.5 nm. It was also observed that the dispersity the Pt NCs in water improved with increasing peptide concentration.

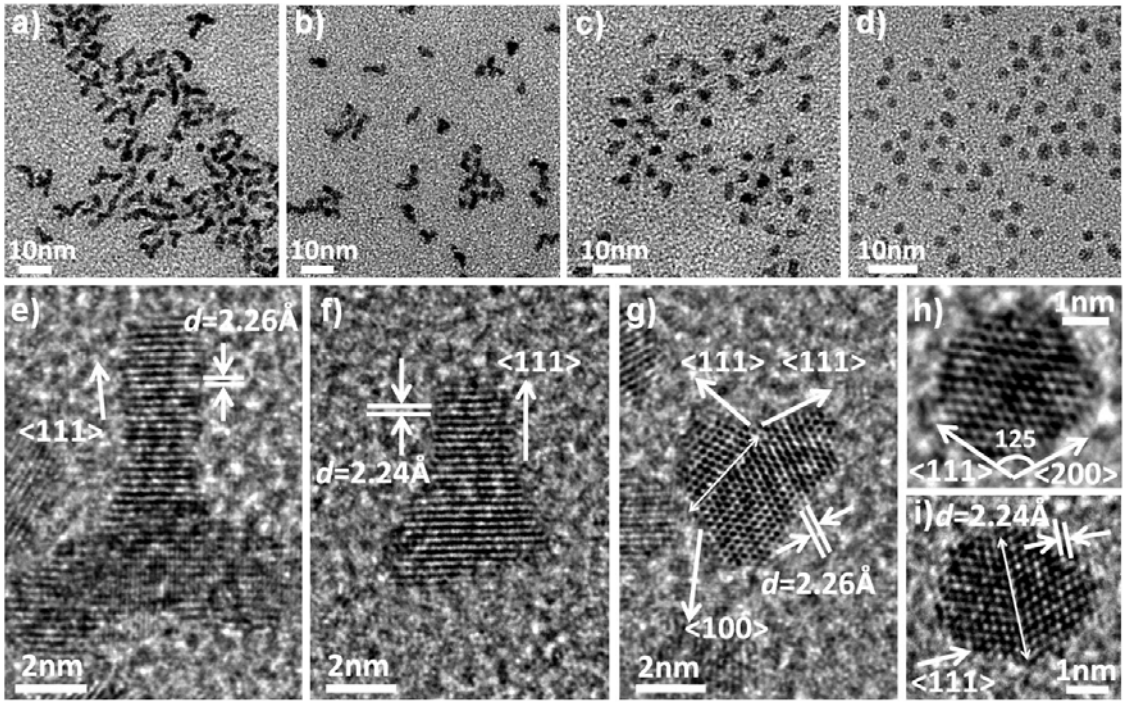

Figure 4.3 (a-d) TEM images of Pt NCs from reactions with 22.5, 50, 100, 250 μg/mL peptide concentrations, respectively. (e-g) are HRTEM images of Pt NCs from reactions with 22.5, 50, 100 μg/mL BP7A. (h-i) are crystals from reaction with 250 μg/mL BP7A. The double headed arrows indicate the twin planes.

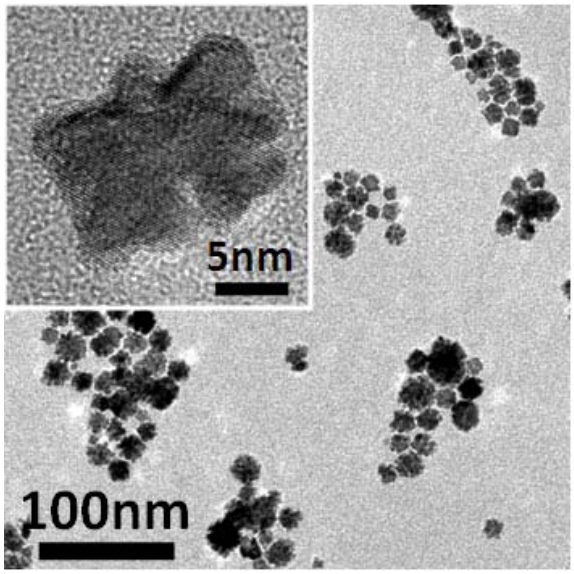

Figure 4.4 TEM image of the Pt NCs from control experiment without adding any peptide molecules.

Lattice analysis with high-resolution TEM (HRTEM) further revealed the single crystal nature of the multipod Pt NCs, and that most of the pods grew along <111> direction with the d spacing of 2.26 Å correspondingly. Some pods were found to grow along <100> directions. Interestingly, we did not observe any pods growing along <110> direction. For metals with a face-centered cubic (FCC) structure, there is usually an energetic sequence of $\gamma(111) < \gamma(100) < \gamma(110)$ for the low index facets.[43] During the synthesis of NCs, capping agent usually functions as the surface energy "modifier" to control the shape of the NCs, as well as prevent NC aggregation.[1,44] Our studies indicate that the Pt-binding peptide served the same role as a capping agent, but with preferential binding to (110) facets. At low peptide concentrations, the peptide molecules selectively bound to (110) facets and lowered their surface energy, and therefore promoted the growth along the <111> and <100> directions. At higher peptide concentrations, as there

were more than enough peptide molecules to cover the (110) facets, excessive peptides also bound to (111) and (100) facets, leading to convergence of surface energies. This can explain the resulting less distinctive multipod structures (Fig. 4.3, f and g). At sufficiently high peptide concentrations, when there were enough peptide molecules to bind to all facets, growth along all directions were inhibited, leading to the spherical morphology (Fig. 4.3, h and i).

It is also worth noting that twinning effect was frequently observed in the Pt NCs obtained with higher peptide concentrations, which may enhance the formation of tri-pod and bi-pod structures. Figure 4.3, g and i, shows the twin boundaries formed with the (111) twinning plane taking along <110> zone axis. It has been suggested that slow growth kinetics may lead to the formation of twin boundaries in NCs.[1] In our previous studies, it was demonstrated that the peptide molecules would greatly slow down the growth rate of Pt NCs.[42] Here, the retarded growth rate may lead to the frequently observed formation of twin boundaries at higher peptide concentrations. Bipod and tripod NCs were commonly found in the multipod NCs, as shown in Fig. 4.5.

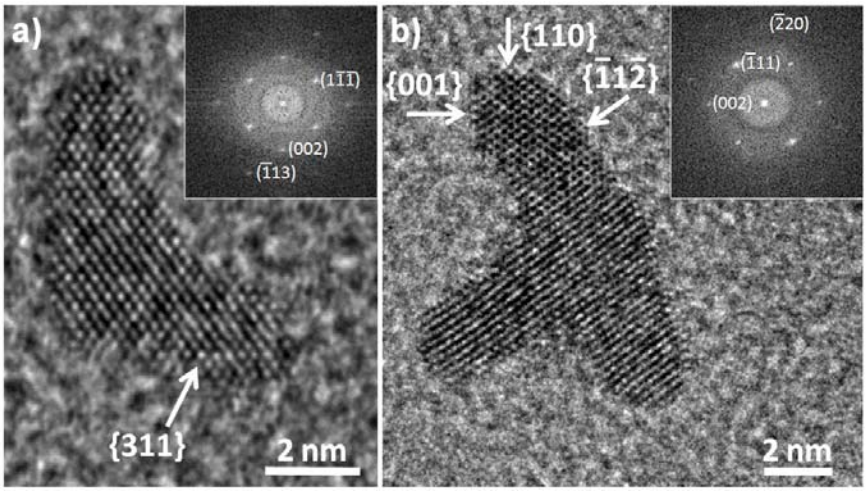

Figure 4.5 (a) and (b) are high resolution image of the bipod and tripod, respectively, capped by BP7A molecules. Insets are Fast Fourier Transformation of the HRTEM images, showing existence of higher index facets along the pod surface.

4.3.3 Synthesis of Pt NCs

To confirm the hypothesis on the growth mechanism of the peptide modulated NC formation, we investigated the time and shape evolution of Pt NCs with difference peptide concentrations (25, 50, 100 and 200 μg/mL), as shown in Fig. 4.6. In this set of experiments, aliquots of reaction solution were taken out during the $NaBH_4$ injection and immediately used to prepare TEM samples. The same procedure was also carried out for control experiment without the peptides (Fig. 4.7).

Without peptide molecules, the obtained Pt NCs did not exhibit a well-defined shape at the early stage at 1 min, and seemed to be the coalescence of smaller particles (nuclei).[45,46] With the elapsing of time, the NCs started to grow into bigger hyperbranched polycrystalline NCs. In the presence of peptide molecules, the growth rate was significantly slowed down. For all peptide concentrations shown in Fig. 4.6, smaller NCs (ca. 2 nm) were observed at the early stage, following which, the NCs slowly evolved into single-crystal, multipod structures.

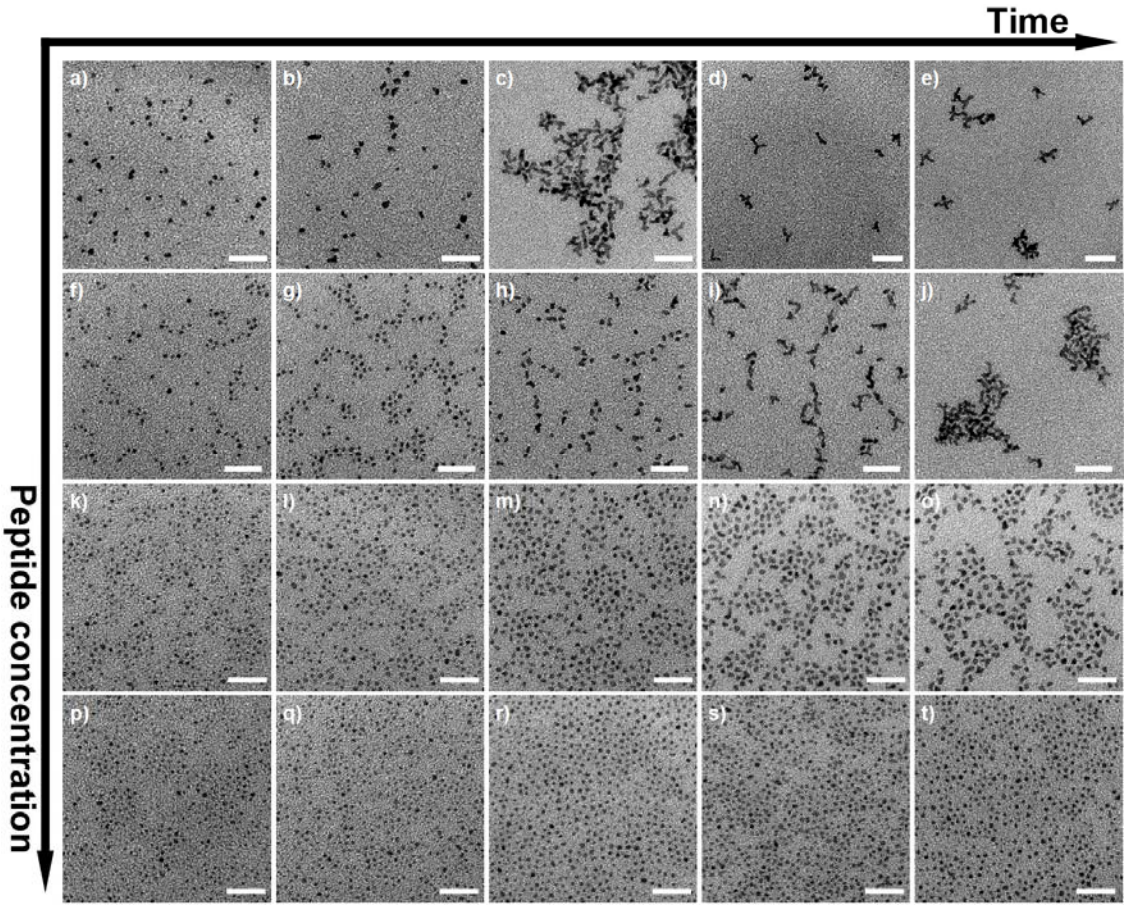

Figure 4.6 TEM images showing the shape evolution of Pt NCs taken at 1, 2, 4, 6, and 10 min of the reaction with 25 µg/mL (a-e), 50 µg/mL (f-j), 100 µg/mL (k-o) and 200 µg/mL (p-t) peptide concentrations, respectively. Scale bars: 20 nm.

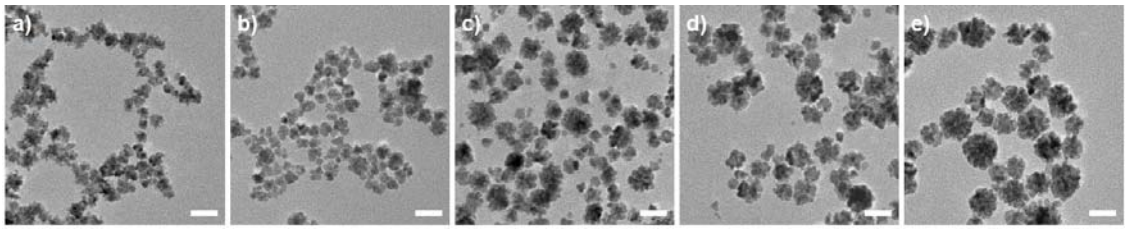

Figure 4.7 TEM images of Pt NCs taken at (a) 1 min, (b) 2 min, (c) 4 min, (d) 6 min and (e) 10 min after the start of $NaBH_4$ injection. Scale bar is 20 nm.

It was observed that the growth rate of Pt NCs decreased with increasing peptide concentration, which may be attributed to the increased deterrence of atom addition onto the nuclei due to the increased peptide coverage on NC surface. At low peptide concentration (e.g., 25 μg/mL, Fig. 4.6 a), majority of the Pt NCs were nearly spherical at the early stage of nucleation and growth. The NCs were slowly elongated and eventually evolved into multipod structure at the following growth stages (i.e., 2, 4, 6, and 10 min, see Fig. 4.6, b-e). On the molecular level, at this concentration, since the ratio of peptide to platinum was relatively low, peptides preferentially bound to (110) facets and detered the growth in <110> direction, leading to pod growth mostly along <111> and <100>. With increasing peptide concentration, the shape evolvement of NCs from sphere to multipod slowed down (Fig. 4.6, f to j), and the final resulting pod length also decreased, which can be attributed to the increased coverage of excessive peptide molecules on (111) and (100) facets. At a concentration of 200 μg/mL, all the crystals were nearly spherical, indicating the NCs were totally covered with peptide molecules so that there were no preferred growth directions.

4.3.4 Electrochemical properties of the Pt NCs

Electrochemical studies were carried out to evaluate the electrochemical surface area (ECSA) of these multipod Pt NCs for electrocatalytic applications as well as to reveal more structure-related properties of the resulting Pt NCs. The as-synthesized Pt NCs of various pod lengths were centrifuged and then redispersed in water to eliminate potential precursor residues in solution. The weight concentration of Pt in the re-suspended solution was determined by inductively coupled plasma optical emission spectrometry (ICP-OES). The NC solutions were pipetted onto polished glassy carbon electrode (GCE),

dried and then covered with Nafion solution. Cyclic voltammetry (CV) was performed in a three-electrode electrochemical cell. The electrolyte was 0.5 M sulfuric acid (H_2SO_4) solution saturated with oxygen. The morphologies of the Pt NCs that were used for the electrochemical measurement were shown in Fig. 4.8.

The Pt NCs used in electrochemical test were synthesized with conditions listed in Table 4.1. The loading amount was determined by the measured Pt weight concentration and loading volume. The calculated loading amount of Pt black, as-synthesized long pod, short pod and near spherical NCs are 4, 2.108, 1.463, and 1.994 μg, respectively.

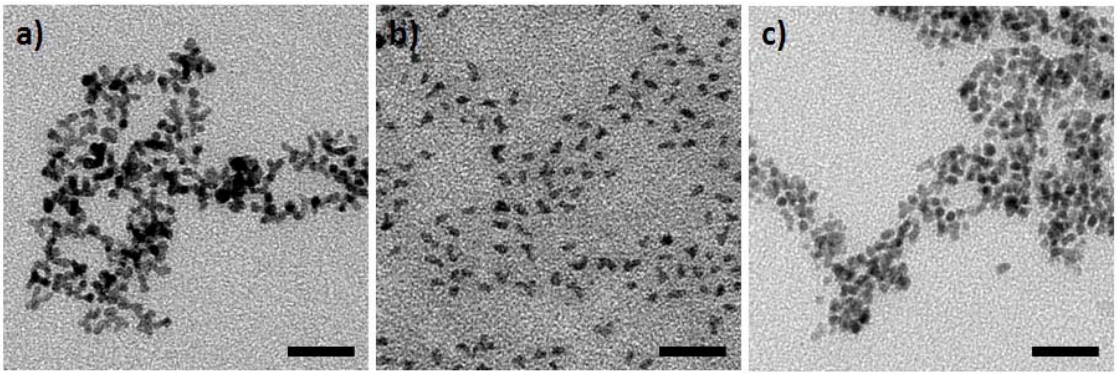

Figure 4.8 TEM images of the (a) long pod, (b) short pod and (c) near spherical nanocrystals used in electrochemical measurement. Scale bar is 20 nm.

Table 4.1 Synthetic condition, and sizes of Pt nanocrystals with different morphologies.

Pt catalyst	K_2PtCl_4 (mM)	$NaBH_4$ (mM)	BP7A (μg/mL)	Size (nm)
Long pod	1	1	25	5.0 ± 0.5 (pod)
Short pod	1	1	100	3.3 ± 0.4

				(pod)
Near spherical	0.5	1	100	2.8 ± 0.3

Fig. 4.9 shows the CV curves recorded by using Pt NCs of different morphologies as cathode catalyst. The potential was swept between -0.18 and 1.2 V versus Ag/AgCl reference electrode with a sweep rate of 50 mV/s. In the hydrogen adsorption/desorption region between -0.18 V and 0.2 V, the ECSA can be estimated by integration of the I-E curve.

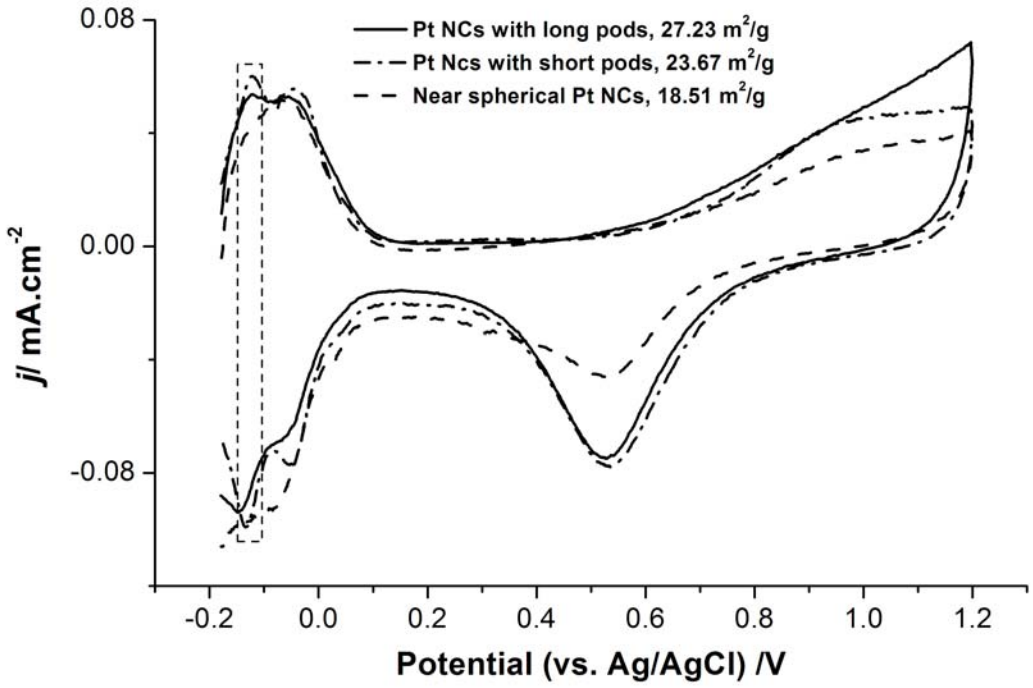

Figure 4.9 CV curves of Pt with different morphologies (Solid curve: Pt NCs with long pods; Dash-dot curve: Pt NCs with short pods; and dash curve: nearly spherical Pt NCs). The curves were recorded by scanning from -0.18 V to 1.2 V at a sweeping rate of 50 mV/s.

The determination of ECSA with the approach of hydrogen adsorption has been well studied. The electric charge density for hydrogen adsorption is known as 210 $\mu C/cm^2$ (denoted by Q_0) assuming a monolayer hydrogen adsorption on Pt surface. The electric charge induced by hydrogen adsorption (denoted by Q) can be calculated by integrating the area in the hydrogen adsorption/desorption region between -0.18 and 0.2 V after the subtraction of double-layer charging. Thus, the ECSA can be derived by the equation $ECSA=0.5Q/(m \cdot Q_0)$, where m is the loading amount of Pt on glassy carbon electrode.

It was found that the as-synthesized Pt NCs demonstrate higher ECSAs than the commercial Pt black in our set up. The Pt NCs with long pods exhibited ECSA around 27.23 m^2/g, almost twice that of the Pt black which showed a specific ECSA of about 15.15 m^2/g (Fig. 4.10). We also found that with the decreasing pod length, the specific ECSA of the as-synthesized Pt NCs also decreased, but still remained higher than that of the Pt black. The observed decreasing ECSA might result from the relatively more residue BP7A molecules remained on the Pt NCs with shorter pods as they were synthesized with higher peptide concentrations. The peaks at -0.13 V (Fig. 4.9) in both forward and backward sweep have been attributed to the hydrogen desorption/adsorption on (110) crystallographic facets.[20-22] We can see that multipod Pt NCs (solid and dash-sot curves in Fig. 4.9) showed distinctive (110) facets features when compared to spherical Pt NCs (dash curve in Fig. 4.9). This observation is consistent with the previously proposed growth mechanism that BP7A peptide molecules preferably bound to and lower the surface energy of (110) facets, which left higher ratio of (110) facets on the NC pod surface. We note that the exact mechanism by which the peptide molecules prefer to bind to (110) facets is not clear at current stage. Further studies especially that involve the

simulation and calculation of binding energy of the peptides to different low index Pt facets are currently underway to better understand the mechanism of the binding. In addition, the multipod Pt NCs showed higher oxygen reduction (~ 0.53 V) current densities than that of the nearly spherical Pt NCs. This may be explained by the existence of the high-index facets on multipod Pt NCs (Fig. 4.10) which contributed to higher adsorption of O_2 molecules.[16]

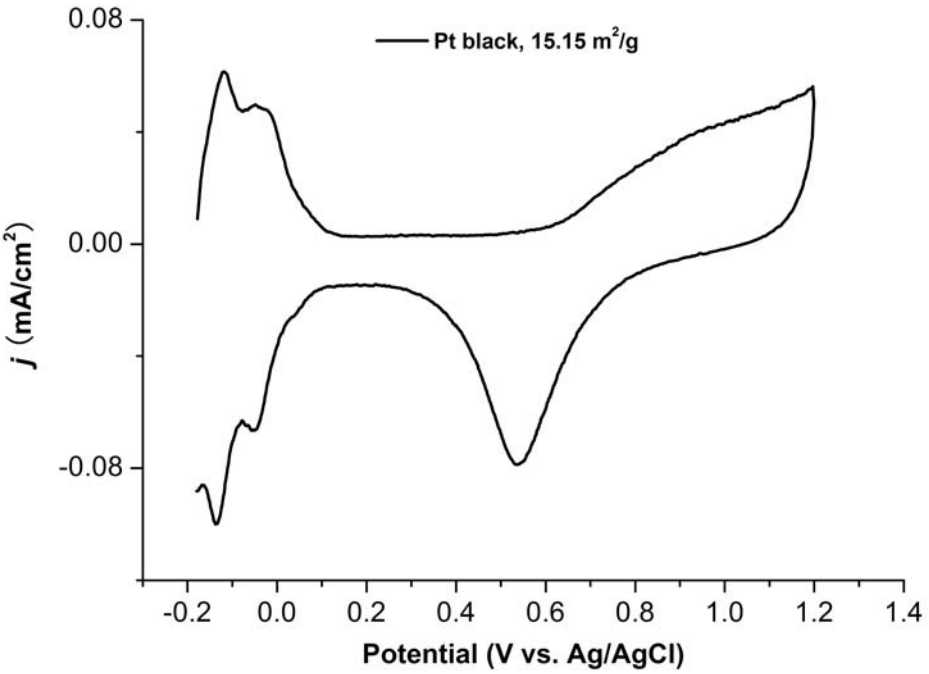

Figure 4.10 CV curve of Pt black. Curve was recorded by scanning from -0.18 V to 1.2 V at the sweep rate of 50 mV/s.

4.4 Conclusion

In summary, we have demonstrated that the peptide molecules selected with phage display technique could be used to regulate the Pt NC growth kinetics therefore control the resulting NC morphologies in aqueous solution at room temperature. By varying the peptide concentration, nearly spherical Pt NCs and Pt NCs of multipod structures with

different pod lengths could be rationally achieved. The shape evolution studies of NCs suggested that the peptide molecules preferably bind onto (110) facets, resulting in multipod structures with preferential pod growth direction along <111> and <100>. It was also demonstrated that the facet-specific selectivity plays a less important role with increasing peptide concentrations, leading to the transformation of multipod to a nearly spherical morphology at high peptide concentrations. The electrochemical study of different shaped Pt NCs showed that the as-synthesized multipod NCs demonstrate high ECSAs and can potentially serve as high performance catalysts in electrocatalytic applications, such as PEM fuel cells. More importantly this study demonstrated a potential pathway to rationally synthesize NCs with selectively exposed facets with specific peptide molecules for the first time, and therefore open up many new opportunities in nanocatalysts design and studies.

[References/Bibliography]

(1) Xia, Y.; Xiong, Y. J.; Lim, B.; Skrabalak, S. E. *Angew Chem Int Edit* **2009**, *48*, 60.

(2) Link, S.; El-Sayed, M. A. *J Phys Chem B* **1999**, *103*, 8410.

(3) Talapin, D. V.; Shevchenko, E. V.; Bodnarchuk, M. I.; Ye, X. C.; Chen, J.; Murray, C. B. *Nature* **2009**, *461*, 964.

(4) Bell, A. T. *Science* **2003**, *299*, 1688.

(5) Narayanan, R.; El-Sayed, M. A. *J Phys Chem B* **2005**, *109*, 12663.

(6) Lopez, N.; Norskov, J. K.; Janssens, T. V. W.; Carlsson, A.; Puig-Molina, A.; Clausen, B. S.; Grunwaldt, J. D. *J Catal* **2004**, *225*, 86.

(7) Hernandez, J.; Solla-Gullon, J.; Herrero, E.; Aldaz, A.; Feliu, J. M. *Journal of Physical Chemistry C* **2007**, *111*, 14078.

(8) Xu, R.; Wang, D. S.; Zhang, J. T.; Li, Y. D. *Chemistry-an Asian Journal* **2006**, *1*, 888.

(9) Claus, P.; Hofmeister, H. *J Phys Chem B* **1999**, *103*, 2766.

(10) Bratlie, K. M.; Lee, H.; Komvopoulos, K.; Yang, P. D.; Somorjai, G. A. *Nano Letters* **2007**, *7*, 3097.

(11) Herricks, T.; Chen, J. Y.; Xia, Y. N. *Nano Letters* **2004**, *4*, 2367.

(12) Lear, T.; Marshall, R.; Lopez-Sanchez, J. A.; Jackson, S. D.; Klapotke, T. M.; Baumer, M.; Rupprechter, G.; Freund, H. J.; Lennon, D. *J Chem Phys* **2005**, *123*.

(13) Silly, F.; Castell, M. R. *Phys Rev Lett* **2005**, *94*.

(14) Lim, B. W.; Lu, X. M.; Jiang, M. J.; Camargo, P. H. C.; Cho, E. C.; Lee, E. P.; Xia, Y. N. *Nano Letters* **2008**, *8*, 4043.

(15) Ma, Y. Y.; Kuang, Q.; Jiang, Z. Y.; Xie, Z. X.; Huang, R. B.; Zheng, L. S. *Angew Chem Int Edit* **2008**, *47*, 8901.

(16) Lim, B.; Jiang, M. J.; Camargo, P. H. C.; Cho, E. C.; Tao, J.; Lu, X. M.; Zhu, Y. M.; Xia, Y. A. *Science* **2009**, *324*, 1302.

(17) Habas, S. E.; Lee, H.; Radmilovic, V.; Somorjai, G. A.; Yang, P. *Nature Materials* **2007**, *6*, 692.

(18) Chen, J. Y.; Herricks, T.; Xia, Y. N. *Angew Chem Int Edit* **2005**, *44*, 2589.

(19) Teng, X. W.; Yang, H. *Nano Letters* **2005**, *5*, 885.

(20) Kuzume, A.; Herrero, E.; Feliu, J. M. *J Electroanal Chem* **2007**, *599*, 333.

(21) Markovic, N.; Gasteiger, H.; Ross, P. N. *J Electrochem Soc* **1997**, *144*, 1591.

(22) Markovic, N. M.; Gasteiger, H. A.; Ross, P. N. *Journal of Physical Chemistry* **1995**, *99*, 3411.

(23) Lin, Z. H.; Lin, M. H.; Chang, H. T. *Chem-eur J* **2009**, *15*, 4656.

(24) Ahmadi, T. S.; Wang, Z. L.; Green, T. C.; Henglein, A.; ElSayed, M. A. *Science* **1996**, *272*, 1924.

(25) Lee, H.; Habas, S. E.; Kweskin, S.; Butcher, D.; Somorjai, G. A.; Yang, P. D. *Angew Chem Int Edit* **2006**, *45*, 7824.

(26) Yu, Y. T.; Xu, B. Q. *Chinese Sci Bull* **2003**, *48*, 2589.

(27) Lee, I.; Morales, R.; Albiter, M. A.; Zaera, F. Proceedings of the National Academy of Sciences of the United States of America **2008**, 105, 15241.

(28) Tsung, C. K.; Kuhn, J. N.; Huang, W. Y.; Aliaga, C.; Hung, L. I.; Somorjai, G. A.; Yang, P. D. *J Am Chem Soc* **2009**, *131*, 5816.

(29) Wang, C.; Daimon, H.; Lee, Y.; Kim, J.; Sun, S. *J Am Chem Soc* **2007**, *129*, 6974.

(30) Tian, N.; Zhou, Z. Y.; Sun, S. G.; Ding, Y.; Wang, Z. L. *Science* **2007**, *316*, 732.

(31) Zhou, Z. Y.; Tian, N.; Huang, Z. Z.; Chen, D. J.; Sun, S. G. *Faraday Discuss* **2008**, *140*, 81.

(32) Douglas, T.; Stark, V. T. *Inorg Chem* **2000**, *39*, 1828.

(33) Prozorov, T.; Mallapragada, S. K.; Narasimhan, B.; Wang, L. J.; Palo, P.; Nilsen-Hamilton, M.; Williams, T. J.; Bazylinski, D. A.; Prozorov, R.; Canfield, P. C. *Adv Funct Mater* **2007**, *17*, 951.

(34) Naik, R. R.; Stringer, S. J.; Agarwal, G.; Jones, S. E.; Stone, M. O. *Nature Materials* **2002**, *1*, 169.

(35) Gugliotti, L. A.; Feldheim, D. L.; Eaton, B. E. *Science* **2004**, *304*, 850.

(36) Ma, N.; Sargent, E. H.; Kelley, S. O. *Nature Nanotechnology* **2009**, *4*, 121.

(37) Choi, J. H.; Chen, K. H.; Han, J. H.; Chaffee, A. M.; Strano, M. S. *Small* **2009**, *5*, 672.

(38) Whaley, S. R.; English, D. S.; Hu, E. L.; Barbara, P. F.; Belcher, A. M. *Nature* **2000**, *405*, 665.

(39) Pacardo, D. B.; Sethi, M.; Jones, S. E.; Naik, R. R.; Knechtt, M. R. *Acs Nano* **2009**, *3*, 1288.

(40) Sarikaya, M.; Tamerler, C.; Jen, A. K. Y.; Schulten, K.; Baneyx, F. *Nature Materials* **2003**, *2*, 577.

(41) Flynn, C. E.; Mao, C. B.; Hayhurst, A.; Williams, J. L.; Georgiou, G.; Iverson, B.; Belcher, A. M. *J Mater Chem* **2003**, *13*, 2414.

(42) Li, Y.; Whyburn, G. P.; Huang, Y. *J. Am. Chem. Soc.* **2009**, *131*, 15998.

(43) Wang, Z. L. *J Phys Chem B* **2000**, *104*, 1153.

(44) Park, J.; Joo, J.; Kwon, S. G.; Jang, Y.; Hyeon, T. *Angew Chem Int Edit* **2007**, *46*, 4630.

(45) Zheng, H. M.; Smith, R. K.; Jun, Y. W.; Kisielowski, C.; Dahmen, U.; Alivisatos, A. P. *Science* **2009**, *324*, 1309.

(46) Murray, C. B. *Science* **2009**, *324*, 1276.

Chapter 5

5 SYNTHESIS OF BIMETALLIC PLATINUM-PALLADIUM CORE-SHELL NANOCRYSTALS AND THEIR HIGH ELECTROCATALYTIC ACTIVITY MODULATED BY PALLADIUM SHELL THICKNESS

5.1 Introduction

Noble metals (e.g. Pt, Pd, Rh, Ru, etc.) have attracted increasing interest as electrocatalysts for fuel cell applications.[1-3] Nanocrystals (NCs) of noble metals exhibit excellent catalytic activities on both cathode, towards oxygen reduction reaction (ORR), and anode, for electro-oxidation of fuel molecules, due to their large effective surface area and highly active surfaces which can be tailored by their sizes and morphologies.[4-7] Among all noble metal materials, Pt and Pd-based NCs are found to show the best catalytic performance in many types of fuel cells such as the alkaline fuel cell (AFC), proton exchange membrane fuel cell (PEMFC), and direct methanol fuel cell (DMFC).[8] DMFC has attracted great interest due to the high energy density released by methanol and its stability at various environmental conditions.[9-11] Pt-based catalysts were acknowledged as the most efficient catalysts in most DMFCs operated in acidic media and Pt NCs of different shapes and sizes have been studied to achieve better reaction kinetics occurring at both the anode and cathode.[12-17] However, anions in acidic media such as bisulfate anions can absorb on the Pt surface, can block the reaction sites, and lead to potential loss in ORR.[18] As a result, DMFCs operated in alkaline media have attracted considerable attention due to the improved reaction kinetics at both electrodes.[19,20] Interestingly, Pd NCs have been reported to demonstrate high activity and

low onset potential in methanol oxidation reaction in alkaline media.[21-23] In the meanwhile, Pt-Pd bimetallic nanostructures, including the core-shell structures and dendrite structures, have been synthesized and demonstrated enhanced electro-catalytic activity and durablity.[24-37] In specific, core-shell structured NCs have demonstrated higher durability, and lower over-potential when compared to pure Pt or pure Pd NCs at the cathode towards ORR in alkaline media.[38]

Bulk material (thin film) studies have demonstrated that coating Pd layers on Pt will modify the ORR reaction kinetics.[39,40] It has been suggested that the coated Pd layers can modify the density of states on Pt surface, which in turn changes the adsorption energy of O-containing species on Pd-Pt surface.[31,39] This modification may facilitate or deteriorate the catalytic performance, depending on the thickness of the Pd layer.[39] The study suggests the importance of Pd shell thickness in modulating the catalytic performance of Pt-Pd core-shell NCs. However, there is no report to date systematically studying the effect of Pd shell thickness on the electrocatalytic activities of Pt-Pd core-shell NCs. Herein, we report the synthesis of water-soluble Pt-Pd core-shell NCs with multipod morphology in aqueous solution. The deposition of Pd on Pt NCs was controlled to study the effect of Pd shell thickness on the catalytic activities of the Pt-Pd bimetallic NCs as both cathode (ORR) and anode (methanol oxidation) catalysts in alkaline media.

5.2 Experimental

5.2.1 Bimetallic NC synthesis

Pt core NCs were synthesized at room temperature in aqueous solution by reducing potassium tetrachloroplatinate (K_2PtCl_4, 1 mM) with sodium borohydride ($NaBH_4$).[41-44] Briefly described as bellow, mixed solution (4 mL) of K_2PtCl_4 and peptide Ac-Thr-Lue-

His-Val-Ser-Ser-Tyr-$CONH_2$ (termed BP7A, 25 μg/mL) was prepared and stirred for 5 min before injecting fresh-made $NaBH_4$ stock solution. The $NaBH_4$ solution (20 mM) was slowly introduced for 10 minutes using syringe pump at the rate of 10 μL/min. The reaction solution was strongly stirred for 1 hour before being centrifuged to collect the NCs. The Pt core NCs were washed twice with ultrapure water (18 MΩ) and re-dispersed in water (4 mL) to obtain Pt NC stock solution. The stock solution (2 mL) was diluted with water and mixed with Na_2PdCl_4 and trisodium citrate ($Na_3C_6H_5O_7$) as reducing agent to make a solution with 1 mM of Na_2PdCl_4 and 2 mM of $Na_3C_6H_5O_7$. The solution was then quickly heated to 92 ^oC and kept at the temperature for a desired period of time to synthesize Pt-Pd core-shell NCs with different Pd shell thickness. The reaction solution was centrifuged to collect the NCs. The NCs were washed with water twice and re-dispersed in water (200 μL).

The morphology of the NCs was characterized by high resolution transmission electron microscopy (HRTEM). The TEM samples were prepared by pipetting drops of reaction solution onto the TEM grid followed by immediate drying and washing with water. Energy dispersive X-ray spectrometer (EDS) spectra, and EDS line scanning profiles were captured on FEI TITAN scanning transmission electron microscopy (STEM) operated at 300 kV. EDS line scanning profile data were analyzed with Emispec Vision Software (FEI Company). High angle annular dark field scanning transmission electron microscopy (HAADF-STEM) and electron energy loss spectroscopy (EELS) were performed using an aberration-corrected 200 kV JEM2100F-Cs instrument, with a corrected probe size of about 0.1 nm, inner correction angle 62 mrad. The elemental and surface analysis was done with Omicron X-ray photoelectron spectroscopy (XPS). The

XPS samples were prepared by air-drying concentrated NC solutions on the silicon dioxide deposited with 20 nm thick Ag film.

5.2.2 Electrochemical Characterization

The weight concentration of the NCs was determined by inductively coupled plasma optical emission spectrometer (ICP-OES). The NC solutions were diluted to the same concentration for electrochemical characterization. For the ORR study, the weight concentration used is 0.15 μg/mL for all NCs including the commercially available Pt and Pd black. Nafion 117 (5%) was added into NC solution (0.15 μg/mL, 100 μL) to get a solution with 0.05% Nafion. The solution was sonicated for 15 min to disperse the NCs as well as the Nafion. The solution was pipetted (10 μL) onto a glassy carbon (GC) rotating disk electrode (Pine Instrumentation) with a diameter of 5 mm, so the metal loading is 1.5 μg. The solution was dried in air at room temperature. A three-electrode electrochemical cell was employed for the electrochemistry study by using Ag/AgCl as reference electrode (RE) and Pt wire as counter electrode (CE). Before electrochemical measurement, the electrode was activated by potential sweep between -0.2 and 1.5 V (vs. Ag/AgCl) in 0.5 M H_2SO_4 electrolyte at a rate of 100 mV/sec to remove the impurities and surfactant residues on NCs. The electrochemical surface area (ECSA) was determined by integrating hydrogen adsorption region (between -0.15 and 0.1 V) of CV sweep in 0.5 M H_2SO_4 between -0.2 and 1.2 V at a rate of 50 mV/s. For the kinetic study in alkaline media with RDE, polarization curves were recorded at different rotating speeds ranging from 400 to 3600 rpm in 0.1 M KOH electrolyte between -0.6 and 0.1 V, at the rate of 10 mV/s. The solution was bubbled with oxygen (O_2) gas to maintain O_2 saturation.

5.2.3 CO poisoning and Methanol oxidation reaction

The weight concentration is 0.5 mg/mL for all NCs with Nafion concentration at 0.05 %. The solution was pipetted (8 μL) onto a GC electrode with 3 mm diameter. For the carbon monoxide (CO) poisoning test, O_2 was bubbled all through the experiment at the rate of 50 mL/min and CO was introduced from 3 min at the rate of 5 mL/min. The flow rates of CO and O_2 were kept at the ratio of 1/10. Chronoamperometries were recorded at -0.25 V for half an hour in 0.1 M KOH electrolyte. The currents were normalized with the corresponding initial stabilized current i_0 before the introduction of CO. For the electro-oxidation of methanol in alkaline media, CV curves were recorded in 0.1 M KOH electrolyte with 1 M methanol. The potential was swept between -1 and 0.2 V at a rate of 100 mV/s.

5.3 Results and discussion

Pt-Pd core-shell NCs were synthesized in a two-step approach−the synthesis of Pt multipod seed NCs which was then followed by epitaxial growth of the Pd shell on the preformed Pt NCs, both in aqueous solution, as described in Section 2. The synthesis and growth mechanism of the Pt multipod NCs have been reported in our previous paper.[41]

5.3.1 Epitaxial growth of Pd on Pt core NCs

The reduction of Pd precursors is achieved by using weak reducing agent $Na_3C_6H_5O_7$ at elevated temperature. Upon reduction, Pd atoms hetero-nucleate on the Pt core to form core/shell structures. Multipod Pt NCs were synthesized and coated with Pd shell as shown in Fig. 5.1. The Pt core NCs (Fig. 5.1 a) were obtained by using 1 mM K_2PtCl_4, 0.5 mM $NaBH_4$, and 25 μg/mL BP7A with the experimental procedure described in methods and Ref. 1. Fig 5.1 (b-d) show the bimetallic NCs synthesized when refluxed at 92 ^oC for 60, 90, 120 minutes, respectively.

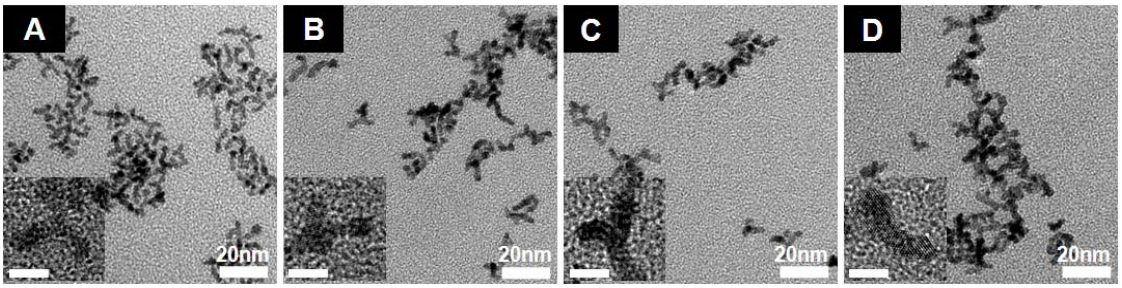

Figure 5.1 Pt-Pd core-shell NCs with long pod. (a) is preformed Pt core NCs with long pods, synthesized by using BP7A as capping agent. (b-d) are bimetallic Pt-Pd NCs with different Pd shell thicknesses by controlling the reaction time at 60, 90 and 120 min, respectively. Inset: HRTEM image of the NCs, scale bar: 5nm.

The epitaxial deposition of Pd on Pt NCs is visualized with HRTEM (Fig. 5.2). Statistical analysis of the pod diameter is based on 50 randomly picked NCs. The average pod diameter for the Pt core NCs is around 2.08 nm (Fig. 5.2 a), with increasing reaction time, the average pod diameter increases to 2.50, 3.01 and 3.31 nm after 30, 60 and 120 minutes of reaction, respectively, as shown in HRTEM in Fig. 1 b-d. Pod diameter mentioned here is defined as the span of the radial direction located the middle of a pod (between the tip and the crossover point of pods). The HRTEM images show that there is no obvious lattice contrast or orientation change at the boundary between Pt and Pd in the bimetallic NCs, indicating that the Pd is epitaxially grown onto the Pt cores (Fig. 5.2 f-h). At 30 min, according to the HRTEM, the pod grows from 9 layers to approximately 12 layers in <111> direction, implying slightly more than one monolayer coverage of Pd on Pt. Schematic in the inset of Fig. 5.2 f shows one pod covered with 1 atomic layer of Pd. As the time elapsed, the pod diameter, in <111> direction, increased to 14 atomic lays at 60 min, and 16 layers at 120 min as shown in Fig. 5.2 g,h, indicating the conformal

epitaxial growth of Pd on Pt. The as-synthesized bimetallic NCs are well dispersed in water without aggregation.

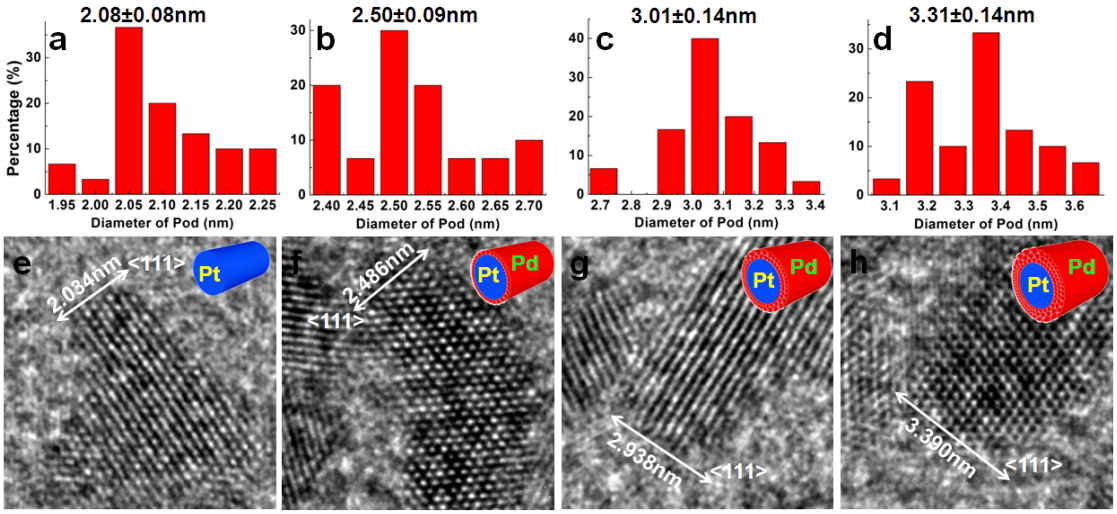

Figure 5.2 Statistical analysis and HRTEM images of pods showing the epitaxial deposition of Pd on Pt. (a) is statistical histogram of pod diameter (based on 50 random counts) of Pt core NCs. (b-d) are histograms of pod diameter of bimetallic Pt-Pd NCs with different Pd shell thicknesses by controlling the deposition time of 30, 60 and 120 minutes. (e-h) are HRTEM images of typical NCs corresponding to (a-d) samples. Insets in (e-h) are schematics of one pod with 0 to 3 Pd atomic layers.

Pt NCs with shorter pods were also synthesized (with higher BP7A concentration) and coated with Pd shell of different thicknesses, as shown in Fig. 5.3. The Pt core NCs were synthesized with 1 mM K_2PtCl_4, 0.5 mM $NaBH_4$, and 100 μg/mL BP7A. Fig. 5.3 (b-e) show the bimetallic NCs synthesized when refluxed at 92 ^oC for 30, 60, 90, 120 minutes, respectively. There is obvious change in morphology or dispersity with the formation of Pd shell. No morphology change or small Pd NCs were observed, suggesting slow and conformal heterogeneous nucleation of Pd shells on Pt NCs.

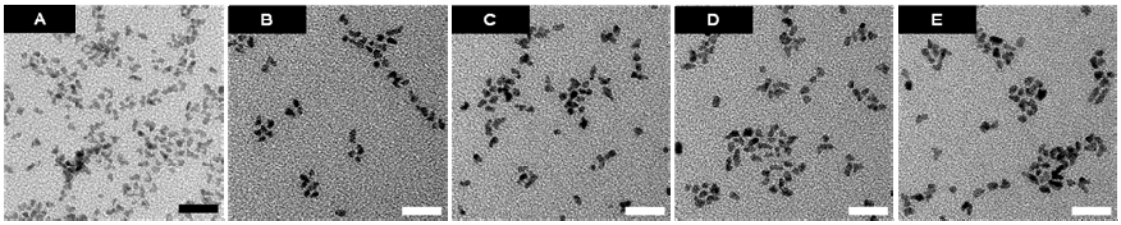

Figure 5.3 Pt-Pd core-shell NCs with short pod. (a) short pod Pt core NC. (b-e) Pt-Pd NCs synthesized with refluxing time of 30, 60, 90 and 120 minutes with 1mM Na_2PdCl_4 using (a) core NCs. Scale bars: 20 nm.

5.3.2 Uniform Pd deposition on individual Pt core NCs

In order to further confirm the uniformity of the deposited Pd shell on individual Pt core NCs, elemental analysis on individual NCs and elemental analysis of ensemble NCs were carried out and compared to each other. The elemental analysis on individual Pt-Pd NC was carried out by EDS on HRTEM, and elemental ratio of ensemble NCs in solution was determined by ICP-OES. The comparison of elemental ratios obtained by these two approaches can be used to evaluate the even deposition of Pd on Pt core NCs. According to the plot in Fig. 5.4 a, the Pd/Pt mass ratios of the ensemble NC solutions measured by ICP-OES on corresponding samples agree very well with the Pd/Pt ratios from EDS results on individual Pt-Pd NCs (average ratio from 15 randomly picked NCs from each sample), indicating that the Pd atoms deposited during the reaction were distributed with similar amount on each NC. The typical EDS spectra of individual NCs obtained with different reaction times were shown in Fig. 5.4 b. There is a gradual increase of the Pd characteristic peak at 2.7 keV on individual particles with increasing reaction time, indicating the increase of Pd shell coverage or thickness. No Pd NCs were found during the EDS studies, again suggesting the Pd was entirely deposited on the Pt core. HAADF-

STEM images in Fig. 5.4 d,e show Z contrast between Pt multipod core and Pd shell, especially for the bimetallic NCs with thick Pd shell (Fig. 5.4 e, where the brighter region is the Pt core NC, and the darker region is the Pd shell), confirming the existence of Pd shell on Pt NCs.

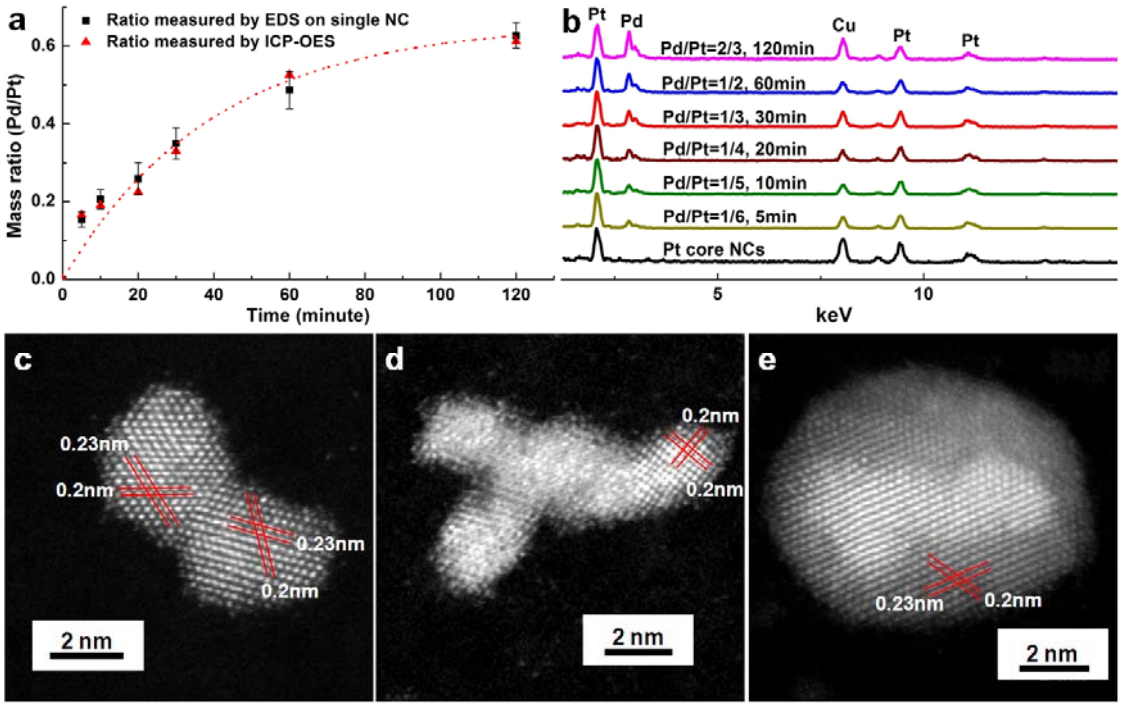

Figure 5.4 Elemental characterization of Pd shell formation using EDS and ICP-OES, and Z-contrast STEM characterization. (a) is the comparison of mass ratios measured with EDS and ICP-OES. The ratios determined by ICP-OES match well with the of EDS results on single NCs. (b) Typical EDS spectra of Pt core and bimetallic Pt-Pd NCs with different Pd wet deposition times. (c-e) representative HAADF-STEM images of (c) Pt multipod core NCs, (d) Pt-Pd NCs with thin Pd shell (30 minutes' deposition time) and (e) Pt-Pd NCs with thick shell (5 hours' deposition time), respectively.

In addition, the EDS line scanning profiles in the Pt/Pd boundary region as shown in insets of Fig. 5.5 b confirmed the existence of Pd compared with the near zero Pd profile in pure Pt core NCs (Fig. 5.5 a). Insets in Fig. 5.5 are line scanning profiles (by EDS) of Pt-L (blue) and Pd-L (red) along the radial direction of the pod. The line scanning profiles were displayed only in the regions close to the edge of the pod or the boundary between Pt and Pd for the purpose of showing how the Pd profile is evolving. The yellow axis indicates the scanning path and distance starting from 0. With thin Pd layer (Fig. 5.5 b), Pd intensity (indicated by the axis in magenta) grows slowly. For thick Pd layer (Fig. 5.5 c), obviously higher intensity of Pd at the shell region can be observed, indicating the existence of Pd shell. HAADF-STEM study confirms the core-shell structure and conformal growth of Pd shell on Pt core. We note that no obvious contrast can be observed in high resolution HAADF images for core-shell NCs with a 1-2 atomic-layer Pd shell (Fig. 5.4 d), and no obvious Pd island formation is observed either, indicating conformal deposition of Pd on Pt core NCs.

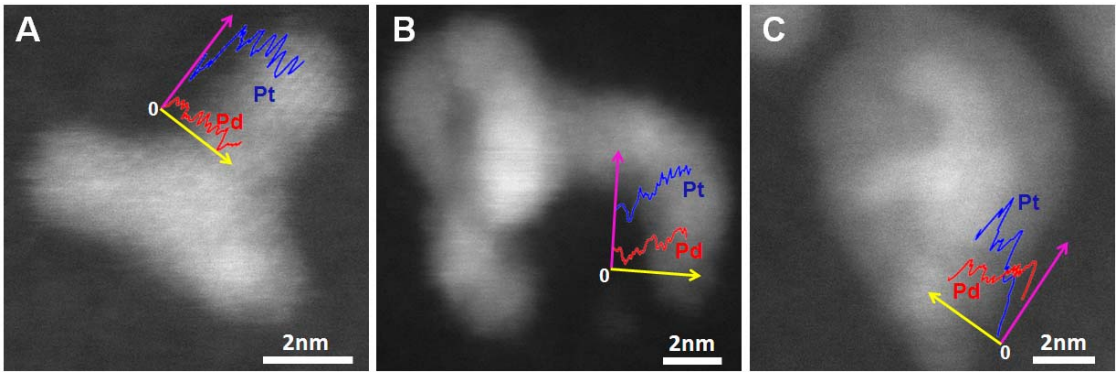

Figure 5.5 HAADF-STEM images of Pt-Pd core-shell NCs. (a) Pt multipod core NCs. (b) and (c) Pt-Pd NCs with Pd grown for 2 and 5 hours, respectively. Insets are EDS line scanning profiles of Pt-L and Pd-L along radial direction of pod. The blue curve is the Pt-

L profile, and the red is Pd-L profile. Yellow axis indicates the scanning path and distance starting from 0, and magenta axis indicates the intensity (element counts).

In addition, EELS mapping was carried out to confirm the core-shell structure. Fig. 5.6 b is the spectrum image with total intensity captured in EELS for the crystal in Fig. 5.6 a. The Pd element map (Fig. 5.6 d) extracted from EELS spectra (Fig. 5.6 c) for all pixels in Fig. 5.6 b shows clear contrast between Pt core (dark region) and Pd (bright region) and indicates the existence of a Pd shell in the bimetallic NCs.

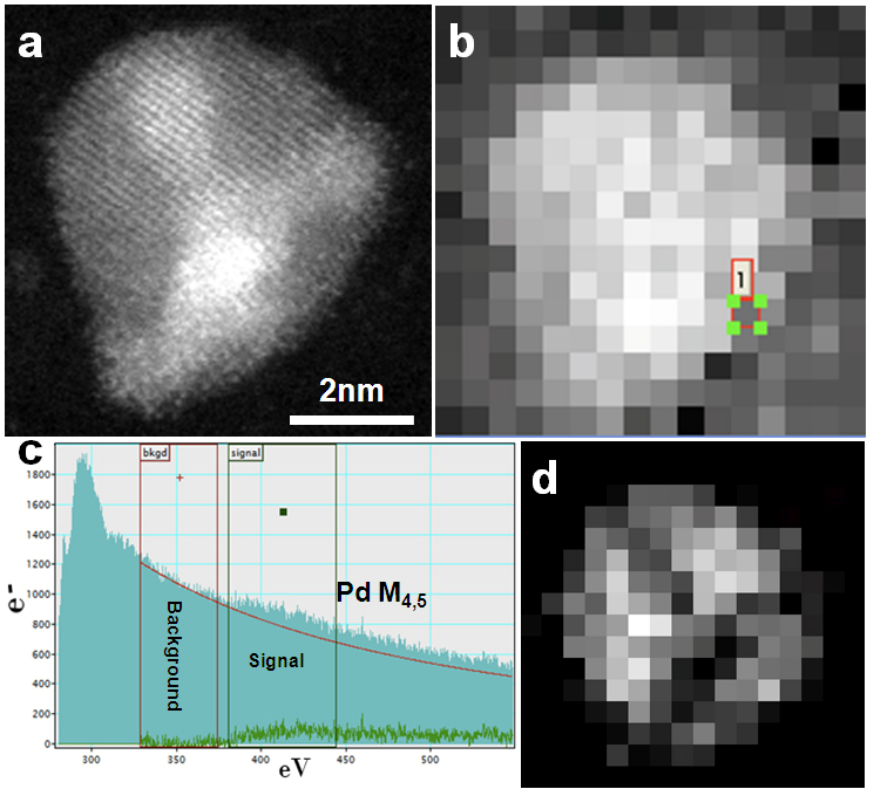

Figure 5.6 EELS study of Pt-Pd core-shell NCs. (a) HAADF STEM image of Pt-Pd NC with thick Pd shell. (b) EELS mapping (total intensity) image of the particle in (a). (c) Extracted EELS spectrum of the highlighted pixel in (b). (d) Extracted Pd map of the particle shown in (a) after background subtraction.

5.3.3 Pd coverage on Pt NC surface

We note that although a Pd shell as thin as 1-2 atomic layers on the Pt core NC is challenging to visualize in the electron microscope due to the inevitable signal limitations, a Pd coverage on the Pt core NCs can be confirmed by the electrochemical approach. Since Pt and Pd individually have distinct hydrogen adsorption behavior in acidic media, it is reasonable to estimate the coverage of Pd on Pt core NC surface using this characteristic.[32] Fig. 5.7 shows the cyclic voltammetric (CV) curves of bimetallic NCs with different Pd/Pt ratios in 0.5 M H_2SO_4. It can be found that the CV curves of Pt-Pd core-shell NCs look similar to Pt/Pd alloy NCs instead of pure Pt or Pd, consistent with the previously reported work.[32] The Pt characteristic hydrogen adsorption peak which occurs around -0.1 V (indicated by the black dashed line, assigned to hydrogen adsorption on Pt(110) facets) gradually diminished from Pt core NCs to Pd/Pt 1/6, showed only a trace bump at 1/3, and totally disappeared when the Pd/Pt reaches 1/2. Meanwhile, another peak at -0.06 V (indicated by the red dashed line) started to be in shape with the increase of Pd ratio.[45] The diminishment of the peak at -0.1 V can be explained by the fewer available Pt atomic sites on the Pt core NC surface with increasing Pd coverage from the wet deposition. For the oxide reduction peak around 0.5 V in the cathodic scan, the peak potential shifts to the negative potential when more Pd is deposited, consistent with the difference between pure Pt and Pd surface oxide reduction potentials as shown in the inset of Fig. 5.7.[45] We therefore suggest that the complete Pd overlay on Pt surface occurs when the Pd/Pt ratio is close to 1/3, and before the Pd/Pt ratio reaches 1/2.

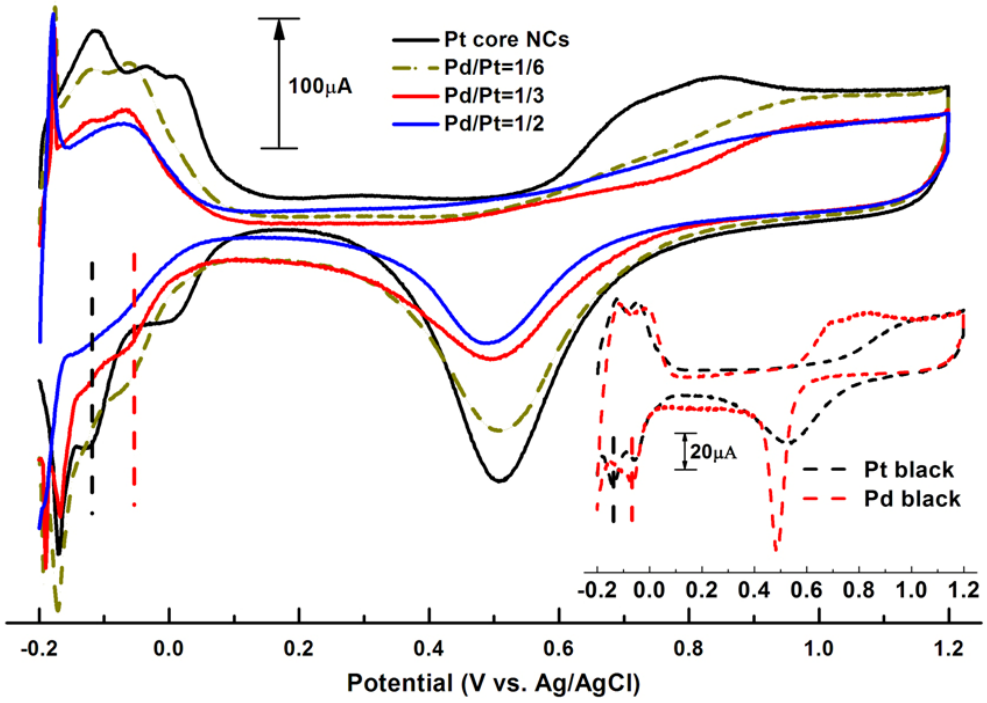

Figure 5.7 Confirmation of Pd monolayer formation by electrochemical approach. CV curves of Pt core NCs and bimetallic NCs with Pd/Pt ratios of 1/6, 1/3, and 1/2, in 0.5 M H_2SO_4 at a scan rate of 50 mV/s. The black dashed line indicates the hydrogen adsorption on Pt(110) facet and the red dashed line indicates the hydrogen adsorption on Pd. Inset shows the CV curves for Pt and Pd black under the same measurement condition.

XPS was employed to examine the surface composition of the core-shell NCs with Pd/Pt ratios of 1/4 and 2/3, respectively. Three deconvoluted peaks are used to fit both the Pt $4f_{5/2}$ and $4f_{7/2}$ peaks as shown in Fig. 5.8. The main contribution comes from the Pt(0), while the lowest contribution comes from the binding energy of the Pt-O bond. The Pt(2+) contribution may from the peptide residues on the surface where Pt atom may coordinate with amines,[41,46] although Pt-Cl bond on the surface might contribute as well due to the precursor ($PtCl_4^{2-}$) residues on the surface.[47] From the characteristic spectra of

the Pd $3d_{3/2}$ and $3d_{5/2}$, three deconvoluted peaks were used to fit the spectra, one coming from the formation of Pd-Pt metallic bond, one from Pd(0) and the other from Pd-O bond.

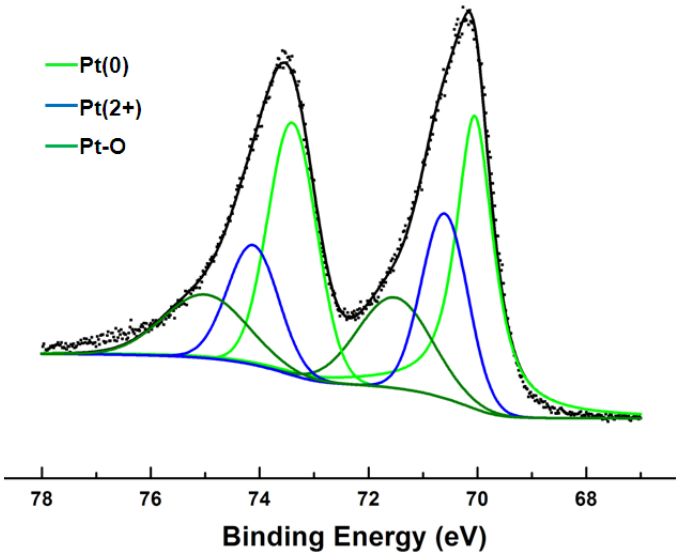

Figure 5.8 XPS of Pt $4f_{5/2}$ and $4f_{7/2}$ for Pt core NCs.

As the Pd/Pt ratio increases from 1/4 to 2/3, we can observe in Fig. 5.9 a and c the decreased contribution from both Pt(2+) and Pt-O and the increased contribution from Pt-Pd bond, indicating Pd atom is replacing the amine residues and O on the surface and being deposited onto Pt. While in Fig. 5.9 b and d, we observed the decreased contribution from Pd-Pt when Pd/Pt ratio increases from 1/4 to 2/3. This observation suggests that the Pd coating on Pt surface is incomplete at Pd/Pt 1/4, where the Pd-Pt bond carries more weight in the surface binding. Then with the completion of the Pd shell (greater than monolayer, when the Pd-Pt bonds reaches its maximum contribution) at Pd/Pt 2/3, Pd-Pd bond starts to populate the surface bonding and hence decrease the relative contribution from the Pd-Pt interface. This observation, together with the increased Pt-Pd contribution in Fig. 5.9 a and c with increasing Pd deposition on Pt surface, confirms that the monolayer Pd shell formation happens between Pd/Pt 1/4 and

2/3. The XPS result also confirms that the surface of the bimetallic NCs is mainly in the oxide state.

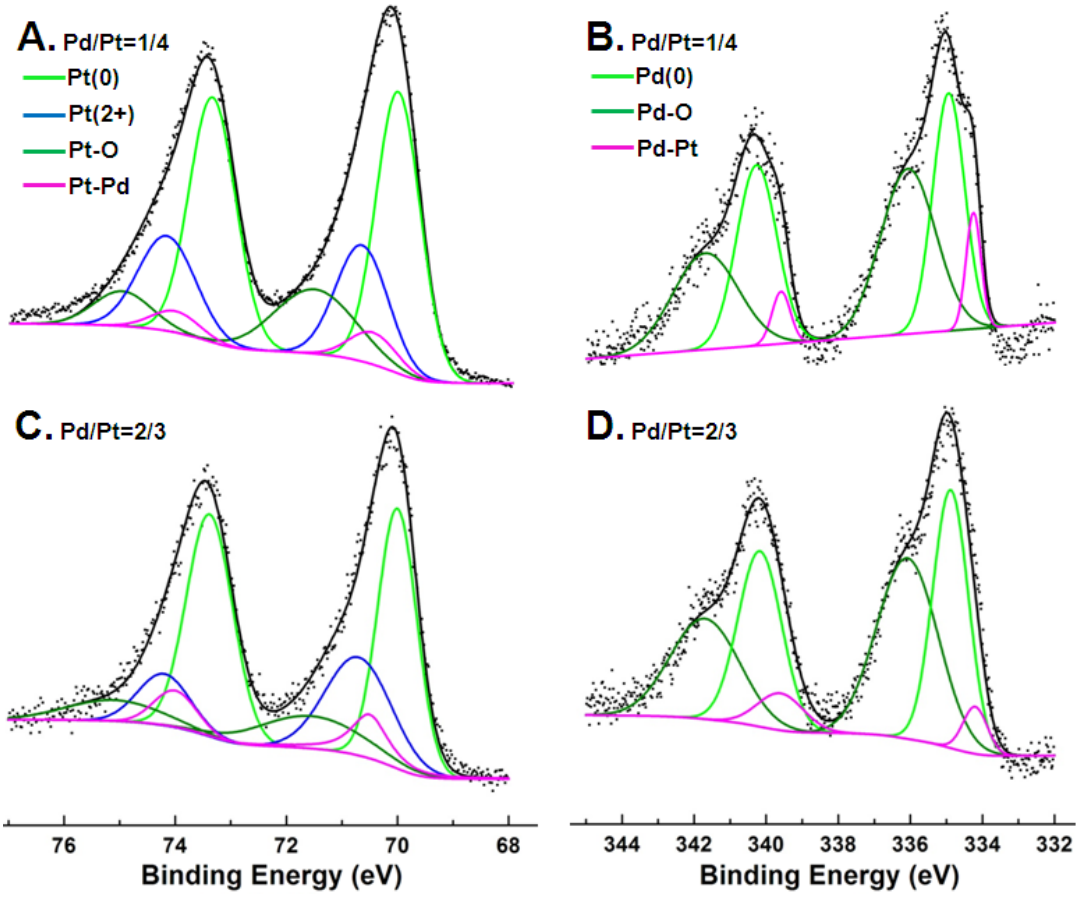

Figure 5.9 Surface elemental characterization of Pd shell with XPS. (a) and (c) are XPS spectra of Pt $4f_{5/2}$ and $4f_{7/2}$ for Pt-Pd NCs with Pd/Pt 1/4 and 2/3. (b) and (d) are XPS spectra of Pd $3d_{3/2}$ and $3d_{5/2}$ for Pt-Pd NCs with Pd/Pt 1/4 and 2/3.

The XPS analysis is consistent with the electrochemical characterization, which indicates the formation of a complete Pd layer on the Pt core NCs happening between Pd/Pt ratio of 1/4 and 2/3.

5.3.4 ORR activities of the Pt-Pd core-shell NCs

Quantitative study of ORR was carried out on a rotating disk electrode (RDE) in 0.1 M KOH. Current densities presented in this study are normalized over the ECSA, which was calculated from the CV curves measured in 0.5 M H_2SO_4 using 210 μC/cm^2 as the electron charge density of the hydrogen monolayer adsorption.

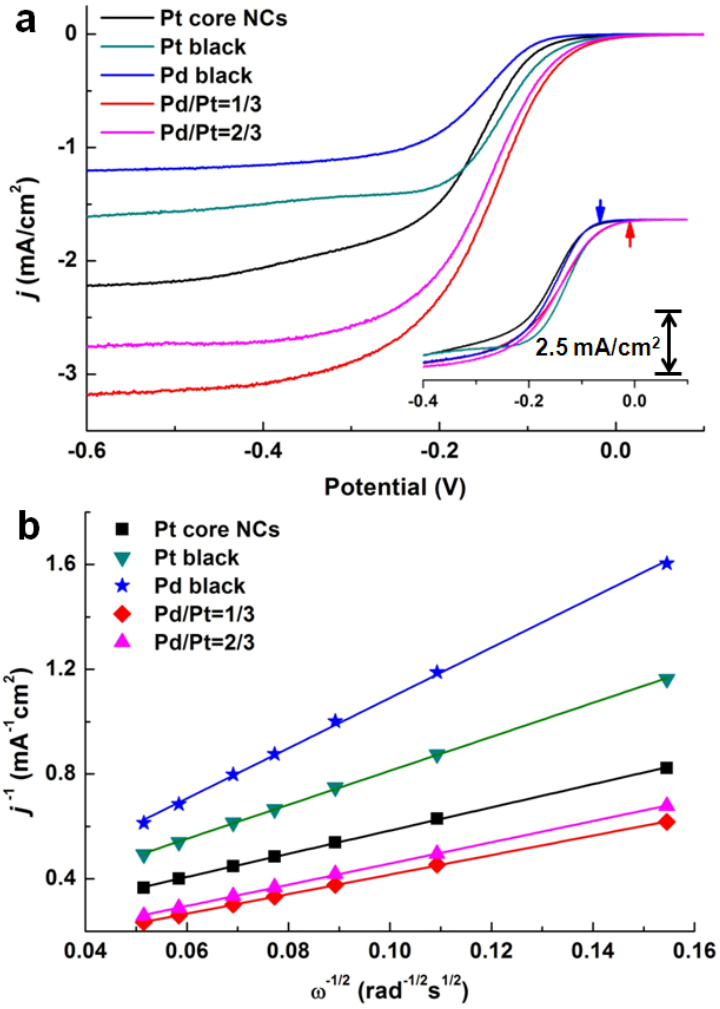

Figure 5.10 ORR kinetic study with RDE technique. (a) Polarization curves (normalized to real surface area ECSA, Potential vs. Ag/AgCl) recorded for Pt core NCs, Pt black, Pd black, and Pt-Pd core-shell bimetallic NCs with Pd/Pt ratios of 1/3 and 2/3 in 0.1 M KOH

at 10 mV/s. Inset is polarization curves between -0.15 and 0.05 V normalized with geometrical area of electrode. (b) L-K plots of the above materials at -0.35 V.

We compared the performance of the bimetallic NCs with Pt core NCs, as well as the commercially available Pt and Pd black to investigate the modification of the catalytic activity induced by the Pd shell. Comparison of the catalytic activities among the different catalysts was made based on the same metal loading amount (1.5 μg) over the 0.196 cm^2 of electrode area. Polarization curves were recorded for the different materials at a rotating speed of 1600 rpm. The polarization curves yield information regarding the O_2 reduction pathway. O_2 can be fully reduced to H_2O through a 4-electron pathway or partially reduced to hydrogen peroxide (H_2O_2) then to H_2O through a 2-electron pathway. In the latter case, a platform is usually observed in the polarization curve. In our case, no platform was found in the ORR region for both the bimetallic NCs and the Pt core NCs, indicating the high yield of the 4-electron pathway (Fig. 5.10 a).

By normalizing the current with the calculated ECSA, (polarization data normalized by geometrical area are shown in the inset of Fig. 5.10 a, demonstrating similar diffusion limiting current for all samples) we can conclude from Fig. 5.10 a that the bimetallic NCs display much higher limiting current densities, with that of the Pd/Pt 1/3 NCs being the highest, than those of the commercial Pt black and Pd black, and obviously higher current density than Pt core NCs. In addition, bimetallic NCs also demonstrated the lowest onset ORR potential when compared to all the other catalysts (Fig. 5.10 a). Previous studies have suggested that a good ORR electrocatalyst should exhibit a moderate interaction with the adsorbate, O, because a too-strong binding might inhibit the dissociation of O from the surface while weak binding might slow down the break-up of O-O bond.[31] In the

Pt-Pd core-shell NCs, we suggest that Pd monolayer on Pt may have a lower binding energy with O than does pure Pt surface, facilitating the subsequent O-O bond break-up and O dissociation steps, leading to the enhanced ORR activities on Pt-Pd core-shell NCs than on Pt core NCs.

More elaborate studies on the kinetics occurring on bimetallic NC surface were carried out to decipher the separate kinetic and diffusion-limited current using Levich-Koutecky (L-K) plots which can be expressed as the following

$$\frac{1}{j} = \frac{1}{j_k} + \frac{1}{j_d} = \frac{1}{j_k} + \frac{1}{B\omega^{1/2}}$$

with $B = 0.62nFC_0D_0^{2/3}\nu^{-1/6}$, and $j_k = nFkC_0$

where j is the measured current density, j_k and j_d are the kinetic and diffusion-limited current densities, respectively, ω is the electrode rotating rate, n is the overall number of electrons transferred in oxygen reduction, F is the Faraday constant, C_0 is the bulk concentration of O_2 saturated in the electrolyte, D_0 is the diffusion coefficient of O_2, ν is the kinematic viscosity of the electrolyte (0.1 M KOH solution), and k is the electron transfer rate constant.[48] The constants C_0, D_0, and ν are selected according to Reference.[49] The intercept of the L-K plot and vertical axis can be used to estimate the kinetic current density.

In our study, series of polarization curves were recorded at different rotating rates ranging from 400 rpm to 3600 rpm, as shown in Fig. 5.11.

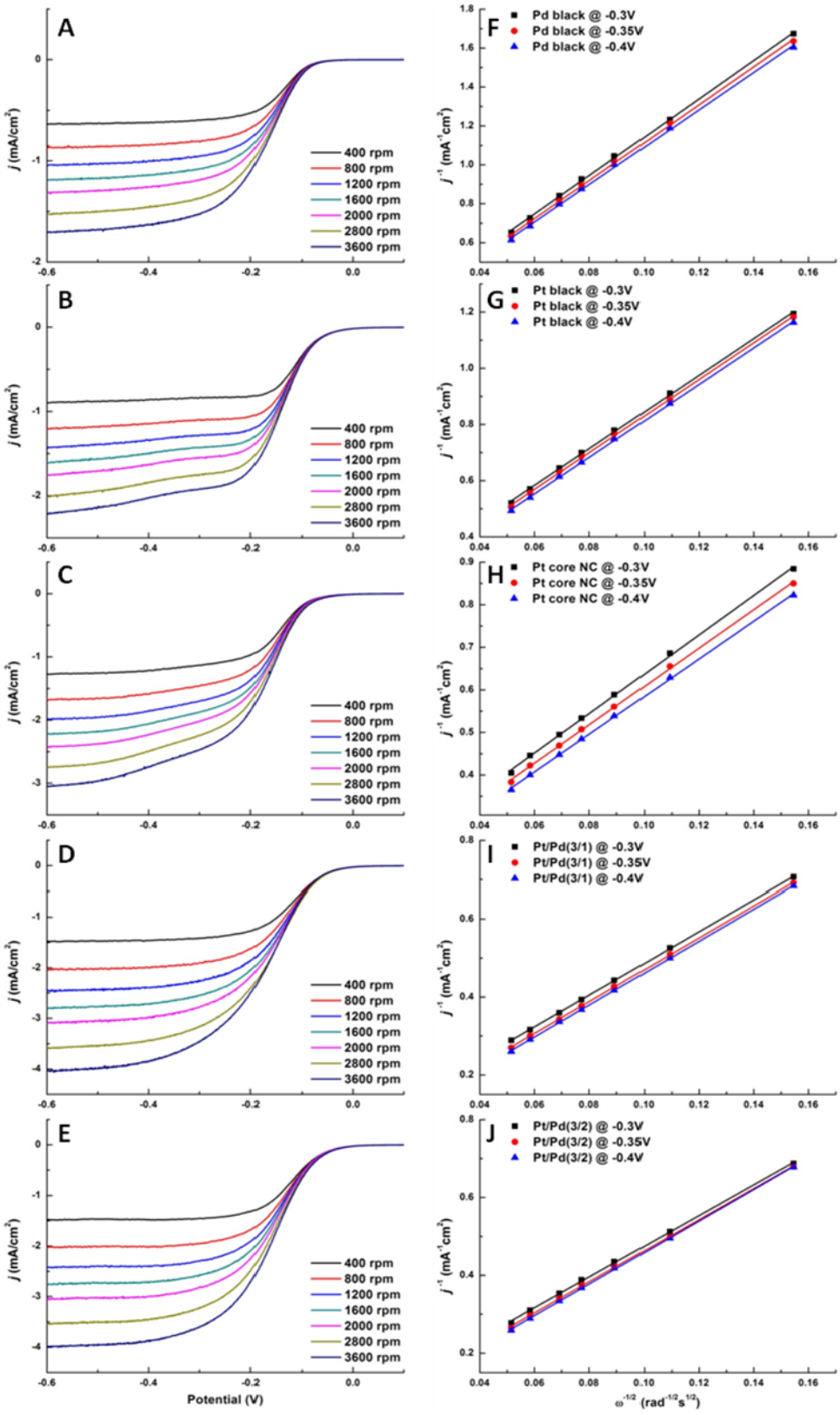
A
B
C
D
E
J (mA/cm²)
400 rpm
800 rpm
1200 rpm
1600 rpm
2000 rpm
2800 rpm
3600 rpm
Potential (V)
F
Pd black @ -0.3V
Pd black @ -0.35V
Pd black @ -0.4V
G
Pt black @ -0.3V
Pt black @ -0.35V
Pt black @ -0.4V
H
Pt core NC @ -0.3V
Pt core NC @ -0.35V
Pt core NC @ -0.4V
I
Pt/Pd(3/1) @ -0.3V
Pt/Pd(3/1) @ -0.35V
Pt/Pd(3/1) @ -0.4V
J
Pt/Pd(3/2) @ -0.3V
Pt/Pd(3/2) @ -0.35V
Pt/Pd(3/2) @ -0.4V
j⁻¹ (mA⁻¹cm²)
ω⁻¹/² (rad⁻¹/²s¹/²)

Figure 5.11 (a-e) are polarization curves of Pd black, Pt black, Pt core NCs, Pt-Pd NCs with Pd/Pt of 1/3 and 2/3 recorded at different rotating speeds. (f-j) are corresponding LK plots at -0.3, -0.35 and -0.4 V for above materials.

The L-K curves were plotted at potentials -0.3, -0.35 and -0.4 V for all NCs (with current normalized with real surface area ECSA). The L-K plots show good linearity and the same slopes over the potential range from -0.3 to -0.4 V for each sample. As a comparison, Fig. 5.10 b shows the L-K plots of bimetallic NCs, Pt core NCs and commercial Pt, Pd black. The L-K plots of bimetallic NCs show smaller slopes than those of the other materials, indicating the enhanced electron transfer efficiency upon introducing Pd shell. Importantly, the kinetic current densities calculated at -0.35 V for the bimetallic NCs with Pd/Pt ratios of 1/3 and 2/3 are 22.79 and 18.77 mA/cm^2, much higher than those of Pt core NCs, Pt and Pd black which are 7.06, 6.13 and 7.65 mA/cm^2, respectively. The values obtained for Pt black is close to the previously reported data.[50] The kinetic current screens the effect of diffusion and thus reflects the nature of the catalytic activity. A 3-fold increase in the kinetic current was observed for the bimetallic NCs when compared with the Pt core NCs, demonstrating the improved catalytic activity of the Pt-Pd core-shell NCs. These quantitative studies demonstrate that the Pd coating on Pt NCs enhances their ORR activities, with highest enhancement achieved with near-monolayer Pd coating, making the bimetallic NCs potentially high-performance cathode catalysts for fuel cell applications in alkaline solutions. Further study is underway to elucidate the detailed mechanism of the enhancement effect of the Pd shell on Pt NCs.

5.3.5 CO poisoning studies of the Pt-Pd core-shell NCs

CO poisoning is a major issue for current application of noble metals as catalyst in fuel cells because the ESCA of the catalyst reduces during operation due to adsorption of CO molecules that are generated from the partial oxidation of methanol molecules and diffuse through the membrane into the cathode. An effective catalyst should be resistant to CO poisoning, so it is important to test the resistance of the catalysts to CO poisoning. Chronoamperometries of Pt core and Pt-Pd core-shell NCs with different Pd/Pt ratios are shown in Fig. 5.12 a. A drop in current was observed with the introduction of CO gas by bubbling. The performance of Pt and Pd black decreased fastest, where i/i_0 dropped to ~0.3 (i and i_0 are currents before and after the introduction of CO, respectively), followed by Pt core NCs. The bimetallic NCs with Pd/Pt 1/3 exhibit a higher stabilized i/i_0 than that of the bimetallic NCs with thicker Pd shell (Pd/Pt=2/3), but both bimetallic NCs hold i/i_0 values (~0.6-0.7) twice those of commercially available Pt black and Pd black.

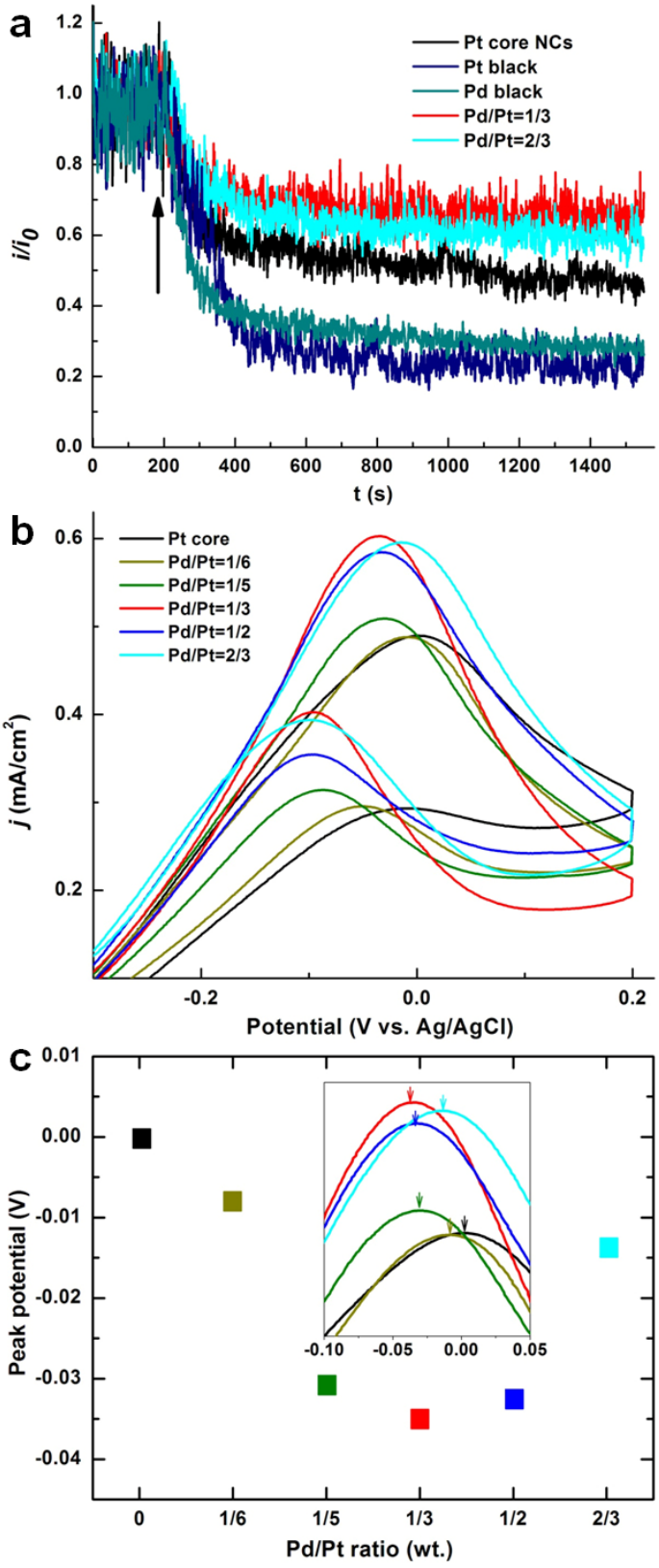
a
Pt core NCs
Pt black
Pd black
Pd/Pt=1/3
Pd/Pt=2/3
i/i0
t (s)
b
Pt core
Pd/Pt=1/6
Pd/Pt=1/5
Pd/Pt=1/3
Pd/Pt=1/2
Pd/Pt=2/3
j (mA/cm2)
Potential (V vs. Ag/AgCl)
c
Peak potential (V)
Pd/Pt ratio (wt.)
0
1/6
1/5
1/3
1/2
2/3

Figure 5.12 CO poisoning tests and methanol oxidation study. (a) CO poisoning study for Pt core, Pt and Pd black, and Pd/Pt 1/3 and 2/3 NCs. Chronoamperometries were recorded at -0.25 V in 0.1 M KOH by introducing CO gas (from 3 min) at the rate of 5 mL/min while keeping the continuous flow of O_2 at 50 mL/min. i_0 is the initial current before introducing the CO. (b) CV curves (shown only between -0.3 and 0.2 V) for Pt core and Pt-Pd NCs with Pd/Pt ratios of 1/6, 1/5, 1/3, 1/2 and 2/3, in 0.1 M KOH and 1 M methanol with a scan rate of 100 mV/s. (c) Plot of methanol oxidation peak potential of the oxidation peak during the forward sweep for different catalysts with Pd/Pt ratios of 0, 1/6, 1/5, 1/3, 1/2 and 2/3. **Inset** shows the zoom-in of CV curves between -0.1 and 0.05 V with peak positions indicated by arrows. (a) and (b) share the same color coding.

The better CO resistivity may be attributed to the fact that the surface of the NCs with thinner Pd shell (close to monolayer) behaves in a similar way to Pt-Pd inter-metallic alloy which is more resistant to CO poisoning.[51] It has been reported that in the Pt-Pd alloy system, stronger electron affinity of Pt causes the shift of electron density from Pd to Pt, which weakens the CO bond with Pd atoms while strengthens the CO bond with Pt atoms. Thus on the alloy surface CO molecules would block Pt-reactive sites but leave Pd sites more accessible for oxygen adsorption and subsequent reaction, resulting in enhanced resistance against CO poisoning.[51,52] Similarly, on the surface of the Pd/Pt 1/3 NCs with Pd monolayer, the electron density shifts toward the Pt underneath the Pd monolayer surface, weakening the bond between CO molecules and the NC surface, decreasing CO absorption on Pd monolayer, which in turn increases its resistance to CO poisoning, while the Pt-Pd core-shell NCs with thicker Pd shell behave more similarly to pure Pd, which is more susceptible to CO poisoning.

5.3.6 Methanol oxidation study of the Pt-Pd core-shell NCs

The catalytic activities of the Pt-Pd core-shell NCs for the electro-oxidation of methanol are studied to assess the performance of the bimetallic NCs as anode catalyst in alkaline media. Catalytic activities of the bimetallic NCs with different Pd/Pt ratios, from 1/6 to 2/3, were compared to see the effect of Pd shell thickness on the catalytic performance. The CV curves were recorded in electrolyte of 0.1 M KOH with 1.0 M methanol. CV curves of the Pt NCs and Pt-Pd core-shell NCs between -0.3 and 0.2 V are shown in Fig. 5.12 b. The currents were normalized with measured ECSA and full CV curves between -1.0 and 0.2 V are shown in Fig. 5.13 a.

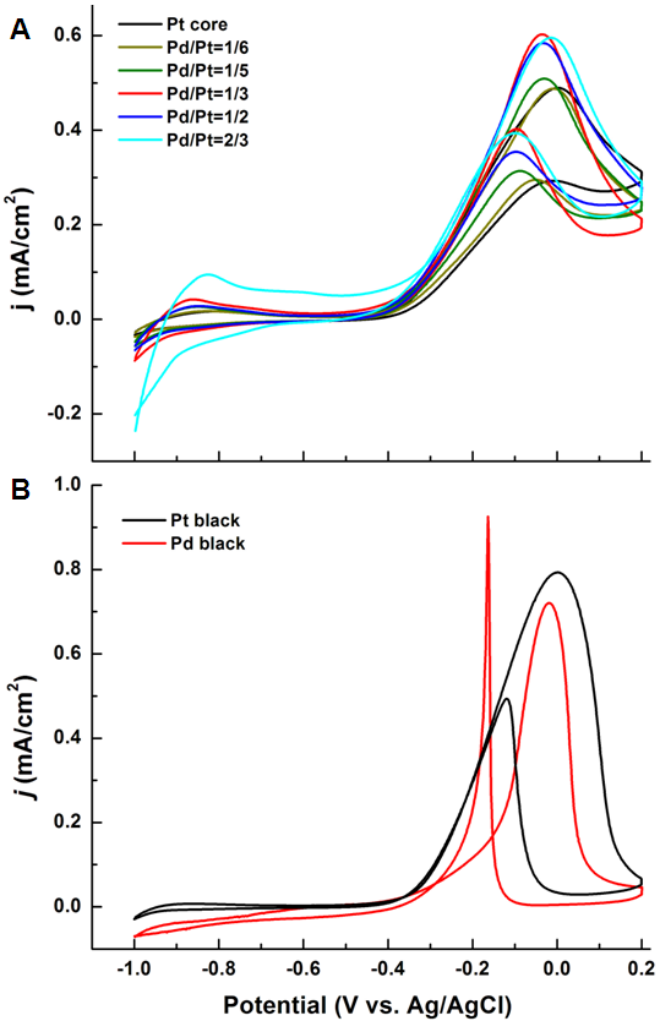

Figure 5.13 Full CV curves for (a) Pt core and Pt-Pd NCs with Pd/Pt ratios of 1/6, 1/5, 1/3, 1/2, 2/3, and (b) Pt black and Pd black The CV curves were recorded in 0.1 M KOH electrolyte with 1 M methanol at the rate of 100 mV/s.

The Pt-Pd core-shell NCs with Pd/Pt ratio 1/3 yields the highest current density for the oxidation peak in the forward sweep, as shown in the zoom-in of CV curves between -0.1 and 0.05 V in the inset of Fig. 5.12 c. In addition, the oxidation peak of methanol during the forward sweep keeps shifting to more negative potential with increasing Pd/Pt ratio from 1/6 to 1/3, and then swifts back towards the positive direction for Pd/Pt ratio of 1/2 and 2/3. The peak potential of commercially available Pt black and Pd black are 0 mV and -20 mV,[53] respectively, both more positive than the 1/3 bimetallic NCs (see supporting information Fig. 5.13 b). The 1/3 bimetallic NCs demonstrate the most negative methanol oxidation peak potential among all bimetallic catalysts (as shown in Fig. 6b), showing close to 35 mV more negative potential than Pt core NCs (and 15 mV more negative than Pd black), which implies that the near monolayer Pd shell yields the lowest energy barrier of the methanol oxidation reaction in alkaline media.

5.4 Conclusion

In conclusion, Pt-Pd core-shell bimetallic NCs with multipod morphologies were synthesized with a two-step protocol in mild aqueous condition, with controllable Pd shell thickness from sub-monolayer to a few atomic layers. The as-synthesized bimetallic NCs demonstrate better performance than the Pt core NCs and commercially available Pt black and Pd black as a cathode catalyst towards ORR, and anode catalyst towards electro-oxidation of methanol fuel molecule in alkaline media. The bimetallic NCs also show better resistance to CO poisoning, which extends the catalyst lifetime. The effect of

the Pd shell on the catalytic activity was systematically studied and the best performance was achieved when the Pd/Pt ratio is 1/3, when the Pd shell is close to one atomic monolayer. These studies demonstrated the potential of using Pt-Pd core-shell bimetallic NCs as high-performance catalysts at both electrodes in DMFC. They also demonstrate the importance of Pd shell thickness of the core-shell NCs on modulating the catalytic performance, which can also provide valuable guidelines for designing high-performance catalysts for fuel cell applications.

[References/Bibliography]

(1) *PEM Fuel Cell Electrocatalysts and Catalyst Layers: Fundamentals and Applications*; Zhang, J., Ed.; Springer London, 2008.

(2) Steele, B. C. H.; Heinzel, A. *Nature* **2001**, *414*, 345.

(3) Mehta, V.; Cooper, J. S. *J. Power Sources* **2003**, *114*, 32.

(4) Lim, B. W.; Lu, X. M.; Jiang, M. J.; Camargo, P. H. C.; Cho, E. C.; Lee, E. P.; Xia, Y. N. *Nano Lett.* **2008**, *8*, 4043.

(5) Teng, X. W.; Liang, X. Y.; Maksimuk, S.; Yang, H. *Small* **2006**, *2*, 249.

(6) Tian, N.; Zhou, Z.-Y.; Sun, S.-G.; Ding, Y.; Wang, Z. L. *Science* **2007**, *316*, 732.

(7) Jiang, L.; Hsu, A.; Chu, D.; Chen, R. *J. Electrochem. Soc.* **2009**, *156*, B643.

(8) Markovic, N. M.; Schmidt, T. J.; Stamenkovic, V.; Ross, P. N. *Fuel Cell* **2001**, *1*, 12.

(9) Dillon, R.; Srinivasan, S.; Arico, A. S.; Antonucci, V. *J. Power Sources* **2004**, *127*, 112.

(10) Hard, G. A. *Platinum Met. Rev.* **1996**, *40*, 10.

(11) Hamnett, A. *Catal. Today* **1997**, *38*, 445.

(12) Stamenkovic, V. R.; Fowler, B.; Mun, B. S.; Wang, G. F.; Ross, P. N.; Lucas, C. A.; Markovic, N. M. *Science* **2007**, *315*, 493.

(13) Kang, Y. J.; Murray, C. B. *J. Am. Chem. Soc.* **2010**, *132*, 7568.

(14) Mayrhofer, K. J. J.; Blizanac, B. B.; Arenz, M.; Stamenkovic, V. R.; Ross, P. N.; Markovic, N. M. *J. Phys. Chem. B* **2005**, *109*, 14433.

(15) Dimos, M. M.; Blanchard, G. J. *J. Phys. Chem. C* **2010**, *114*, 6019.

(16) Park, K. W.; Choi, J. H.; Kwon, B. K.; Lee, S. A.; Sung, Y. E.; Ha, H. Y.; Hong, S. A.; Kim, H.; Wieckowski, A. *J. Phys. Chem. B* **2002**, *106*, 1869.

(17) Liu, H. T.; He, P.; Li, Z. Y.; Li, J. H. *Nanotechnology* **2006**, *17*, 2167.

(18) Wang, J. X.; Markovic, N. M.; Adzic, R. R. *J. Phys. Chem. B* **2004**, *108*, 4127.

(19) Kordesch, K.; Hacker, V.; Gsellmann, J.; Cifrain, M.; Faleschini, G.; Enzinger, P.; Fankhauser, R.; Ortner, M.; Muhr, M.; Aronson, R. R. *J. Power Sources* **2000**, *86*, 162.

(20) Tripkovic, A. V.; Popovic, K. D.; Grgur, B. N.; Blizanac, B.; Ross, P. N.; Markovic, N. M. *Electrochim. Acta* **2002**, *47*, 3707.

(21) Xu, C. W.; Cheng, L. Q.; Shen, P. K.; Liu, Y. L. *Electrochem. Commun.* **2007**, *9*, 997.

(22) Lee, Y. W.; Han, S. B.; Park, K. W. *Electrochem. Commun.* **2009**, *11*, 1968.

(23) Jiang, L.; Hsu, A.; Chu, D.; Chen, R. *J. Electrochem. Soc.* **2009**, *156*, B370.

(24) Li, H. Q.; Sun, G. Q.; Li, N.; Sun, S. G.; Su, D. S.; Xin, Q. *J. Phys. Chem. C* **2007**, *111*, 5605.

(25) Greeley, J.; Mavrikakis, M. *Nat. Mater.* **2004**, *3*, 810.

(26) Habas, S. E.; Lee, H.; Radmilovic, V.; Somorjai, G. A.; Yang, P. *Nat. Mater.* **2007**, *6*, 692.

(27) Peng, Z. M.; Yang, H. *J. Am. Chem. Soc.* **2009**, *131*, 7542.

(28) Lim, B.; Jiang, M. J.; Camargo, P. H. C.; Cho, E. C.; Tao, J.; Lu, X. M.; Zhu, Y. M.; Xia, Y. A. *Science* **2009**, *324*, 1302.

(29) Tao, F.; Grass, M. E.; Zhang, Y. W.; Butcher, D. R.; Renzas, J. R.; Liu, Z.; Chung, J. Y.; Mun, B. S.; Salmeron, M.; Somorjai, G. A. *Science* **2008**, *322*, 932.

(30) Zhang, J. L.; Vukmirovic, M. B.; Sasaki, K.; Nilekar, A. U.; Mavrikakis, M.; Adzic, R. R. *J. Am. Chem. Soc.* **2005**, *127*, 12480.

(31) Zhang, J.; Lima, F. H. B.; Shao, M. H.; Sasaki, K.; Wang, J. X.; Hanson, J.; Adzic, R. R. *J. Phys. Chem. B* **2005**, *109*, 22701.

(32) Wells, P. P.; Crabb, E. M.; King, C. R.; Wiltshire, R.; Billsborrow, B.; Thompsett, D.; Russell, A. E. *PCCP* **2009**, *11*, 5773.

(33) Shao, M. H.; Huang, T.; Liu, P.; Zhang, J.; Sasaki, K.; Vukmirovic, M. B.; Adzic, R. R. *Langmuir* **2006**, *22*, 10409.

(34) Sun, X. M.; Li, Y. D. *Angewandte Chemie-International Edition* **2004**, *43*, 597.

(35) Sun, Z.; Yang, Z.; Zhou, J.; Yeung, M. H.; Ni, W.; Wu, H.; Wang, J. *Angewandte Chemie-International Edition* **2009**, *48*, 2881.

(36) Huang, X.; Zhang, H.; Guo, C.; Zhou, Z.; Zheng, N. *Angewandte Chemie-International Edition* **2009**, *48*, 4808.

(37) Kristian, N.; Wang, X. *Electrochem. Commun.* **2008**, *10*, 12.

(38) Lima, F. H. B.; Zhang, J.; Shao, M. H.; Sasaki, K.; Vukmirovic, M. B.; Ticianelli, E. A.; Adzic, R. R. *J. Solid State Electrochem.* **2008**, *12*, 399.

(39) Arenz, M.; Schmidt, T. J.; Wandelt, K.; Ross, P. N.; Markovic, N. M. *J. Phys. Chem. B* **2003**, *107*, 9813.

(40) Arenz, M.; Stamenkovic, V.; Ross, P. N.; Markovic, N. M. *Surf. Sci.* **2004**, *573*, 57.

(41) Li, Y.; Huang, Y. *Adv. Mater.* **2010**, *22*, 1921.

(42) Li, Y.; Whyburn, G. P.; Huang, Y. *J. Am. Chem. Soc.* **2009**, *131*, 15998.

(43) Chiu, C.-Y.; Li, Y.; Ruan, L.; Ye, X.; Murray, C. B.; Huang, Y. *Nature Chemistry* **2011**, *3*, 393.

(44) Ruan, L.; Chiu, C.-Y.; Li, Y.; Huang, Y. *Nano Lett.* **2011**, *11*, 3040.

(45) Capon, A.; Parsons, R. *J. Electroanal. Chem.* **1972**, *39*, 275.

(46) Kumar, A.; Joshi, H. M.; Mandale, A. B.; Srivastava, R.; Adyanthaya, S. D.; Pasricha, R.; Sastry, M. *J. Chem. Sci.* **2004**, *116*, 293.

(47) Karhu, H.; Kalantar, A.; Vayrynen, I. J.; Salmi, T.; Murzin, D. Y. *Applied Catalysis a-General* **2003**, *247*, 283.

(48) Bard, A. J.; Faulkner, L. R. *Electrochemical Methods: Fundamentals and Applications*; Wiley: New York, 2001.

(49) Chen, W.; Chen, S. *Angewandte Chemie-International Edition* **2009**, *48*, 4386.

(50) Meng, H.; Shen, P. K. *Electrochem. Commun.* **2006**, *8*, 588.

(51) Papageorgopoulos, D. C.; Keijzer, M.; Veldhuis, J. B. J.; de Bruijn, F. A. *J. Electrochem. Soc.* **2002**, *149*, A1400.

(52) Matsumoto, F.; Roychowdhury, C.; DiSalvo, F. J.; Abruna, H. D. *J. Electrochem. Soc.* **2008**, *155*, B148.

(53) Kadirgan, F.; Beden, B.; Leger, J. M.; Lamy, C. *J. Electroanal. Chem.* **1981**, *125*, 89.

Chapter 6

6 LOW-TEMPERATURE SEED-MEDIATED SYNTHESIS OF MONODISPERSED HYPERBRANCHED PLATINUM-RUTHENIUM NANOPARTICLES AND THEIR ELECTROCATALYTIC ACTIVITY IN METHANOL OXIDATION

6.1 Introduction

Noble-metal-based multi-component nanoparticles (NPs) are attracting both academic and industrial interests as anode electrocatalysts for methanol electro-oxidation, etc.[1-7] Due to the low adsorption potential of active oxygen atoms on Ru, bimetallic PtRu NP has shown low energy barrier for methanol oxidation as well as CO oxidation, which enhanced their catalytic activity and CO tolerance.[8-12] This enhancement, based on the commonly accepted bi-functional mechanism, depends strongly on the distribution of Pt and Ru atoms on NP surface. The methanol molecules that mostly adsorbed on Pt, and the oxygen atoms, adsorbed mainly on Ru, need to be adjacent to each other to render the occurrence of the methanol oxidation reaction more efficient.[13,14] Different synthetic approaches including H_2 reduction, polyol reduction, impregnation, microwave, γ irradiation, and sonochemical reduction, have been developed to obtain PtRu NPs with different sizes and compositions.[15-24] NPs synthesized by these approaches are spherical or near spherical without any particular shapes. Besides, bimetallic core-shell, hollow NPs, and three dimensional structures have also been synthesized containing Pt and Ru.[25-29] Herein, we report a new approach to synthesize PtRu NPs with hyperbranched (HB) morphology by a Pt seed-mediated growth mechanism at room temperature. We found

that HB morphology leads to an increase in the methanol oxidation activity by creating more adjacent sites for Pt and Ru.

6.2 Experimental

6.2.1 Preparation of hyperbranched PtRu NPs

Potassium tetrachloroplatinate (K_2PtCl_4, Aldrich, >99.9%) was dissolved in ultraclean de-ionized (DI) water (Aqua, 18.2 MΩ) to prepare K_2PtCl_4 stock solution of 10 mM and aged for at least 48 h before being used. Ruthenium(III) chloride hydrate ($RuCl_3 \cdot xH_2O$, Aldrich, 99.98%) was dissolved in water to prepare $RuCl_3$ stock solution of different concentrations such as 10, 20 mM. Peptide molecules (with sequence Ser-Ser-Phe-Pro-Gln-Pro-Asn, termed as S7) were used as capping agent for the synthesis. S7 stock solution was prepared by dissolving 1 mg of S7 peptide in 1 mL of water. Reaction solution were prepared by mixing 200 μL of K_2PtCl_4 stock solution, 100 μL of peptide stock solution, and 2.8 mL of DI water and kept stirred for 5 min before reaction. Fresh 40 mM sodium borohydride ($NaBH_4$) solution was prepared immediately before reaction by dissolving 15 mg $NaBH_4$ (Aldrich, 99.99%) in 10 mL DI water.

Reaction was carried out by injecting 100 μL $NaBH_4$ solution in a single shot into the reaction vessel containing K_2PtCl_4 and S7 peptide. After 30 s, 800 μL $RuCl_3$ stock solution was injected in another shot into the reaction solution. The reaction solution was centrifuged after 1 h of reaction and the precipitated NPs were collected and re-dispersed in 1 mL DI water.

TEM samples were prepared by floating the carbon side of the copper grid on a drop of NP solution for 5 min and then on a drop of DI water for another 3 min. The grid was dried in air at room temperature. TEM images were obtained on FEI CM 120 operated at

120 kV. HRTEM images, HAADF images, and EDS were captured on FEI TITAN STEM operated at 300 kV.

UV-Vis spectra were obtained from DU®800 Spectrophotometer. XRD pattern were obtained from panalytical X'pert pro diffractometer. Weight concentration of the NP solution was determined by inductively coupled plasma optical emission spectrometry (ICP-OES).

6.2.2 Electrochemical measurement

NP solutions were diluted to 0.5 mg/mL based on the concentrations measured by ICP-OES. Working electrodes were prepared by pipetting 8μL of NP solution onto a glassy carbon electrode with a diameter of 3mm and dried at 60 ^{o}C. A Nafion solution of 0.05% was then pipetted to the electrode and dried to cover the NP layer. Commercially available PtRu black (1:1 in atomic ratio, Alfa Aesar) and Pt black (Alfa Aesar) were used as comparison.

Electrochemical surface areas were determined by UPD Cu stripping approach. Ag/AgCl electrode and Pt wire were used as reference electrode and counter electrode, respectively. All potentials mentioned are recorded vs. Ag/AgCl reference electrode. In 0.1 M H_2SO_4 electrolyte, the electrode was kept at 0.8V for 120 s, and then 0.1 V for 150 s, and followed with linear scan from 0.1 to 0.8 V at the rate of 10 mV/s. The same electrochemical treatment was done in the electrolyte with 0.1 M H_2SO_4 and 0.005 M $CuSO_4$. The charge induced by Cu desorption was calculated by subtracting the currents of the two curves and integrating the current with respect to time. Area was calculated by dividing the charge by monolayer stripping charge of Cu, 420 μC/cm^2.

Cyclic voltammograms (CVs) were recorded in 0.1 M H_2SO_4 electrolyte with 0.5 M methanol at a scan rate of 100 mV/s between -0.2 and 1 V. The obtained CV curves were normalized by the area determined by Cu UPD approach.

6.3 Results and discussions

6.3.1 Synthesis of PtRu NPs

A mixed aqueous solution of potassium tetrachloroplatinate (K_2PtCl_4) and a peptide molecule with sequence (Ser-Ser-Phe-Pro-Gln-Pro-Asn, termed as S7) was prepared and stirred for 5 min before reaction. The S7 peptide has been demonstrated to generate ultrasmall Pt seeds.[30-32] A fresh 40 mM sodium borohydride ($NaBH_4$) solution was injected in a single shot to generate the Pt seeds, followed by another injection of 10 mM ruthenium chloride ($RuCl_3$) solution after 30 s. The color turned into light golden gradually after the $NaBH_4$ injection, and finally rapidly into black in 5 s after $RuCl_3$ injection. The NPs synthesized with different $RuCl_3$ concentrations are shown in Fig. 6.1 (a-c). As-synthesized NPs with this seed-mediated approach show the HB morphology. With increasing amount of $RuCl_3$ injected, the NPs do not change much in sizes but show improvement in size distribution. High resolution transmission electron microscopy (HRTEM) (Fig. 6.1 d) revealed that most of the 'branches' are attached together by (111) twinning planes rather than the physical aggregation. The NP surface is found to display both low and high index facets. According to the fast Fourier transform (FFT) of the HRTEM image shown in Fig. 6.1 d, (311) facets exist as part of the exposed surfaces on the branches, which can possibly endow the NPs with higher catalytic activity due to more step and corner atoms exposed at the high-index facet. This is in contrast to the

surface of PtRu black as shown in Fig. 6.2 where the mostly observed facets are (111) facets.

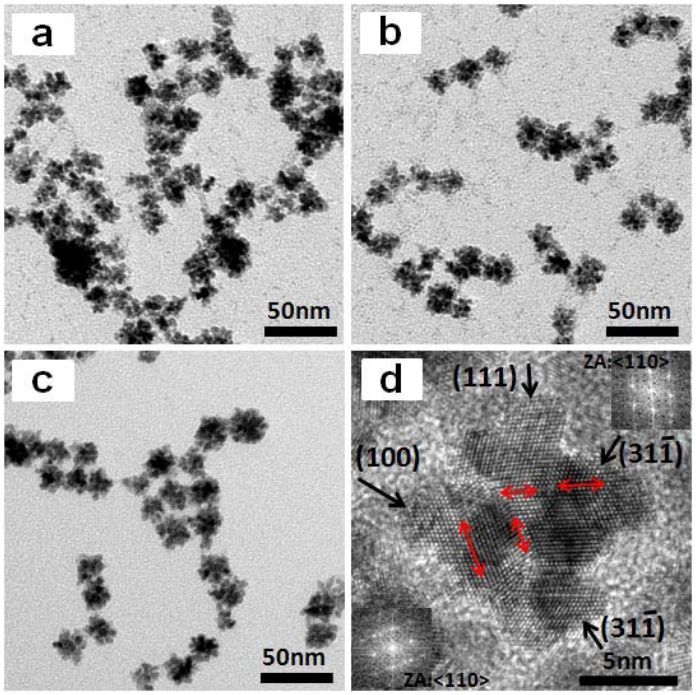

Figure 6.1 TEM images of PtRu HBNPs with different Pt/Ru precursor ratios: (a) 1/1, (b) 1/2 and (c) 1/4. (d) HRTEM image of typical as-synthesized PtRu HBNP.

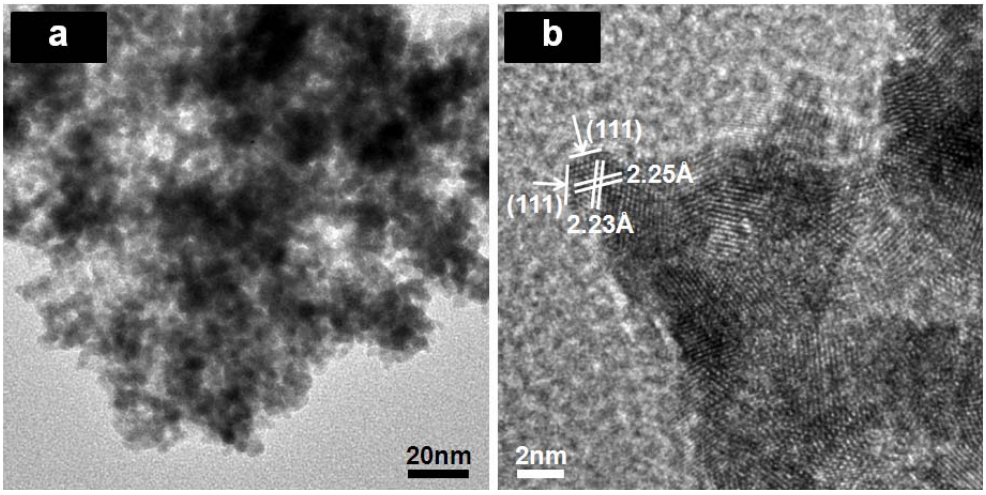

Figure 6.2 (a) Low magnification TEM image and, (b) HRTEM image of PtRu black, respectively.

Powder X-ray diffraction (PXRD) was carried out for as-synthesized Pt_3Ru HBNPs, and compared with Pt black and PtRu black (50% Ru in atomic%), as shown in Fig. 6.3. The XRD pattern of the alloy NPs can be indexed to (111), (200), (220), and (311) diffractions of a face-centered-cubic (FCC) crystal structure. The well-shaped (111) diffraction peaks confirm high alloying degree in the NPs. And the (111) peak of Pt_3Ru HBNPs is located between those of Pt black and PtRu black consistent with the composition-lattice trend. The lattice constant was calculated to be 3.887 nm. The crystalline domain size was measured to be 6.9 nm using Debye-Scherrer formulation and the full width at half-maximum (FWHM) of the (111) diffraction peak.[33] This is consistent with the HRTEM observation in that the single crystalline domain of each branch is between 5-8 nm.

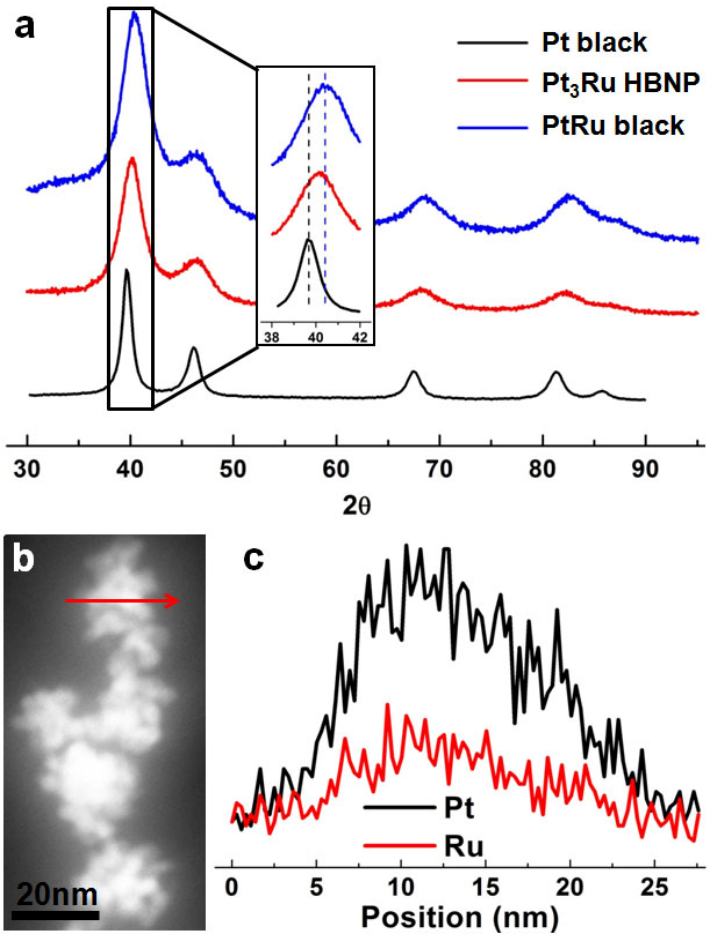

Figure 6.3 (a) XRD patterns of Pt black, Pt_3Ru and PtRu black. (b) HAADF-STEM images of Pt_4Ru HBNPs. (c) EDS line scanning profile of one PtRu HBNP as highlighted in (b).

Element distribution on single NP was carried out by energy-dispersive X-ray spectroscopy (EDS). Fig. 6.3 b shows scanning transmission electron microscopy high angle annular dark field (STEM-HAADF) image of the Pt_4Ru HBNPs. The line scanning profile of EDS spectra is captured on a single NP and shown in Fig. 6.3 c. Due to the hyperbranched nature of the NPs, the profiles are bumpy, but shows no abrupt phase change through the NPs.

6.3.2 Mechanism study

Pt seeds were captured by taking reaction solution 30 s after the $NaBH_4$ injection and casting onto the TEM grids followed by wash with DI water, as shown in Fig. 6.4.

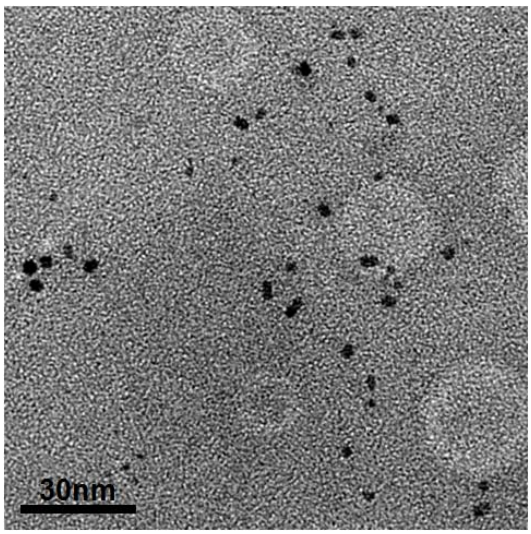

Figure 6.4 TEM images of the Pt NPs captured at 30 s and after injecting 1 mM $NaBH_4$ into the mixed solution of 0.5 mM K_2PtCl_4 and 25 μg/mL S7.

Compared with the size (~15 nm) of the HBNPs, the Pt seeds formed before $NaBH_4$ injection (~1-2 nm, see Fig. S2 in SI) is difficult to be distinguished from the profile. The EDS line scanning results indicate that the Pt and Ru atoms are uniformly distributed in the NPs. Both XRD and EDS data confirm that the seed-mediated synthesis approach can produce well-alloyed PtRu NPs at room temperature.

The role of the Pt seeds in the formation of HBNPs was also studied. The injection of $NaBH_4$ solution introduced a large amount of ultrasmall Pt seeds as shown in Fig. 6.4 that play an important role in the nucleation of PtRu NPs. Without the Pt seeds, irregular PtRu NPs form instead of the HBNPs. For the PtRu NPs shown in Fig. 6.5, an aqueous solution of 3.1 mL with 25 μg/mL S7 (final concentration) was prepared and stirred for 5

min. Then, 400 μL of 5 mM K_2PtCl_4, and 400 μL of 5 mM $RuCl_3$ solutions were injected simultaneously 30 s after the injection of 100 μL of 40 mM $NaBH_4$.

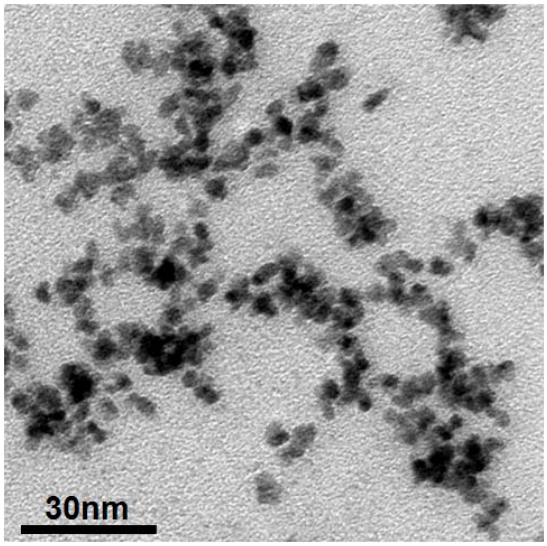

Figure 6.5 PtRu NPs synthesized by injecting 0.5 mM K_2PtCl_4 and 0.5 mM $RuCl_3$ into solution with 1 mM $NaBH_4$ and 25 μg/mL S7.

As another control experiment, when only $RuCl_3$ is reduced with the presence of S7 peptide, a network of irregular Ru NPs form instead of well-defined crystalline NPs, as shown in Fig. 6.6. For the synthesis, a solution of 3.5 mL with 25 μg/mL S7 was prepared and stirred for 5 min. Then, only 400 μL of 5 mM $RuCl_3$ solution was injected 30 s following the injection of 100 μL of 40 mM $NaBH_4$.

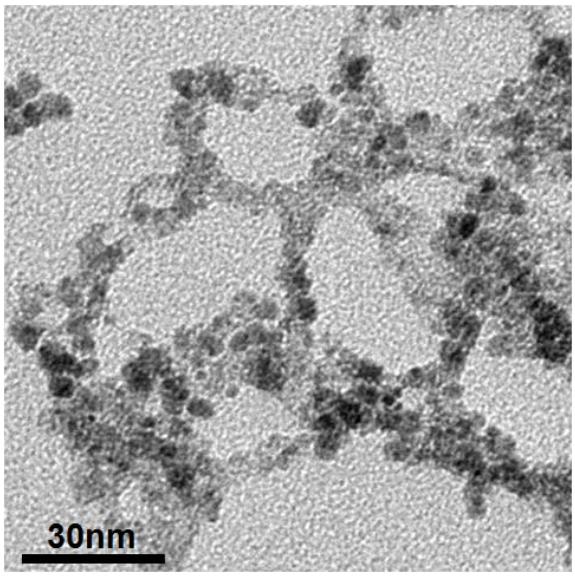

Figure 6.6 Ru NPs synthesized by injecting 0.5 mM $RuCl_3$ into solution with 1 mM $NaBH_4$ and 25 μg/mL S7.

It was also observed that without $RuCl_3$, smaller Pt NPs can form with low product yield. For the synthesis, 40 mM $NaBH_4$ (100 μL) solution was injected into solution containing 1 mM K_2PtCl_4 and 25 ug/mL S7 peptide molecule. Pt NPs were captured by taking reaction solution 1 h after the $NaBH_4$ injection and casting onto the TEM grids followed by washing with DI water, as shown in Fig. 6.7.

However, with the addition of $RuCl_3$, significant amount of Pt atoms can be reduced and seeds serving as heterogeneous nucleation sites, the presence of $RuCl_3$ could accelerate the reduction rate of $PtCl_4^{2-}$ to eventually form PtRu HBNPs. This can be attributed to the autocatalytic process of the Pt seeds for the co-reduction of Pt and Ru.[34]

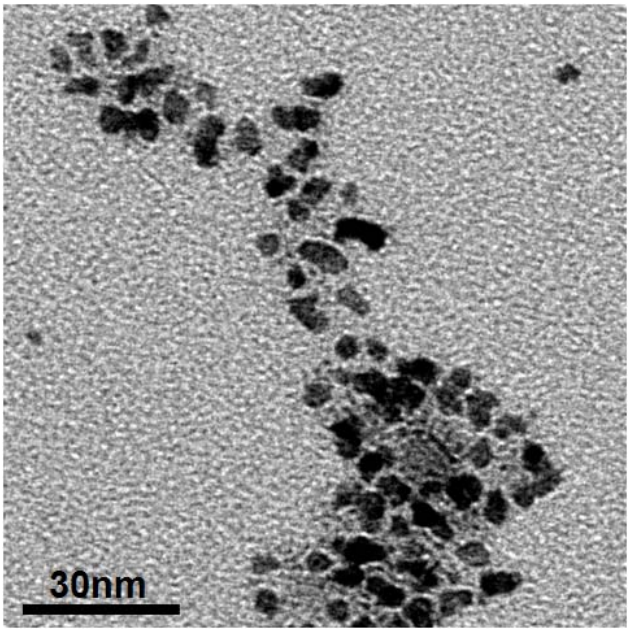

Figure 6.7 TEM images of the Pt NPs 1 h after injecting 1 mM $NaBH_4$ into the mixed solution of 0.5 mM K_2PtCl_4 and 25 μg/mL S7.

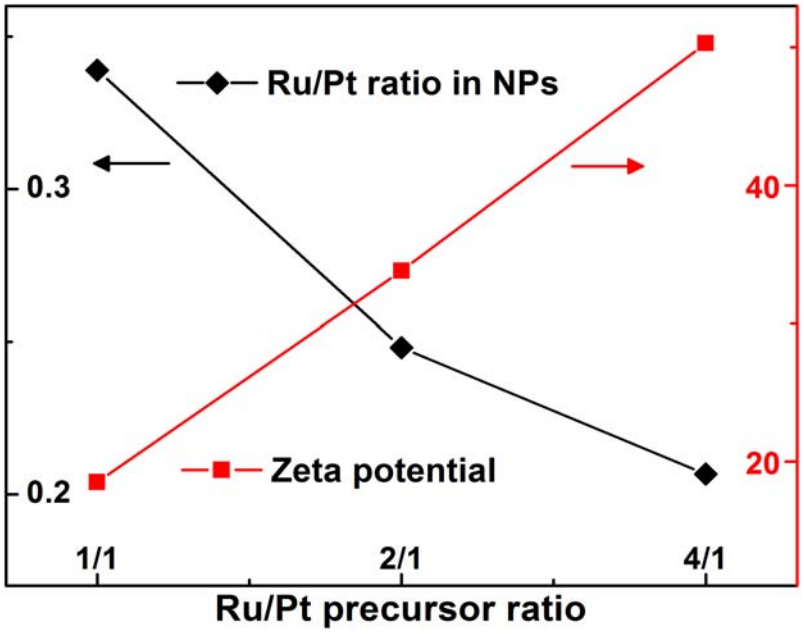

Figure 6.8 Diagram showing relationships of Ru/Pt ratios in HBNPs, as well as the zeta potential of the NPs, with the starting Ru/Pt precursor ratios.

Atomic ratios measured by EDS in Fig. 6.8 show that fewer Ru atoms are incorporated into the HBNPs (lower Ru/Pt) when higher $RuCl_3$ concentration is used, so further experiments were carried out to understand the formation mechansim of HBNPs. The standard reduction potential of Ru^{3+} to Ru is 0.68 V, but it is only 0.24 V for Ru^{3+}/Ru^{2+} pair and 0.45 V for Ru^{2+}/Ru^{0} pair. It indicates that Ru^{3+} may be reduced to Ru^{2+} and then to Ru^{0}, rather than the scenario in which Ru^{3+} is reduced directly to Ru^{0}, as shown in Fig. 6.9.

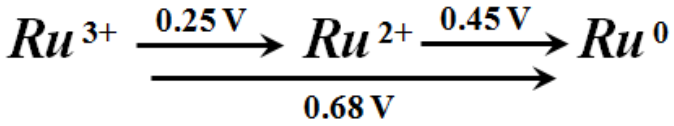

Figure 6.9 Standard reduction potentials Ru^{3+} to Ru^{2+}, Ru^{2+} to Ru^{0}, and Ru^{3+} directly to Ru^{0}, during its reduction pathway.

It has been reported that Ru^{2+} species visually show a ink-blue color and show absorption in UV region between 200 and 300 nm.[35] So images were taken with video mode to capture the colour of Ru^{3+}. 100 µL of fresh $NaBH_4$ solution was firstly injected into reaction solution containing 1 mM K_2PtCl_4 and 25 µg/mL S7 peptide. And then 800 µL of 5 mM $RuCl_3$ solution was injected into the solution. Fig. 6.10 shows the snapshots taken from video, which is at 0.1 s from the start of $RuCl_3$ injection. All images show original color without any color processing. From the snapshots of the color evolution of the reaction, it can be observed that in about 2 s after the $RuCl_3$ injection, the solution displays the ink blue color, which quickly turns dark due to the formation of NPs.

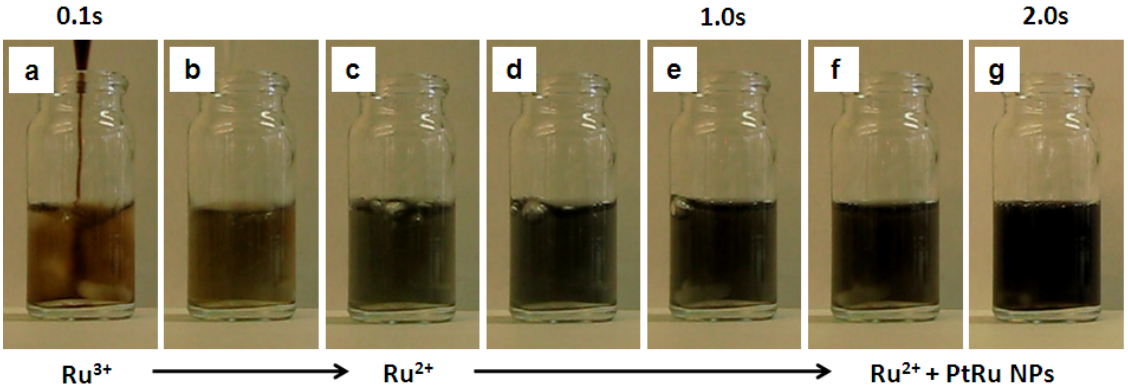

Figure 6.10 (a-g) Snapshots of video recorded showing the color change of reaction solution in 2 s after the $RuCl_3$ injection.

To further confirm the existence of Ru^{2+} in the solution under the reducing conditions, UV-Vis spectra were captured for the supernatants of reaction solutions obtained by injecting different concentrations of $RuCl_3$ into $NaBH_4$ solutions (Fig. 6.11). K_2PtCl_4 was not included as $PtCl_4^{2-}$ has overlapping absorption region with Ru^{2+}. At low $RuCl_3$ concentrations, no Ru^{3+} or Ru^{2+} signature were observed since all Ru ions were reduced. However, at higher $RuCl_3$ concentrations, supernatants start to show a shouder peak at 210 nm as indicated by the arrow, which is assigned to the absorption of Ru^{2+} (Fig. 6.11).[36] The observations suggest that when lower concentration of $RuCl_3$ was used for HBNP synthesis, $NaBH_4$ can reduce all Ru^{3+} to Ru^{2+} and then to Ru^0. However, when higher $RuCl_3$ concentration was used, more $NaBH_4$ was consumed to reduce Ru^{3+} to Ru^{2+}. Hence a significant portion of the Ru^{2+} can not be further reduced to Ru^0 due to the exhausion of the $NaBH_4$, and remained as Ru^{2+} in the solution. This explains the fact that when higher $RuCl_3$ concentration is injected, less Ru is incorporated into the obtained HBNPs. Through this approach, the ratio of Pt/Ru can be manipulated from 3 to 5, while maintaining the HB morphology.

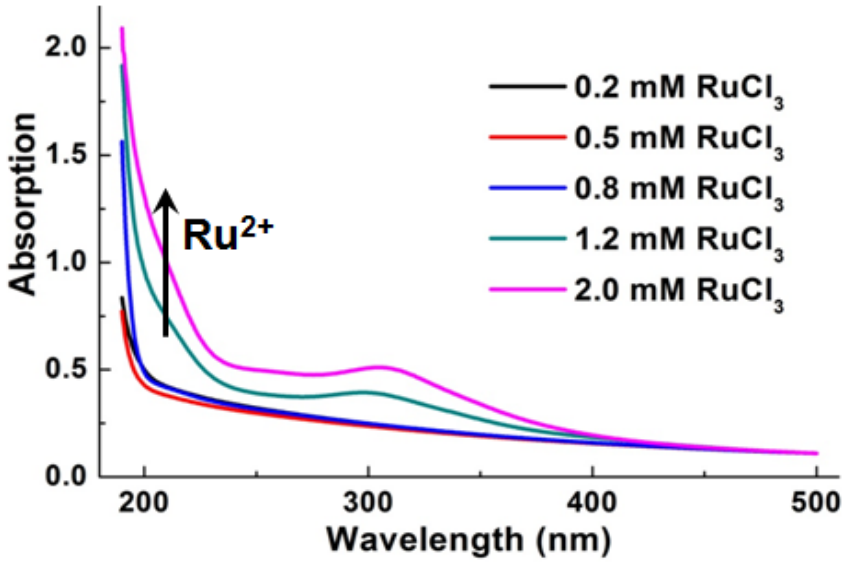

Figure 6.11 UV-Vis specta of supernatents from centrifuged reaction solutions when injecting $RuCl_3$ of different concentrations into 2 mM $NaBH_4$ solution.

6.3.3 Electro-catalytic activities of PtRu HBNPs

Electro-oxidation of methanol was conducted to evaluate the electro-catalytic performance of PtRu HBNPs. Commercial Pt and PtRu black were used as comparisons. Electrochemical surface areas were determined by under-potential deposited (UPD) Cu stripping approach, as shown in Table 6.1.[37] For the experimental details, in 0.1 M H_2SO_4 electrolyte, the electrode was kept at 0.8V for 120 s, and then 0.1 V for 150 s, and followed with linear scan from 0.1 to 0.8 V at the rate of 10 mV/s. The same electrochemical treatment was done in the electrolyte with 0.1 M H_2SO_4 and 0.005 M $CuSO_4$. The charge induced by Cu desorption was calculated by subtracting the currents of the two curves and integrating the current with respect to time. Area was calculated by dividing the charge by monolayer stripping charge of Cu, 420 $\mu C/cm^2$.

Table 6.1 Electrochemical surface areas (measured by Cu UPD method) of different catalysts used in this study.

Catalyst	ECSA (m^2/g)
Pt black	18.2
PtRu black	36.6
Pt_3Ru HBNP	57.9
Pt_4Ru HBNP	65.4
IR $Pt_{1.2}Ru$	77.4
IR $Pt_{1.8}Ru$	75.0

Cyclic voltammograms (CVs) were recorded in 0.1 M H_2SO_4 electrolyte with 0.5 M methanol. Currents were normalized with surface areas determined by UPD Cu stripping as shown in Fig. 6.12.

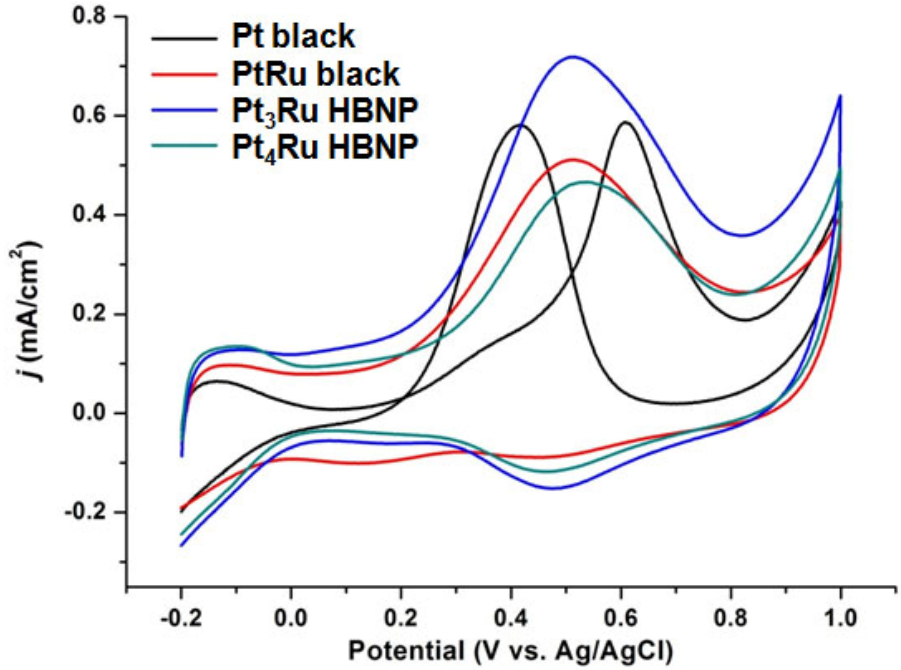

Figure 6.12 CV curves of Pt black, PtRu black and Pt_3Ru and Pt_4Ru HBNPs in 0.1 M H_2SO_4 + 0.5 M methanol.

For Pt black, there is an enormous oxidation peak at 0.4 V (vs. Ag/AgCl reference electrode otherwise specially noted) in cathodic scan which is commonly assigned to the oxidation of partially oxidized species that adsorbs on Pt surface after the anodic scan. This peak totally disappeared for PtRu HBNPs with different Pt/Ru ratios, indicating that methanol can be fully oxidized during the anodic scan. In addition, the oxidation peak in anodic scan of PtRu is about 0.1 V more negative than that of Pt. It can be explained by the bi-functional mechanism. On pure Pt, oxygen species starts to adsorb on the surface between 0.3 and 0.4 V, and methanol starts to adsorb at around 0 V, so the oxygen adsorption is the rate-limiting step for oxidation of methanol on Pt surface. However, on Ru surface, oxygen species start to adsorb from 0 V, a much lower potential than it does on pure Pt. So on PtRu alloy surface, the two binding species can co-exist and react at a

lower potential (~ 0 V) than they do on Pt surface (~ 0.3-0.4 V). Compared with PtRu black, the HB Pt_3Ru shows more negative oxidation peak and higher oxidation current density (1.7 times that of PtRu black). The better performance of Pt_3Ru over PtRu black possibly originates from the morphological factor because the HB morphology increases the chance for methanol to be adsorbed next to a O-binding Ru sites. For instance, methanol and O species adsorbed on different branches have the chance to react due to the small steric spacing between the branches, while the commercial PtRu black (See Fig. 6.2) has an aggregated structure where this mechanism does not apply. We therefore infer that the morphological factor contributes to the catalytic activity of the HBNPs. For Pt_4Ru HBNP, the oxidation current density starts to fall compared with Pt_3Ru because fewer surface Ru sites are available for the adsorption of oxygen species, limiting the number of occuring oxidation reactions per unit surface area. It is generally accepted that for PtRu alloy, when Pt/Ru ratio is closer to 1, electro-catalytic activity for methanol oxidation is higher. However, the PtRu black with 50% Ru (atomic%) shows oxidation current densities lower than that of HB Pt_3Ru.

To confirm the morphological advantage of the HBNPs, irregular (IR) PtRu NPs were also synthesized, named as IR $Pt_{1.2}Ru$ and $Pt_{1.8}Ru$ NPs. IR $Pt_{1.2}Ru$ nanoparticles were synthesized by adding 100 μL of 40 mM $NaBH_4$ solution into 3.9 mL mixed solution with 0.4mM K_2PtCl_4, 0.6 mM $RuCl_3$ and 25 μg/mL S7 peptide. Irregular $Pt_{1.8}Ru$ nanoparticles were synthesized by adding 100 μL of 40 mM $NaBH_4$ solution into 3.9 mL mixed solution with 0.6 mM K_2PtCl_4, 0.4 mM $RuCl_3$ and 25 μg/mL S7 peptide. TEM images of the IR PtRu NPs were shown in Fig. 6.13.

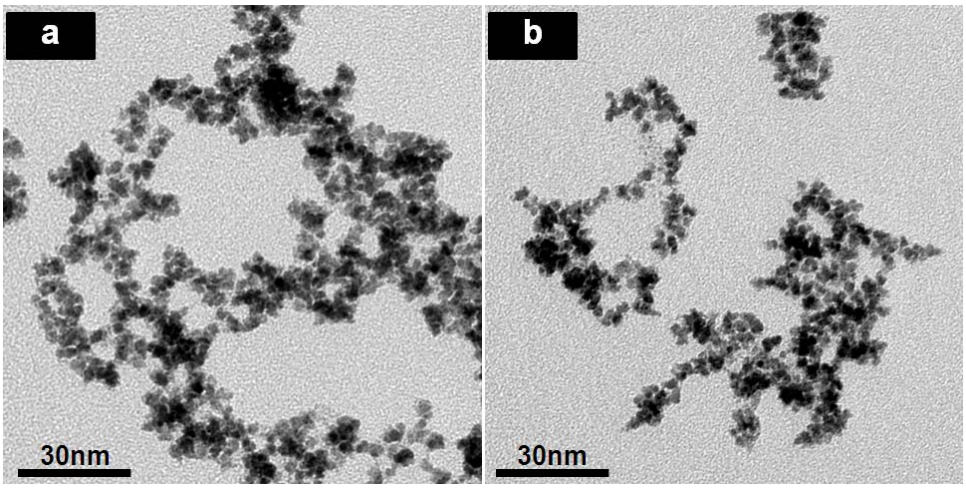

Figure 6.13 (a) and (b) are TEM images of as-synthesized IR $Pt_{1.2}Ru$ and $Pt_{1.8}Ru$ NPs, both of which show irregular shapes.

IR $Pt_{1.2}Ru$ and $Pt_{1.8}Ru$ NPs were tested for methanol oxidation with curves shown in Fig. 6.14. Even though the IR $Pt_{1.2}Ru$ and $Pt_{1.8}Ru$ NPs have Pt/Ru ratio closer to 1, oxidation current densities are lower than those of Pt_3Ru and Pt_4Ru HBNPs, implying the unique advantage of HB morphology over IR NPs with current density enhancement up to 3 folds.

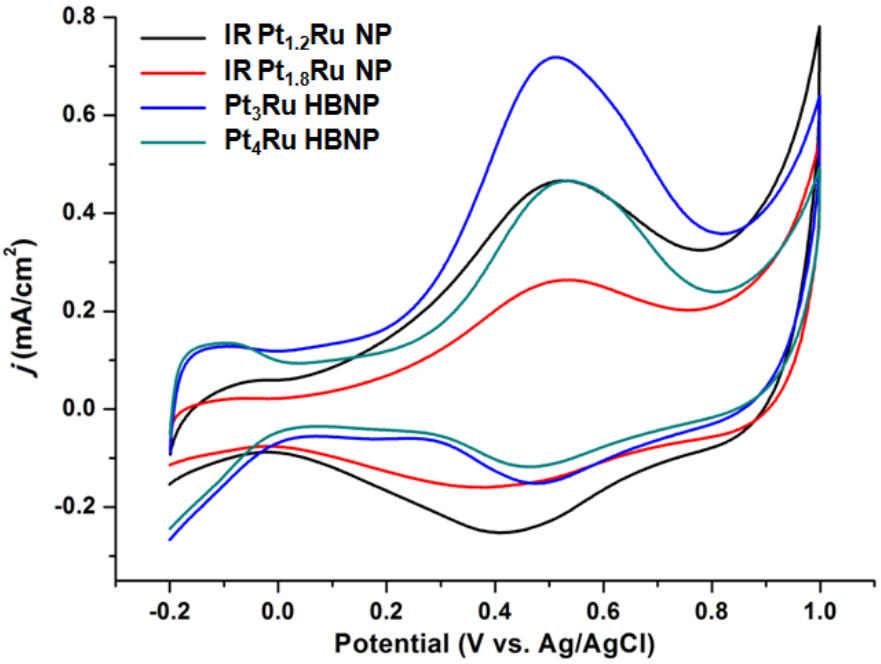

Figure 6.14 CV curves of IR $Pt_{1.2}Ru$ and $Pt_{1.8}Ru$ NPs, compared with Pt_3Ru and Pt_4Ru HBNPs.

6.4 Conclusion

In summary, this work introduces a low-temperature seed-mediated synthesis approach to hyperbranched PtRu NPs. The alloying degree in the NPs is high and the element distribution in NPs is uniform. The reaction pathway of Ru^{3+} to Ru^0 involves the intermediate Ru^{2+} and the elemental ratio can be controlled based on this mechanism. Due to the HB morphological advantage, as well as the existence of high-index facets exposed on HBNPs the activity for electro-oxidation of methanol can be enhanced compared with commercial PtRu black.

[References/Bibliography]

(1) Petrii, O. A. *J Solid State Electr* **2008**, *12*, 609.

(2) Croy, J. R.; Mostafa, S.; Hickman, L.; Heinrich, H.; Cuenya, B. R. *Appl Catal A-gen* **2008**, *350*, 207.

(3) Habas, S. E.; Lee, H.; Radmilovic, V.; Somorjai, G. A.; Yang, P. *Nature Materials* **2007**, *6*, 692.

(4) Wang, D.; Peng, Q.; Li, Y. *Nano Research* **2010**, *3*, 574.

(5) Kang, Y.; Murray, C. B. *J Am Chem Soc* **2010**, *132*, 7568.

(6) Wang, F.; Li, C.; Sun, L.-D.; Wu, H.; Ming, T.; Wang, J.; Yu, J. C.; Yan, C.-H. *J Am Chem Soc* **2011**, *133*, 1106.

(7) Bao, Z.; Sun, Z.; Xiao, M.; Chen, H.; Tian, L.; Wang, J. *J Mater Chem* **2011**, *21*, 11537.

(8) Gasteiger, H. A.; Markovic, N.; Ross, P. N.; Cairns, E. J. *Journal of Physical Chemistry* **1993**, *97*, 12020.

(9) Tong, Y. Y.; Kim, H. S.; Babu, P. K.; Waszczuk, P.; Wieckowski, A.; Oldfield, E. *J Am Chem Soc* **2002**, *124*, 468.

(10) Kaiser, J.; Colmenares, L.; Jusys, Z.; Mortel, R.; Bonnemann, H.; Kohl, G.; Modrow, H.; Hormes, J.; Behm, R. J. *Fuel Cells* **2006**, *6*, 190.

(11) Wang, H. S.; Alden, L. R.; DiSalvo, F. J.; Abruna, H. D. *Langmuir* **2009**, *25*, 7725.

(12) Garcia, G.; Florez-Montano, J.; Hernandez-Creus, A.; Pastor, E.; Planes, G. A. *J Power Sources* **2011**, *196*, 2979.

(13) Iwasita, T.; Hoster, H.; John-Anacker, A.; Lin, W. F.; Vielstich, W. *Langmuir* **2000**, *16*, 522.

(14) Watanabe, M.; Motoo, S. *J Electroanal Chem* **1975**, *60*, 259.

(15) Watanabe, M.; Uchida, M.; Motoo, S. *J Electroanal Chem* **1987**, *229*, 395.

(16) Nashner, M. S.; Frenkel, A. I.; Adler, D. L.; Shapley, J. R.; Nuzzo, R. G. *J Am Chem Soc* **1997**, *119*, 7760.

(17) Pan, C.; Dassenoy, F.; Casanove, M. J.; Philippot, K.; Amiens, C.; Lecante, P.; Mosset, A.; Chaudret, B. *J Phys Chem B* **1999**, *103*, 10098.

(18) Bock, C.; Paquet, C.; Couillard, M.; Botton, G. A.; MacDougall, B. R. *J Am Chem Soc* **2004**, *126*, 8028.

(19) Liu, Z. F.; Ada, E. T.; Shamsuzzoha, M.; Thompson, G. B.; Nikles, D. E. *Chem Mater* **2006**, *18*, 4946.

(20) Lee, S. A.; Park, K. W.; Kwon, B. K.; Sung, Y. E. *J Ind Eng Chem* **2003**, *9*, 63.

(21) Kawaguchi, T.; Sugimoto, W.; Murakami, Y.; Takasu, Y. *J Catal* **2005**, *229*, 176.

(22) Liu, Z. L.; Lee, J. Y.; Chen, W. X.; Han, M.; Gan, L. M. *Langmuir* **2004**, *20*, 181.

(23) Kang, Y. O.; Choi, S. H.; Gopalan, A.; Lee, K. P.; Kang, H. D.; Song, Y. S. *J Appl Polym Sci* **2006**, *100*, 1809.

(24) Vinodgopal, K.; He, Y. H.; Ashokkumar, M.; Grieser, F. *J Phys Chem B* **2006**, *110*, 3849.

(25) Alayoglu, S.; Nilekar, A. U.; Mavrikakis, M.; Eichhorn, B. *Nature Materials* **2008**, *7*, 333.

(26) Guo, D. J.; Zhao, L.; Qiu, X. P.; Chen, L. Q.; Zhu, W. T. *J Power Sources* **2008**, *177*, 334.

(27) Chen, T. Y.; Lin, T. L.; Luo, T. J. M.; Choi, Y.; Lee, J. F. *Chemphyschem* **2010**, *11*, 2383.

(28) Bernechea, M.; Garcia-Rodriguez, S.; Terreros, P.; de Jesus, E.; Fierro, J. L. G.; Rojas, S. *Journal of Physical Chemistry C* **2011**, *115*, 1287.

(29) Teng, X.; Maksimuk, S.; Frommer, S.; Yang, H. *Chem Mater* **2007**, *19*, 36.

(30) Chiu, C.-Y.; Li, Y.; Ruan, L.; Ye, X.; Murray, C. B.; Huang, Y. *Nature Chemistry* **2011**, *3*, 393.

(31) Kim, J.; Rheem, Y.; Yoo, B.; Chong, Y.; Bozhilov, K. N.; Kim, D.; Sadowsky, M. J.; Hur, H.-G.; Myung, N. V. *Acta Biomaterialia* **2010**, *6*, 2681.

(32) Srivastava, S.; Samanta, B.; Arumugam, P.; Han, G.; Rotello, V. M. *J Mater Chem* **2007**, *17*, 52.

(33) Klug, H. P.; Alexander, L. E. *X-Ray Diffraction Procedures: For Polycrystalline and Amorphous Materials*; Wiley-VCH: Weinheim, 1974.

(34) Ciacchi, L. C.; Pompe, W.; De Vita, A. *J Phys Chem B* **2003**, *107*, 1755.

(35) Harpeness, R.; Peng, Z.; Liu, X. S.; Pol, V. G.; Koltypin, Y.; Gedanken, A. *J Colloid Interf Sci* **2005**, *287*, 678.

(36) Dasgupta, M.; Mahanti, M. K. *Transit Metal Chem* **1987**, *12*, 433.

(37) Green, C. L.; Kucernak, A. *J Phys Chem B* **2002**, *106*, 1036.

Chapter 7

7 STABILIZATION OF HIGH PERFORMANCE ORR PT ELECTROCATALYST SUPPORTED ON REDUCED GRAPHENE OXIDE (RGO)/CARBON BLACK (CB) COMPOSITE

7.1 Introduction

Precious-metal-group (PMG) nanocrystals (NCs) have served so far as the most potential cathode electro-catalysts in proton exchange membrane (PEM) fuel cell.[1] Synthesis of highly active PMG nanocatalysts is intriguing chemists in the past decade.[2-5] To make the most use of the precious metal and lower the cost of fuel cells, PMG NCs are usually loaded on high surface area supporting materials.[6] Carbon-based materials have been widely used as supporting material for PMG catalysts.[7-12] The activity and durability of carbon-supported PMG NCs in the oxygen reduction reaction (ORR) occurring at fuel cell cathode, are of great concern to both industry and academia.[6] So far, high surface area carbon black, carbon nanotube, highly oriented pyrolytic graphite (HOPG), etc., have been systematically studied as ORR catalyst supports.[13-16] Recently, graphene (or reduced graphene oxide, i.e. RGO) attracts attention as an unique two-dimensional material with good conductivity, high surface area and high mechanical strength, all of which meet the requirements of a good electro-catalyst support.[17] Therefore, intensive effort has been placed on using RGO as catalyst support for the ORR and some exciting results have been reported.[18-27]

However, due to the nature of the two-dimensional material, RGO sheets tend to stack together through π-π interaction when they are dried, even when they are loaded

with NCs.[22] The stacking blocks substantial amount of catalytic sites on NCs, and sets higher resistance for the diffusion of reactant molecules, which retards the catalytic reaction. Various reported work on RGO-supported ORR catalyst show retarded oxygen reduction rates at certain potential range and slowed down oxygen diffusion.[18,28,29] In addition, RGO sheets obtained by wet chemical synthesis approach usually contain more defects, which reduces the electron transfer rate in the graphene sheet and across the NC-RGO interface as well.[30] So far, little efforts have been made to address this issue and to prevent the stacking of RGO sheets as the support.[31,32]

Herein, we report an approach to design highly active and durable ORR catalyst by loading Pt NCs on primary support RGO and then mixing with secondary support high surface area carbon black (CB). By inserting carbon black particles between the Pt/RGO sheets, the composite structure not only enhances the catalytic activity, but also dramatically improves the durability of the catalyst.

7.2 Experimental

7.2.1 Synthesis of Pt NCs

The Pt NCs were synthesized with a protocol developed in our lab. 20 mL of the precursor solution was prepared with final concentrations of H_2PtCl_6 at 1.5 mM, sodium citrate at 0.5 mM, and a water-soluble aromatic molecule at 1 mg/mL in ultra-pure water (18 MΩ, Millipore).[1] The precursor solution was then heated to 85 ^oC within 10 minutes and maintained at 85 ^oC for 5 minutes before the reaction. A fresh stock solution of 120 mM $NaBH_4$ was prepared and 0.5 mL of the $NaBH_4$ solution was injected into the precursor solution. The reaction solution was kept being stirred at 85 ^oC for 1 hour. The reaction solution was cooled to room temperature. Size and morphology of the NCs were

analyzed with Phillips CM120 TEM operated at 120 kV, and high resolution TEM with FEI TITAN at 300 kV. Scanning electron microscopic (SEM) images were taken on a JEOL JSM-6700F with field emission gun. The weight concentration of the Pt NCs in solution was estimated with inductively coupled plasma optical emission spectrometry (ICP-OES). 1 mL of the reaction solution was taken out and centrifuged at 14000 rpm. The precipitated Pt NCs was collected for ICP-OES measurement which can be used to estimate the weight concentration of Pt NCs in reaction solution.

7.2.2 Preparation of catalyst

Commercial Pt/C catalysts (HiSPEC^{TM}3000, 20 w.t.% Pt on Vulcan XC72R carbon) purchased from Johnson Matthey (JM) was used as baseline catalyst for comparison.

7.2.2.1 Preparation of Pt/RGO and Pt/CB catalysts

10 mL of isopropanol (IPA) was mixed with 10 mL of the pristine Pt NCs solution. The mixed solution was sonicated for 5 minutes. To make the Pt/RGO catalyst (Pt:RGO=1:2), expected amount of graphene sample were dissolved, sonicated and dispersed well in 5 mL of IPA. The Pt NC solution and the RGO solution were then mixed and sonicated for 30 minutes in ice water bath. The catalyst solution was stirred overnight, then centrifuged at 8000 rpm to collect the catalyst, and washed with water for 2 times, acetone for 2 times and then IPA for 2 times. For home-made Pt/CB catalyst, procedures were the same except that the mass ratio Pt/CB is 1/4. The final loading of Pt on carbon (i.e. mass ratio) is determined by thermogravimetric analysis (TGA). The catalyst powders, obtained by freeze drying, were heated from 50 ^{o}C to 600 ^{o}C at the rate of 10 ^{o}C/minute in air.

7.2.2.2 Preparation of the Pt/RGO/CB catalyst

CB was initially washed with IPA for 3 times, and dissolved in IPA at 4 mg/mL, and then sonicated for 30 minutes. Pre-obtained Pt/RGO catalyst (dissolved in IPA, 0.1 mg/mL) was mixed with CB solution. Proper volumes of CB solution were used to achieve Pt/RGO/CB with different RGO/CB ratios. Mixed solution was initially sonicated for 30 minutes to disperse the CB and Pt/RGO, and then stirred overnight to load the CB on Pt/RGO. The solution was then centrifuged (8000 rpm) and re-dissolved (by 30 seconds of sonication) in IPA for further use. In this study, RGO/CB with mass ratios of 1/1 (termed as Pt/RGO/CB-1, the 1/1 ratio is only counted between RGO and CB masses, not Pt/RGO and CB) and 2/1 (Pt/RGO/CB-2) were prepared and compared.

7.2.2.3 Preparation of the Pt/RGO/CB-M catalyst

CB was initially washed with IPA for 3 times, and dissolved in IPA at 4 mg/mL, and then sonicated for 5 minutes. Pre-obtained Pt/RGO catalyst (dissolved in IPA, 0.1 mg/mL) was mixed with CB solution. Proper volume of CB solution was used to achieve RGO/CB ratio to be 1/1. The mixed solution was agitated with simple vortex for 1 minute (to avoid the formation of well-composited structure). The solution was then centrifuged (8000 rpm) and re-dissolved (by 30 seconds of sonication) in IPA for further use.

7.2.2.4 Preparation of the JM Pt/C/RGO catalyst

10 mg of JM Pt/C catalyst was dissolved in 4 mL of H_2O/IPA (4/1) mixed solvent. The solution was sonicated for 30 minutes and stored as JM Pt/C stock solution. RGO solution (1 mg/mL in IPA) containing 8 mg RGO, and 0.5 mL of 20 mM sodium chloride solution (in H_2O) were added into the JM Pt/C stock solution. The mixed solution was sonicated for 30 minutes, and then stirred overnight. JM Pt/C/RGO was centrifuged,

washed with water for 3 times, then with IPA for 3 times, and re-dispersed in 10 mL IPA for further use.

7.2.2.5 Preparation of the JM Pt/C/CB catalyst

10 mg of JM Pt/C catalyst was dissolved in 4 mL of H_2O/IPA (4/1) mixed solvent. The solution was sonicated for 30 minutes as JM Pt/C stock solution. CB solution (1 mg/mL in IPA) containing 8 mg CB, were added into the JM Pt/C stock solution. The mixed solution was sonicated for 30 minutes, and then stirred overnight. JM Pt/C/CB was centrifuged, washed with IPA for 3 times, and re-dispersed in 10 mL IPA for further use.

7.2.3 Electrochemical measurement

According to the Pt weight concentrations determined by ICP-OES, all catalyst solutions (in IPA) were diluted to the same Pt concentration at0.3 mg/mL. 1 μL 5% Nafion solution was added into 100 μL catalyst solution and the solution was sonicated for 1 minutes. 9 μL catalyst solution was drop-casted on glassy carbon electrode (GCE, Pine Instrumentation) with electrode area of 0.196 cm^2 and dried in vacuum. The final Pt loading of all made-in-house catalysts was 13.8 $\mu g/cm^2$. The same procedure as described above was used for JM Pt/C except that the final Pt loading was 20.4 $\mu g/cm^2$. The catalyst film was checked with optical microscopy to confirm it is uniform. Ag/AgCl (3 M Cl^-) was used as reference electrode and Pt wire was used as counter electrode. All electrochemical data were captured in 0.1 M $HClO_4$ electrolyte. ECSA were calculated by integrating the hydrogen adsorption charges in cyclic voltammetry (CV). The ADTs were scanned between 0.6 and 1.1 V (all potentials are referenced to reversible hydrogen electrode (RHE)) in electrolyte exposed to atmosphere up to 20000 cycles and CV curves were recorded every 4000 cycles.

After ADT, electrodes were sonicated in IPA to collect the catalysts. Before making the TEM samples, the IPA solutions containing the catalysts were sonicated for enough time (varying between 10 and 30 minutes) to allow the catalysts to be fully dispersed in IPA. TEM samples were prepared by casting the catalyst-containing IPA solutions onto TEM grids and drying in the air.

7.3 Results and discussions

7.3.1 Preparation of catalysts

Pt NCs were synthesized in aqueous solution at 85 ^{o}C. The transmission electron microscopic (TEM) image of the as-synthesized water-soluble Pt NCs is shown in Fig. 7.1. Over 80% of the NCs show cuboctahedral morphology with uniform size. The average size is 5 nm with deviation lower than 5%. The high resolution image in Fig. 7.1(b) shows that the as-synthesized Pt NCs are single crystalline.

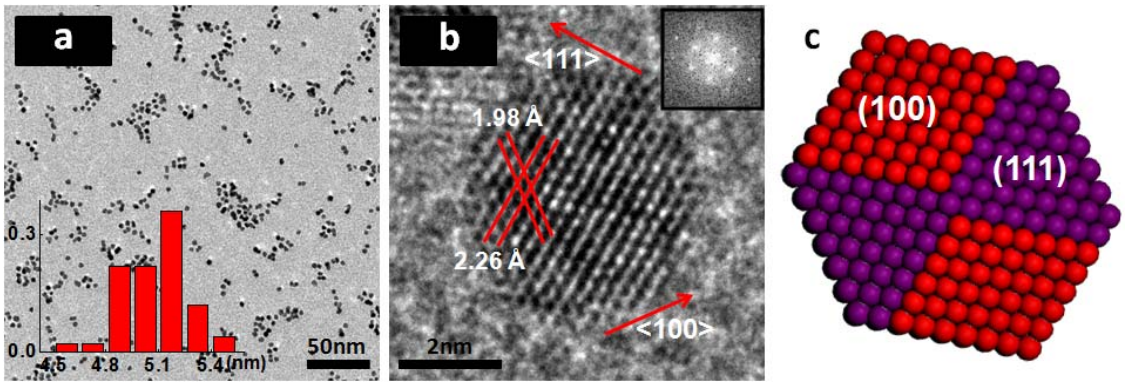

Figure 7.1 (a) TEM image of as-synthesized Pt NCs. Inset: Statistical analysis of the size based on 100 randomly picked NCs. (b) High resolution TEM image showing the lattice of the NC. Inset: Fast Fourier transform from the <110> zone axis. (c) Schematic of a constructed cuboctahedral NC with (100) and (111) facets highlighted.

The weight concentration of the Pt NCs in solution was measured by inductively coupled plasma optical emission spectrometry (ICP-OES) to estimate the amount of carbon materials needed in order to achieve expected Pt/Carbon ratio. Pt NCs loaded on different types of supports are shown in Fig. 7.2. On RGO, the Pt loading ratio is 33 wt% (referred to total mass). The TEM image shows that Pt NCs were loaded uniformly on RGO without obviously localized aggregation. RGO was obtained by hydrazine reduction of graphene oxide synthesized by Hummer's method.[33,34] Pt/RGO/CB composite was prepared by mixing Pt/RGO with CB in IPA and stirring overnight. According to Fig. 7.2(c) which is the typical view under TEM, all Pt-loaded RGO sheets form composites with CB particles. We note that no bare Pt/RGO sheets or bare CB without NCs were observed under TEM, indicating well-mixed nature of the composite. Besides, most Pt NCs were still attached on RGO, indicating that the contact between Pt NCs and the RGO is good. As a comparison, TEM images of Pt NCs directly loaded on CB were shown in Fig. 7.2(e,f). It can be inferred that there is obvious difference of how Pt NCs are located on Pt/CB from that of Pt NCs on the Pt/RGO/CB. Two types of Pt/RGO/CB catalysts were prepared with RGO/CB (Note: not the ratio between Pt/RGO and CB) mass ratio of 1/1 (termed as Pt/RGO/CB-1) and 2/1 (Pt/RGO/CB-2). The loading ratio of Pt on Pt/RGO/CB-1 shown in Fig. 7.2(c,d) is 22 wt%, Pt on Pt/RGO/CB-2 is 26 wt%, and Pt on home-made (HM) Pt/CB is 21 wt%, determined by thermal gravimetric analysis (TGA).

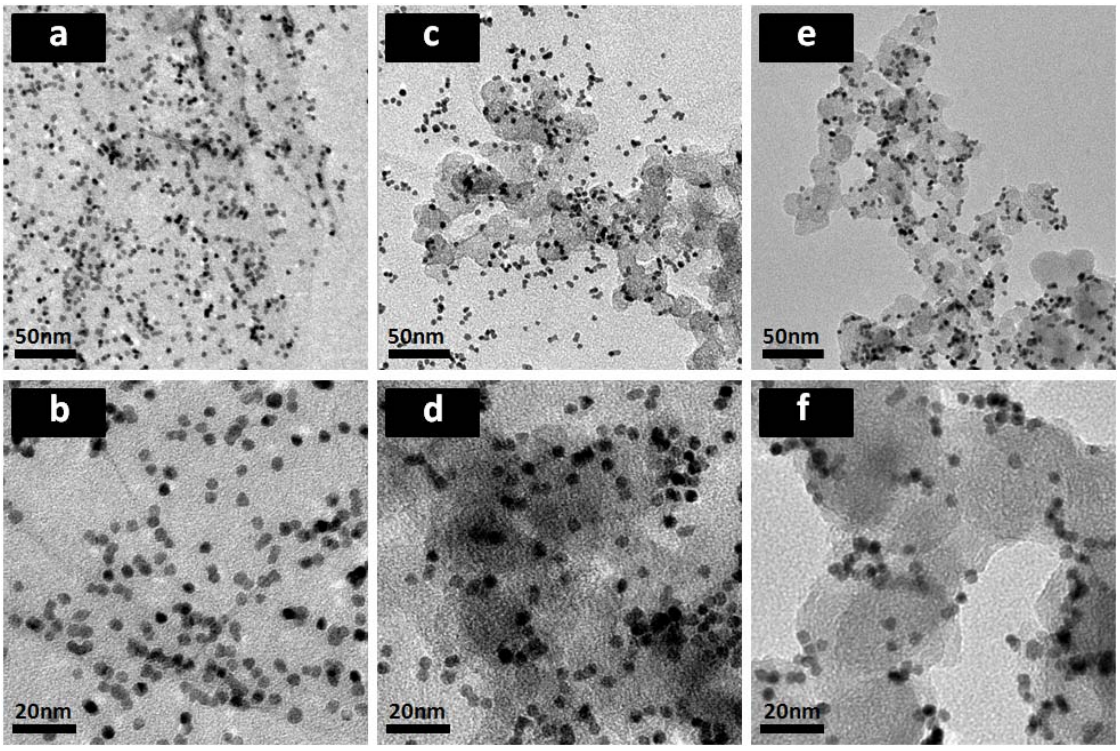

Figure 7.2 TEM images of (a,b) Pt NCs loaded on RGO, (c,d) Pt/RGO mixed with carbon black (Pt/RGO/CB-1), (e,f) Pt NCs loaded only on carbon black.

7.3.2 Electrochemical characterization of the catalysts

Electrochemical measurement was carried out to observe the effect of CB insertion on ORR. The loading of Pt on glassy carbon electrode (GCE) was controlled at 13.8 μg/cm^2 for all catalyst samples with home-made Pt NCs. Commercial Pt/C catalysts (20 w.t.% Pt on Vulcan XC72R carbon) obtained from Johnson Matthey (JM) was used as baseline catalyst for comparison, and is termed JM Pt/C. Due to the difficulty of making uniform catalyst film with JM Pt/C at the same loading amount, the loading of the baseline catalyst JM Pt/C was controlled at 20.4 μg/cm^2. After the electrode was fully activated with cyclic voltammetry (CV) scans between 0 and 1.0 V (vs. reversible hydrogen electrode (RHE)), the stable CV curves were recorded and compared in Fig. 7.3(a). All CV curves were normalized by corresponding electrochemical surface areas (ECSAs)

calculated by integrating hydrogen adsorption charges.[35] The specific ECSAs of these catalysts were measured to be 60.1, 57.0, 56.4, 50.0 m^2/g for home-made Pt/CB, Pt/RGO, Pt/RGO/CB-1 and Pt/RGO/CB-2, compared with 58.9 m^2/g for JM Pt/C.

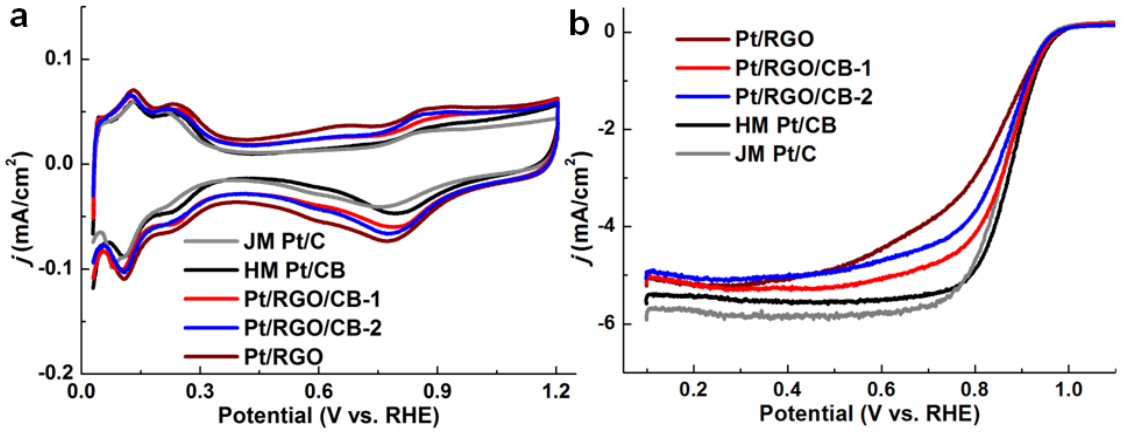

Figure 7.3 (a) CV curves, and (b) polarization curves for home-made Pt/CB, Pt/RGO, JM Pt/C, Pt/RGO/CB-1 and -2.

Polarization curves in O_2-saturated $HClO_4$ electrolyte were recorded on rotating disk electrode (RDE) at the rotating rate of 1600 rpm, normalized with area of the GCE (0.196 cm^2), shown in Fig. 7.3(b). Compared with HM Pt/C catalyst, Pt/RGO shows much lower current density at 0.9 V, indicating that the kinetic current is lower when Pt NCs are loaded on RGO. In addition, the diffusion-limiting potential region (where current is stabilized as a plateau) is shorter for Pt/RGO catalyst, meaning that its kinetic current drops faster with elevating potential. However, for the HM Pt/CB catalyst, the current at mixed kinetic-diffusion control region (between 0.80 and 0.95 V) is higher than commercial catalyst. All the above information indicates that the RGO-supported Pt NCs shows lower ORR activity than Pt NCs on CB, and that pure RGO inhibits the oxygen reduction rate. This is partly due to the fact that when Pt/RGO catalyst was dried, RGO sheets tend to form closely-packed film, which inhibits the diffusion of O_2 through the

film to approach the Pt surface and thus lowers the reduction rate on Pt NCs.[36] The stacking of the Pt-loaded RGO can be observed through scanning electron microscopic (SEM) images shown in Fig. 7.4(c,d). Interestingly, when CB is well mixed with Pt-loaded RGO sheets as a secondary support, currents can be dramatically promoted between 0.6 and 0.9 V, indicating that the ORR activity can be recovered. This is due to the fact that the inserted CB particles enlarged the gaps between RGO sheets which provides enough space for fast oxygen diffusion through the film, and enhances the oxygen supply in the film, accelerating the reduction rate. The structure of the well-mixed composite is shown in Fig. 7.5, in which the Pt-loaded RGO sheet highlighted with yellow circle is sandwiched by CB particles (highlighted with black circle). Comparing the polarization curves of Pt/RGO/CB-1 and Pt/RGO/CB-2 samples, it can be seen that when more CB is added, the ORR activity can be further enhanced and more space is created, confirming the proposed inhibition mechanism of RGO and the recovering mechanism by adding CB.

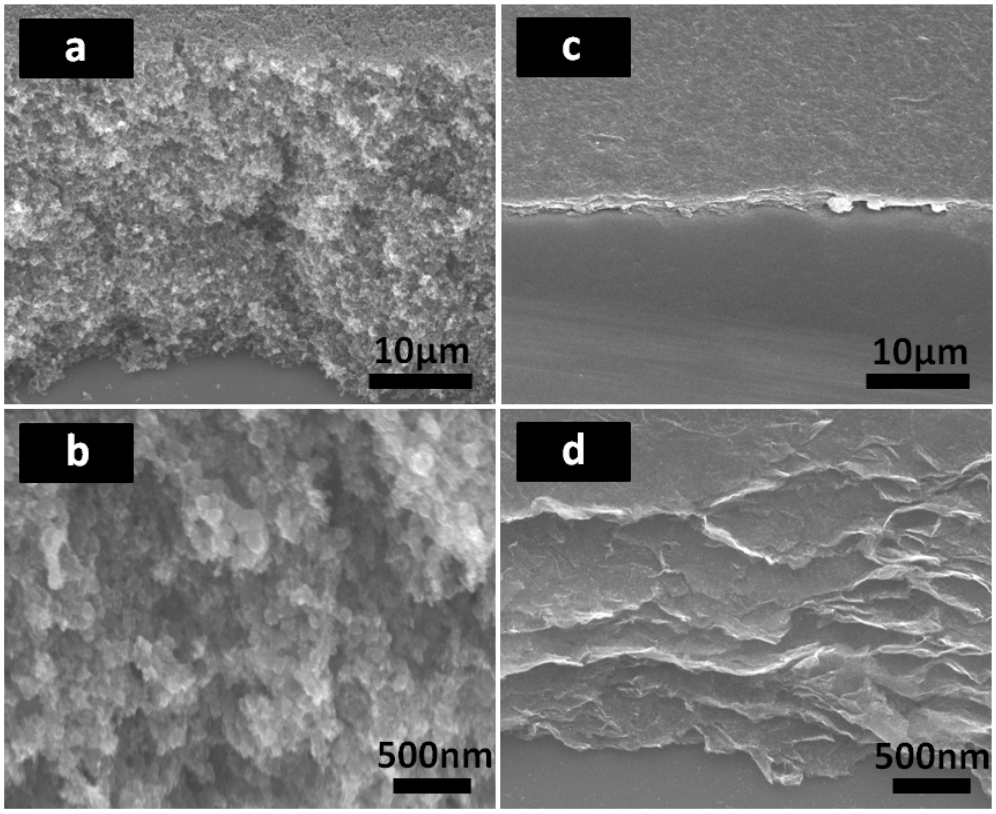

Figure 7.4 (a,b) and (c,d) are scanning electron microscopic (SEM) images of home-made Pt/CB and Pt/RGO catalysts. Catalyst films were made by drop-casting catalyst solution on SiO_2.

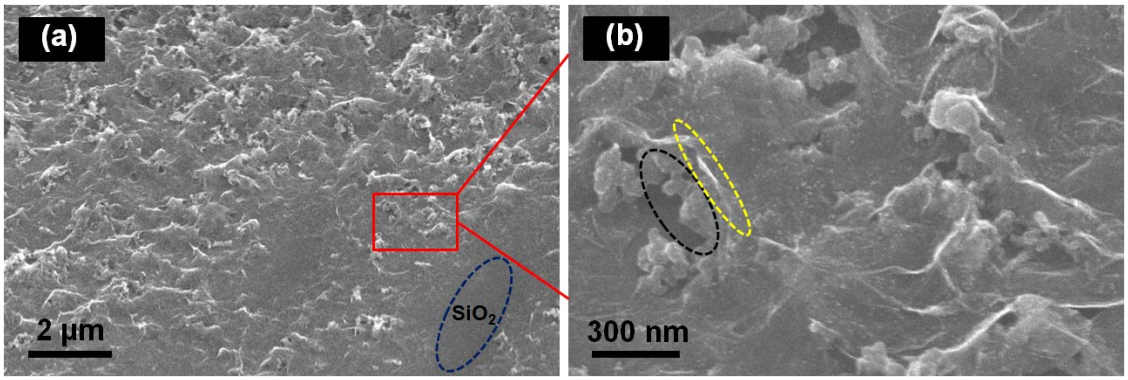

Figure 7.5 (a, b) are SEM images of cross-section of Pt/RGO/CB-1 catalyst film. Catalyst films were made by drop-casting catalyst solution on SiO_2. Yellow dashed circle

in (b) highlights the edge of the Pt-loaded RGO sheet. Black dashed circle highlights the CB particles.

7.3.3 ADT measurement

ADT was carried out to test the durability of the catalysts. Potential was cycled between 0.6 and 1.1 V in 0.1 M $HClO_4$ which was exposed to the atmosphere. CV curves between 0 and 1.1 V were recorded every 4000 cycles in order to compare the change of ECSAs during the potential cycling. Fig. 7.6 (a) and (b) show the evolutions of CV curves for Pt/RGO/CB-1 and Pt/RGO/CB-2, with the change of JM Pt/C shown in Fig. 7.6(c) as a comparison. The similar curves for HM Pt/CB, and Pt/RGO are shown in Fig. 7.7. It is observed that the ECSA of JM Pt/C drops to almost 60% of its initial surface area after the first 4000 ADT cycles, but the loss slows down and the final ECSA after 20000 cycles stabilizes at around 51% of the initial value, consistent with previously reported results (Fig. 7.6(d)).[37] For HM Pt/CB catalyst, the ECSA slowly drops to 60%, which is slightly better than the commercial JM Pt/C catalyst. The Pt/RGO retains only 46% of its initial ECSA. However, the Pt/RGO/CB-2 sample shows the improvement on ECSA loss, with 87% of the initial ECSA remained. With higher amount of CB addition, the Pt/RGO/CB-1 sample retains more than 95% of its initial ECSA.

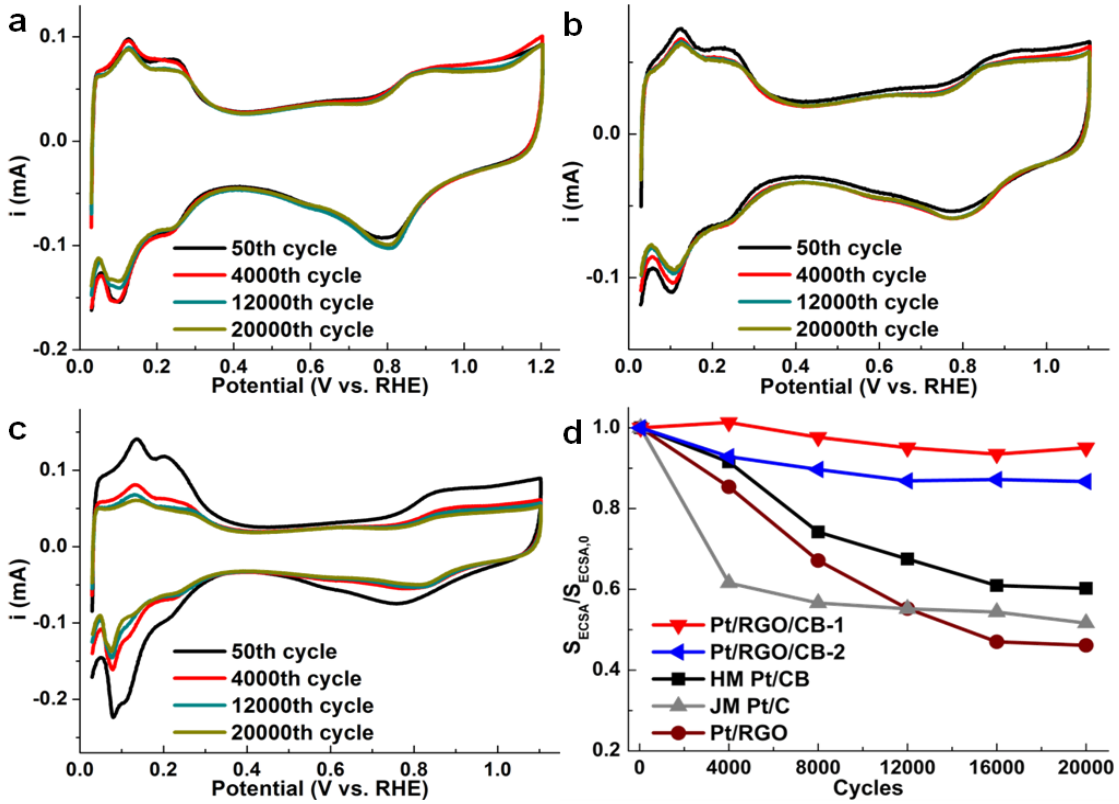

Figure 7.6 CV curves of 50, 4000, 12000 and 20000 cycles for (a) Pt/RGO/CB-1, (b) Pt/RGO/CB-2, and (c) JM Pt/C. (d) Comparison of ECSA loss for different materials. $S_{ECSA,0}$ stands for the initial ECSA of the corresponding catalyst.

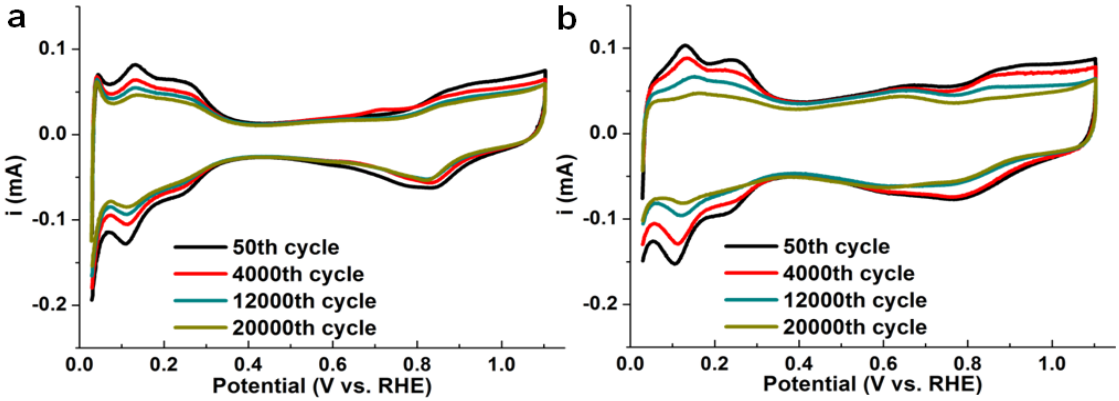

Figure 7.7 CV curves of 50, 4000, 12000 and 20000 cycles for (a) Home-made Pt/CB, (b) Pt/RGO.

ORR activities after the 20000 cycles of ADT were also measured for all samples in O_2-saturated $HClO_4$ electrolyte. Fig. 7.8(a) shows the polarizations curves for home-made Pt/CB, Pt/RGO, Pt/RGO/CB-1, and JM Pt/C catalysts. As comparisons, polarization curves before the ADT were shown in solid curves, and after the ADT shown in dashed curves. In the mixed kinetic-diffusion control region, it is obvious that the polarization curves of the Pt NCs on CB or RGO only, show more obvious current drop after the ADT, while there is almost no change for the Pt/RGO/CB-1 sample which is supported on the RGO/CB composite support. To illustrate the effect of CB amount added into the Pt/RGO catalyst, Fig. 7.8(b) shows the comparisons of Pt/RGO/CB-1 and Pt/RGO/CB-2 with JM Pt/C, indicating the better performance of Pt/RGO/CB-1 and Pt/RGO/CB-2 over the commercial JM Pt/C catalyst.

Activities were calculated as a quantitative comparison to illustrate the superior performance of Pt/RGO/CB catalysts. Mass-transport-corrected kinetic current at 0.9 V was calculated according to the Levich−Koutecký equation: $1/i=1/i_k+1/i_d$, where i_k is the kinetic current and i_d is the diffusion-limiting current.[38] As shown in Fig. 7.8(c), after the ADT, the specific activities of Pt/RGO/CB-1 and Pt/RGO/CB-2 samples at 0.9 V are 0.212 and 0.200 mA/cm^2 respectively, almost twice that of commercial JM Pt/C catalyst (~0.106 mA/cm^2), and higher than those supported only on CB or RGO. In terms of mass activity, the Pt/RGO/CB-1 sample retains at 0.109 A/mg after ADT, slightly higher than the activity of Pt/RGO/CB-2 sample, and almost triples the final mass activity of the commercial JM Pt/C after ADT (0.031 A/mg). Both Pt/RGO/CB samples show significantly smaller change in activities than that of the commercial catalyst, indicating the obvious enhancement effect on catalyst durability when inserting CB into Pt/RGO.

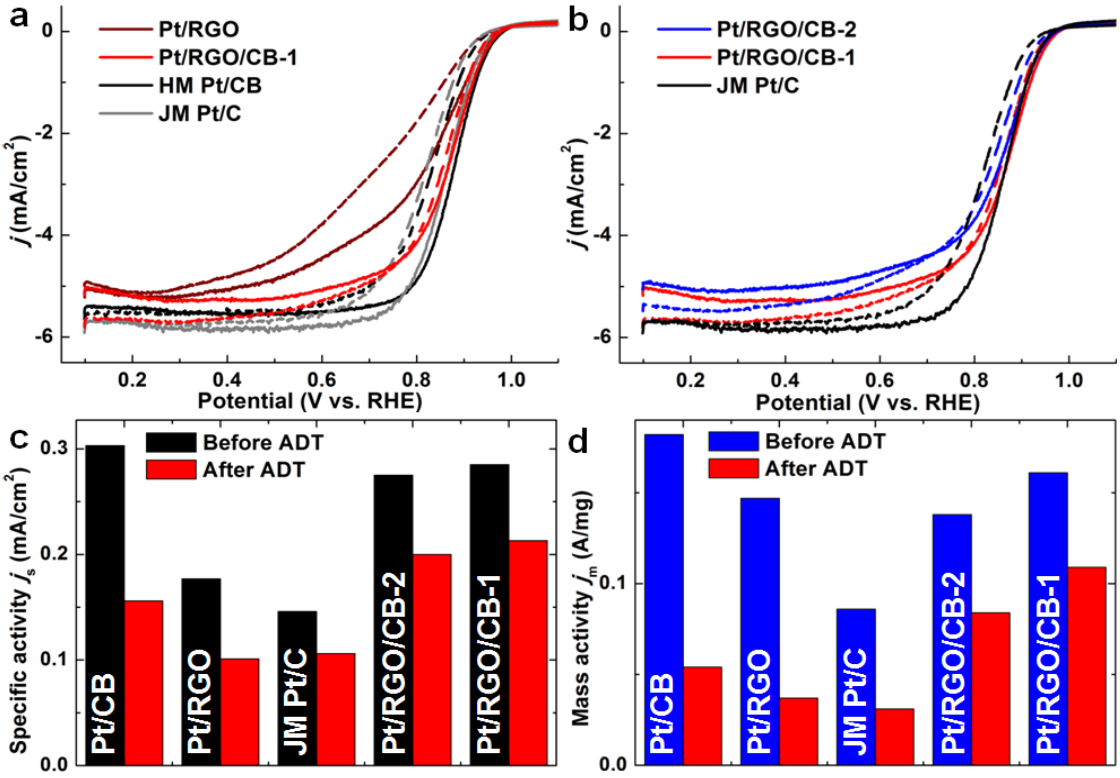

Figure 7.8 (a) Polarization curves of Pt/CB, Pt/RGO, JM Pt/C, and Pt/RGO/CB-1 before (solid curve) and after (dashed curve) the ADT. (b) Polarization curves of Pt/RGO/CB-1 and -2 with comparison of JM Pt/C before (solid) and after (dashed) the ADT. (c) and (d) are specific activities and mass activities at 0.9V for different materials.

7.3.4 Mechanism study

To reveal the mechanism of the durability enhancement observed, catalysts were collected by sonicating the GCE in IPA after the ADT and their structures were observed by TEM. TEM images of as-prepared home-made Pt/CB and Pt/RGO (Fig. 7.9(a, b) and (d, e)), and Fig. 7.9 (c, f) show the statistical analyses of the Pt NC sizes after the ADT test. In general the Pt NCs grow obviously in size through Ostwald ripening. The average size is ~9.75 nm for Pt/CB, and ~10.92 nm for Pt/RGO, compared to ~5nm before the ADT, and both with much wider size distributions.

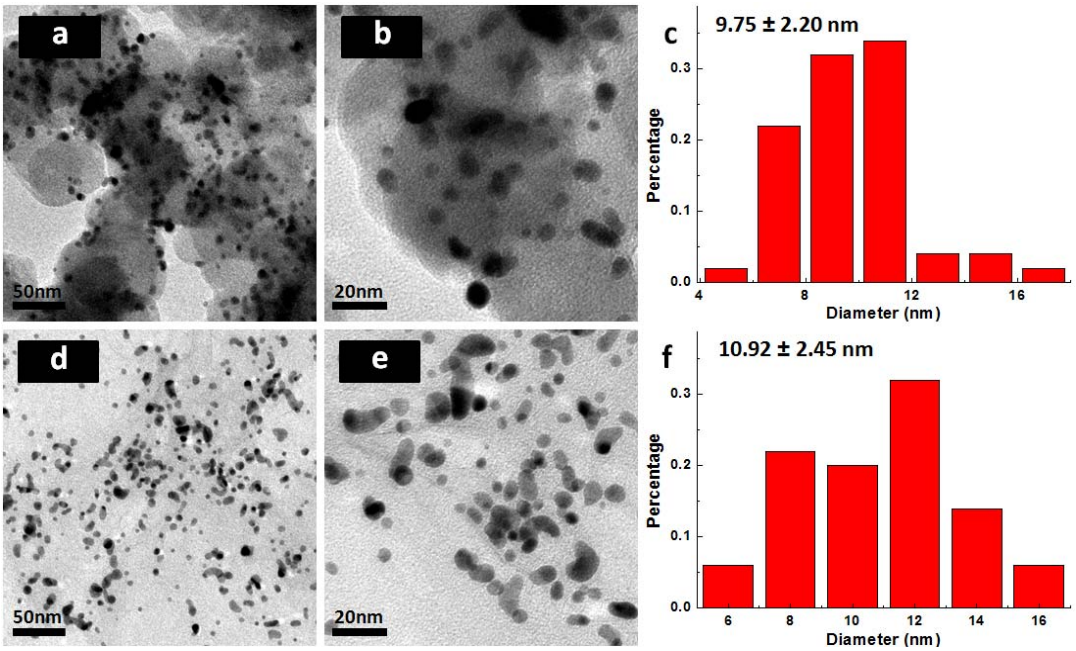

Figure 7.9 (a,b) TEM images and (c) Histogram of statistical analysis of Pt particle size (based on 100 randomly picked particles) of Pt/CB collected from electrode after ADT. (d,e) TEM images and (f) Histogram of statistical analysis of Pt particle size of Pt/RGO collected from electrode after ADT.

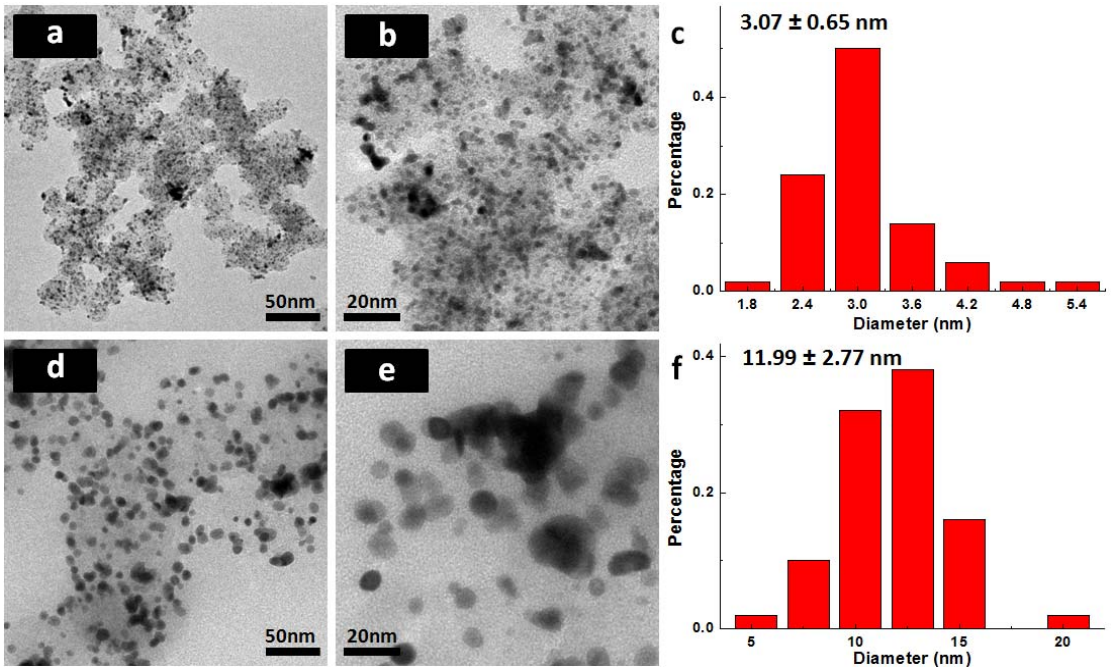

Figure 7.10 JM Pt/C catalyst (a,b) before and (d,e) after the ADT. (c) and (f) are histogram of statistical analysis of Pt particle size of JM Pt/C before and after ADT.

The commercial JM Pt/C catalysts grow in size from around ~3 nm to ~12 nm after the ADT as shown in Fig. 7.10. This is consistent with the observed obvious decrease in ECSA for these catalysts.

However, in the Pt/RGO/CB samples, after the ADT, we found a significant portion of Pt NCs are attached onto CB while all NCs are on RGO before the ADT. Interestingly, the size distributions of Pt NCs on CB and on RGO are distinctively different. Fig. 7.11(a, c) show the typical Pt NCs supported on CB and on RGO respectively, from Pt/RGO/CB-1 after ADT.

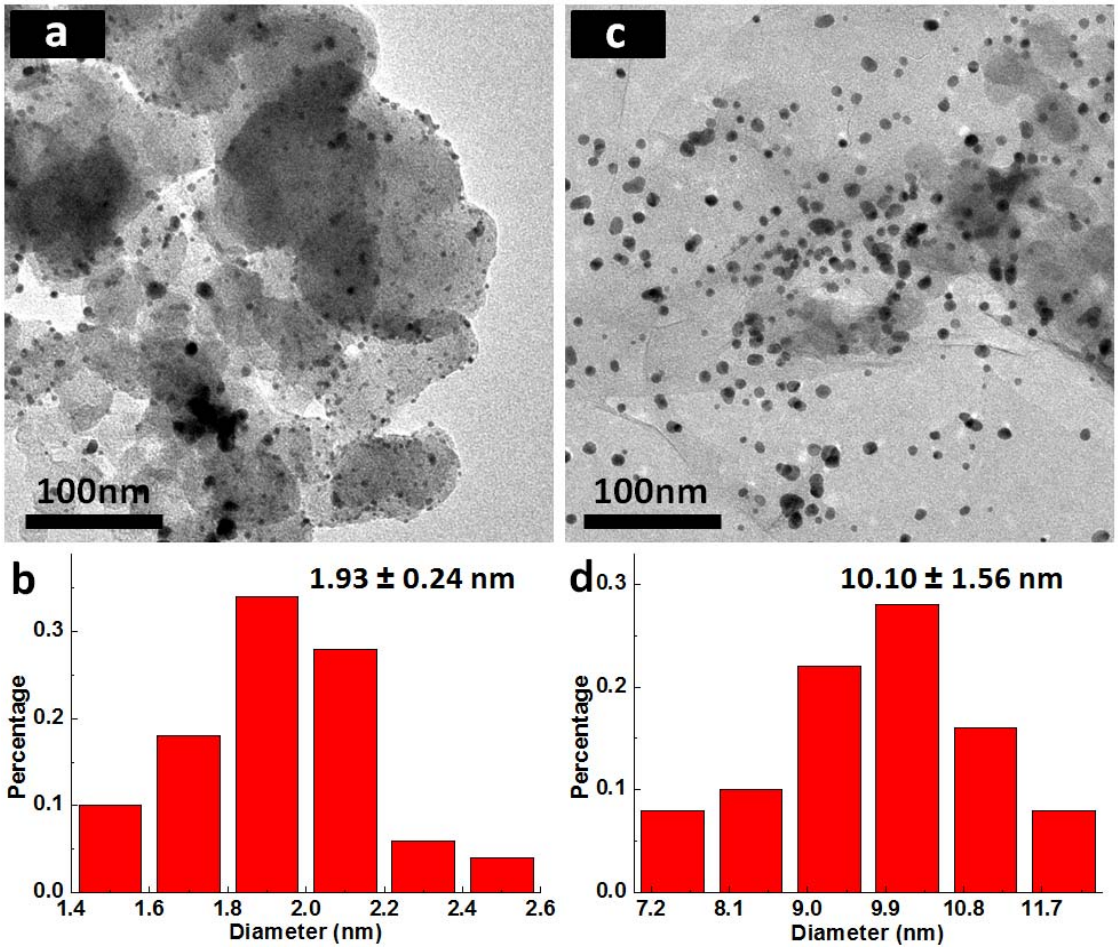

Figure 7.11 (a, c) TEM image of Pt particles supported on CB and on RGO respectively, from collected Pt/RGO/CB-1 after ADT. They are captured in different regions from the same TEM sample. (b, d) Statistical analyses of Pt sizes supported on CB and on RGO, respectively as shown in (a, c).

It is observed that the size of NCs attached on CB (~1.93 nm) is obviously smaller than those on RGO sheets (~10.10 nm). It is interesting that the NCs attached on CB are much smaller than the initial Pt NCs loaded on RGO sheets (~5 nm). We hence suggest that while the Pt NCs on RGO sheets experience Ostwald ripening as did those on the regular samples, the dissolved Pt species or clusters during the ripening process can be

recaptured or can renucleate on the CB in the hybrid support structure. It has been reported that the migration of Pt atoms or clusters on carbon surface depends strongly on the surface heterogeneity, which means that defects or kinks on the surface can serve as heterogeneous nucleation sites.[39,40] Compared with smooth graphitized surface, CB is richer in kinks and traps, which provides more nucleation sites for migrating Pt species (atoms or clusters) and re-collects more Pt species which will otherwise combine into larger particles or dissolve into the electrolyte. So CB is potentially more capable of capturing more surface area after the ADT. This is consistent with our results that the loss of Pt ECSA is lower on HM Pt/CB than on Pt/RGO (Fig. 7.6(d)). In the Pt/RGO/CB, on one hand, the CB can capture and provide nucleation sites for the migrating Pt species generated from dissolution of Pt NCs (which is induced by Ostwald ripening) on RGO. On the other hand, the RGO sheets, with its 2D nature, can possibly act as a "mesh bag" to prevent the Pt species from leaking into the electrolyte, providing them more opportunity to be captured or to be renucleated on the CB component. This synergetic process leads to the creation of many ultrasmall Pt NCs on CB surface, which in turn counteract the decreased Pt surface area induced by Pt ripening and dissolution. Hence we observed a sharp decrease in the total loss of ECSA for Pt/RGO/CB samples.

With the proposed mechanism, the high durability of the Pt/RGO/CB composite catalysts can be readily understood. The mechanism are further confirmed by control experiments with two additional types of catalyst prepared by (1) mixing JM Pt/C catalyst with RGO, name as JM Pt/C/RGO, and (2) mixing JM Pt/C catalyst with CB, with details included in SI (termed as JM Pt/C/CB). The final ECSA of JM Pt/C/RGO after 20000 cycles of ADT can be retained over 80% (as shown in Fig. 7.12) of the initial

ECSA, much higher than that of the JM catalyst (51%) and JM Pt/C/CB (47%). It confirms that the existence of RGO plays an important role in enhancing the durability, and that this hybrid support structure can be broadly applicable to commercial catalytic products.

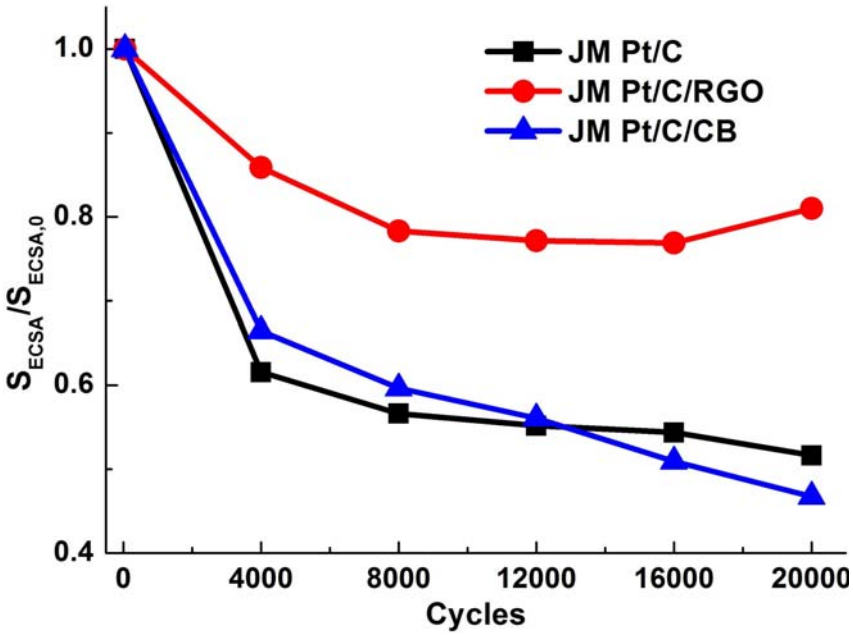

Figure 7.12 Comparison of the ECSA change vs. number of cycles relationships for JM Pt/C, JM Pt/C/RGO, and JM Pt/C/CB. $S_{ECSA,0}$ stands for the initial electrochemical surface area before ADT of corresponding materials.

Another catalyst structure, prepared by randomly mixing Pt/RGO and CB without the sonication and stirring process (termed as Pt/RGO/CB-M, as shown in Fig. 7.13) was used to confirm the effect of well-composited structure between Pt/RGO and CB. Fig. 7.14 shows that the final ECSA of Pt/RGO/CB-M decreased to ~60% of the initial value, much worse than that of Pt/RGO/CB-1 (95%), indicating that the well-mixed RGO/CB composite structure is critical to achieving greatly enhanced durability. The above two sets of comparison are consistent with the proposed mechanism.

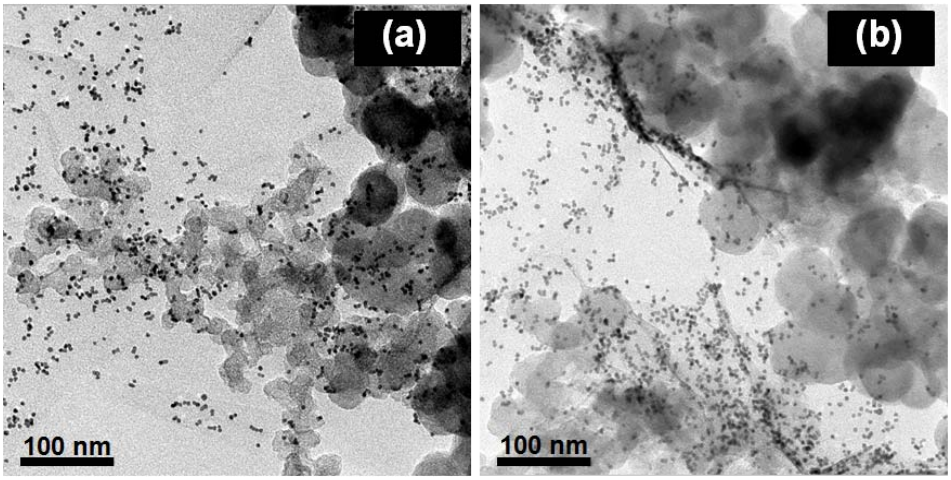

Figure 7.13 (a) and (b) are typical TEM images of Pt/RGO/CB-1 and Pt/RGO/CB-M, respectively. In Pt/RGO/CB-1 (a), CB particles disperse well on Pt-loaded RGO sheets. But in Pt/RGO/CB-M (b), Pt-loaded RGO sheets tend to fold and attach on aggregated CB particles.

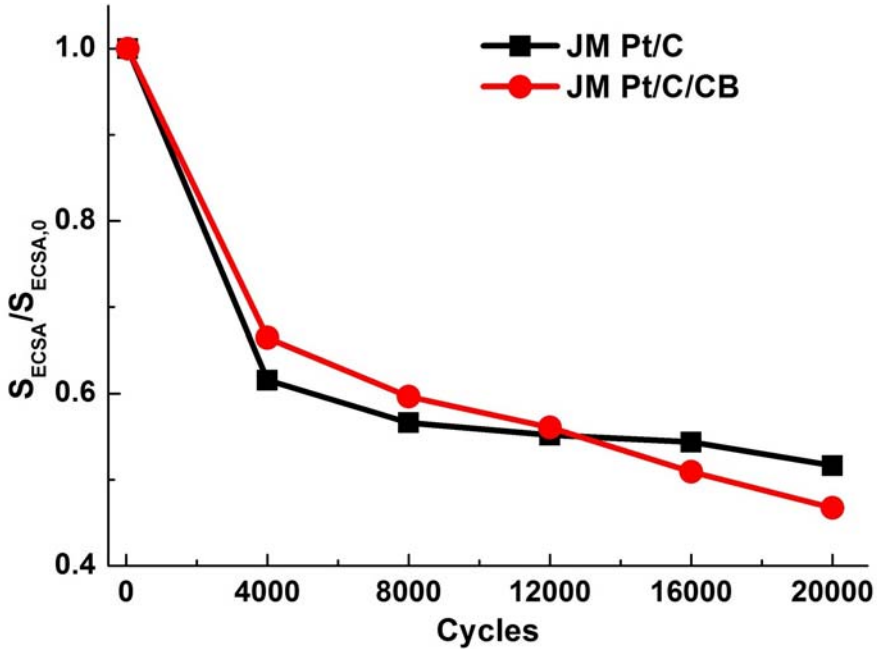

Figure 7.14 Comparison of ECSA change vs. number of cycles relationships for Pt/RGO/CB-1 and Pt/RGO/CB-M. $S_{ECSA,0}$ stands for the initial electrochemical surface area.

7.4 Conclusion

As a summary, we have successfully demonstrated that the composite catalytic structure Pt/RGO/CB shows greatly enhanced ORR activity compared to Pt/RGO structure in 0.1 M $HClO_4$. Importantly, ADT shows that the Pt/RGO/CB only lost 5% of the ECSA after up to 20000 cycles' test, while the commercial JM Pt/C catalyst lost almost 50% of ECSA after the same number of cycling. In addition the ORR mass activity of the Pt/RGO/CB catalyst after the ADT is 2 times higher than that the of the commercial JM Pt/C catalyst. TEM observations combined with electrochemical measurements suggest that in the hybrid structure, the flexible 2D profile of RGO may function as a "mesh" that prevents leaching of dissolved Pt species into the electrolyte, while the CBs can serve as active site for re-capture or renucleation of small Pt clusters. These studies confirm the determining role of the RGO/CB hybrid structure in enhancing the catalyst durability. More importantly we have further demonstrated that the proposed working mechanism of the hybrid catalytic structure can be successfully applied to the commercial JM Pt/C product, which shows again greatly enhanced durability. This particular catalyst design approach can be used to prepare high performance and durable fuel cell catalysts.

[References/Bibliography]

(1) Gasteiger, H. A.; Markovic, N. M. *Science* **2009**, *324*, 48.

(2) Peng, Z.; Yang, H. *Nano Today* **2009**, *4*, 143.

(3) Li, Y.; Whyburn, G. P.; Huang, Y. *J. Am. Chem. Soc.* **2009**, *131*, 15998.

(4) Chiu, C.-Y.; Li, Y.; Ruan, L.; Ye, X.; Murray, C. B.; Huang, Y. *Nat. Chem.* **2011**, *3*, 393.

(5) Ruan, L.; Chiu, C.-Y.; Li, Y.; Huang, Y. *Nano Lett.* **2011**, *11*, 3040.

(6) Shao, Y.; Liu, J.; Wang, Y.; Lin, Y. *J. Mater. Chem.* **2009**, *19*, 46.

(7) Juntgen, H. *Fuel* **1986**, *65*, 1436.

(8) Huang, X.; Zhao, Z.; Fan, J.; Tan, Y.; Zheng, N. *J. Am. Chem. Soc.* **2011**, *133*, 4718.

(9) Koh, S.; Strasser, P. *J. Am. Chem. Soc.* **2007**, *129*, 12624.

(10) Habas, S. E.; Lee, H.; Radmilovic, V.; Somorjai, G. A.; Yang, P. *Nat. Mater,* **2007**, *6*, 692.

(11) Peng, Z.; Yang, H. *J. Am. Chem. Soc.* **2009**, *131*, 7542.

(12) Zhang, J.; Yang, H.; Fang, J.; Zou, S. *Nano Lett.* **2010**, *10*, 638.

(13) Wu, J.; Zhang, J.; Peng, Z.; Yang, S.; Wagner, F. T.; Yang, H. *J. Am. Chem. Soc.* **2010**, *132*, 4984.

(14) Li, W. Z.; Liang, C. H.; Zhou, W. J.; Qiu, J. S.; Zhou, Z. H.; Sun, G. Q.; Xin, Q. *J. Phys. Chem. B* **2003**, *107*, 6292.

(15) Zhou, Y.; Pasquarelli, R.; Holme, T.; Berry, J.; Ginley, D.; O'Hayre, R. *J. Mater. Chem.* **2009**, *19*, 7830.

(16) Shao, Y.; Sui, J.; Yin, G.; Gao, Y. *Applied Catalysis B-Environmental* **2008**, *79*, 89.

(17) Geim, A. K.; Novoselov, K. S. *Nat. Mater,* **2007**, *6*, 183.

(18) Kou, R.; Shao, Y.; Mei, D.; Nie, Z.; Wang, D.; Wang, C.; Viswanathan, V. V.; Park, S.; Aksay, I. A.; Lin, Y.; Wang, Y.; Liu, J. *J. Am. Chem. Soc.* **2011**, *133*, 2541.

(19) Guo, S.; Sun, S. *J. Am. Chem. Soc.* **2012**, *134*, 4.

(20) Guo, S.; Dong, S.; Wang, E. *Acs Nano* **2010**, *4*, 547.

(21) Yoo, E.; Okata, T.; Akita, T.; Kohyama, M.; Nakamura, J.; Honma, I. *Nano*

Lett. **2009**, *9*, 2255.

(22) Si, Y.; Samulski, E. T. *Chem. Mater.* **2008**, *20*, 6792.

(23) Seo, M. H.; Choi, S. M.; Kim, H. J.; Kim, W. B. *Electrochem. Commun.* **2011**, *13*, 182.

(24) Rao, C. V.; Reddy, A. L. M.; Ishikawa, Y.; Ajayan, P. M. *Carbon* **2011**, *49*, 931.

(25) Kou, R.; Shao, Y.; Wang, D.; Engelhard, M. H.; Kwak, J. H.; Wang, J.; Viswanathan, V. V.; Wang, C.; Lin, Y.; Wang, Y.; Aksay, I. A.; Liu, J. *Electrochem. Commun.* **2009**, *11*, 954.

(26) Liang, Y.; Li, Y.; Wang, H.; Zhou, J.; Wang, J.; Regier, T.; Dai, H. *Nat. Mater,* **2011**, *10*, 780.

(27) Choi, S. M.; Seo, M. H.; Kim, H. J.; Kim, W. B. *Carbon* **2011**, *49*, 904.

(28) Xin, Y.; Liu, J.-g.; Zhou, Y.; Liu, W.; Gao, J.; Xie, Y.; Yin, Y.; Zou, Z. *J. Power Sources* **2011**, *196*, 1012.

(29) Yoo, E.; Okada, T.; Akita, T.; Kohyama, M.; Honma, I.; Nakamura, J. *J. Power Sources* **2011**, *196*, 110.

(30) Gomez-Navarro, C.; Weitz, R. T.; Bittner, A. M.; Scolari, M.; Mews, A.; Burghard, M.; Kern, K. *Nano Lett.* **2007**, *7*, 3499.

(31) Yoo, E.; Kim, J.; Hosono, E.; Zhou, H.-s.; Kudo, T.; Honma, I. *Nano Lett.* **2008**, *8*, 2277.

(32) Park, S.; Shao, Y.; Wan, H.; Rieke, P. C.; Viswanathan, V. V.; Towne, S. A.; Saraf, L. V.; Liu, J.; Lin, Y.; Wang, Y. *Electrochem. Commun.* **2011**, *13*, 258.

(33) Hummers, W. S.; Offeman, R. E. *J. Am. Chem. Soc.* **1958**, *80*, 1339.

(34) Stankovich, S.; Dikin, D. A.; Piner, R. D.; Kohlhaas, K. A.; Kleinhammes, A.; Jia, Y.; Wu, Y.; Nguyen, S. T.; Ruoff, R. S. *Carbon* **2007**, *45*, 1558.

(35) Arenz, M.; Mayrhofer, K. J. J.; Stamenkovic, V.; Blizanac, B. B.; Tomoyuki, T.; Ross, P. N.; Markovic, N. M. *J. Am. Chem. Soc.* **2005**, *127*, 6819.

(36) Yan, J.; Wei, T.; Shao, B.; Ma, F.; Fan, Z.; Zhang, M.; Zheng, C.; Shang, Y.; Qian, W.; Wei, F. *Carbon* **2010**, *48*, 1731.

(37) Zhang, J.; Sasaki, K.; Sutter, E.; Adzic, R. R. *Science* **2007**, *315*, 220.

(38) Lim, B.; Jiang, M.; Camargo, P. H. C.; Cho, E. C.; Tao, J.; Lu, X.; Zhu, Y.; Xia, Y. *Science* **2009**, *324*, 1302.

(39) Ehrburger, P.; Mahajan, O. P.; Walker, P. L. *J. Catal.* **1976**, *43*, 61.

(40) Flynn, P. C.; Wanke, S. E. *J. Catal.* **1974**, *34*, 390.

Chapter 8

8 SUMMARY

8.1 Synthesis and catalysis of Pt-based nanoparticles

With the aim to improve the electrocatalytic activity of Pt based electrocatalysts for oxygen reduction and methanol oxidation in proton exchange membrane fuel cell (PEMFC) and direct methanol fuel cell (DMFC) and to reduce the cost of electrocatalysts, following work, including (1) demonstrate a bimomimetic approach to select material-specific biomolecules as capping agent for the synthesis of Pt nanoparticles, (2) achieve the morphology and size controlled synthesis of Pt nanoparticles, (3) use as-synthesized Pt nanoparticles as starting material for the synthesis of Pt-based bimetallic nanoparticles, (4) improve the electrocatalytic activities of the bimetallic nanoparticles in ORR and methanol oxidation reaction, has been carried out to finally achieve the objective.

To demonstrate the biomimetic approach to select biomolecules specifically binding to target materials and use the biomolecues as stabilizing agent for the nanoparticle synthesis, phage display (PD) technique was used to fulfill the selection process by using Pt as a case study. Peptide molecules were selected and then synthesized with Fmoc solid phase peptide synthesis (Fmoc-SPPS) technique. With specifically selected peptide molecules as stabilizing agent, we have reported the rational synthesis of mono-disperse ultrasmall Pt NCs, in aqueous solution at room temperature,. The selected peptide molecule P7A is able to bind to the Pt NC surface and thus can function as stabilizer to regulate Pt crystal nucleation and growth, and therefore control both the morphology and size of the final Pt NCs. Uniform near-spherical Pt NCs with size from 1.73 to 3.54 nm

were achieved with very narrow size distribution. It has also been demonstrated that peptide can be unbound from the NC surface by simply lowering the pH of the solution or degraded through a photolysis process.

By modifying the P7A peptide into BP7A with both ends of the peptide molecule blocked, the morphology of the nanoparticles synthesized with BP7A can be tuned. We have demonstrated that the peptide molecules selected with phage display technique could be used to regulate the Pt NC growth kinetics therefore control the resulting NC morphologies in aqueous solution at room temperature. By varying the peptide concentration, nearly spherical Pt NCs and Pt NCs of multipod structures with different pod lengths could be rationally achieved. The shape evolution studies of NCs suggested that the peptide molecules preferably bind onto {110} facets, resulting in multipod structures with preferential pod growth direction along <111> and <100>. It was also demonstrated that the facet-specific selectivity plays a less important role with increasing peptide concentrations, leading to the transformation of multipod to a nearly spherical morphology at high peptide concentrations. The electrochemical study of different shaped Pt NCs showed that the as-synthesized multipod NCs demonstrate high ECSAs and can potentially serve as high performance catalysts in electrocatalytic applications, such as PEM fuel cells. More importantly this study demonstrated a potential pathway to rationally synthesize NCs with selectively exposed facets with specific peptide molecules for the first time, and therefore open up many new opportunities in nanocatalysts design and studies.

With the as-synthesized multipod Pt NCs as core materials, bimetallic PtPd nanoparticles with Pt-Pd core-shell structure can be obtained and their electro-catalytic

activities in ORR and methanol oxidation reaction are enhanced. Pt-Pd core-shell bimetallic NCs with multipod morphologies were synthesized with a two-step protocol in mild aqueous condition, with controllable Pd shell thickness from sub-monolayer to a few atomic layers. The as-synthesized bimetallic NCs demonstrate better performance than the Pt core NCs and commercially available Pt black and Pd black as a cathode catalyst towards ORR, and anode catalyst towards electro-oxidation of methanol fuel molecule in alkaline media. The bimetallic NCs also show better resistance to CO poisoning, which extends the catalyst lifetime. The effect of the Pd shell on the catalytic activity was systematically studied and the best performance was achieved when the Pd/Pt ratio is 1/3, when the Pd shell is close to one atomic monolayer. These studies demonstrated the potential of using Pt-Pd core-shell bimetallic NCs as high-performance catalysts at both electrodes in DMFC. They also demonstrate the importance of Pd shell thickness of the core-shell NCs on modulating the catalytic performance, which can also provide valuable guidelines for designing high-performance catalysts for fuel cell applications.

The biomimetic synthesis of Pt-based bimetallic nanoparticles with peptide molecules is not only limited to those with hybrid structures such as core-shell structure mentioned above, it can also be applied to the synthesis of Pt-based alloy nanoparticles. With S7 peptide which is also selected against Pt surface, more specifically to the nanoparticle surface, PtRu alloy nanoparticles were then studied. We introduces a low-temperature seed-mediated synthesis approach to hyperbranched PtRu NPs. The alloying degree in the NPs is high and the element distribution in NPs is uniform. The reaction pathway of Ru^{3+} to Ru^{0} involves the intermediate Ru^{2+} and the elemental ratio can be controlled based on

this mechanism. Due to the HB morphological advantage, as well as the existence of high-index facets exposed on HBNPs the activity for electro-oxidation of methanol can be enhanced compared with commercial PtRu black.

With the work discussed in this dissertation, the main idea is to demonstrate that the biomimetically selected material-specific peptide molecules can be used to synthesize Pt nanoparticles or Pt-based bimetallic nanoparticles which can be used for the electro-catalysis involved in PEMFC and DMFC. Hopefully with the approach demonstrated, a new protocol can be employed for the low-temperature and 'green' synthesis of noble metal nanoparticles.

8.2 Hybrid support for Pt catalyst

To better incorporate reduced graphene oxide (RGO) into the fuel cell catalyst, an innovative hybrid supporting material was designed and prepared to overcome the stacking issue of RGO and enhance both the activity and durability of graphene-supported catalyst. Oxygen reduction reaction (ORR) catalyst supported by hybrid composite materials is prepared by well-mixing of carbon black (CB) with Pt-loaded RGO. With the insertion of CB particles between RGO sheets, the stacking of RGO can be effectively prevented, which promotes the diffusion of oxygen molecules through the RGO sheets and enhances the electro-catalytic activity in ORR. Importantly, the accelerated durability test (ADT) demonstrates that the hybrid supporting material can dramatically enhance the durability of the catalyst and retain the electrochemical surface area (ECSA) of Pt. The final ECSA of the Pt nanocrystal on the hybrid support after 20000 ADT cycles is shown to be retained at a level higher than 95%, much higher than the commercial available catalyst. We suggest that the unique 2D profile of the RGO

functions as barrier that prevents leaching of Pt into electrolyte and the CB in vicinity acts as active sites to recapture/renucleate the dissolved Pt species. We have furthermore demonstrated that the working mechanism can be successfully applied to the commercial Pt/C product to greatly enhance its durability.

Appendices

Selected publications

1. **Li, Y.**, & Huang, Y., Low-Temperature Seed-mediated Synthesis of Monodispersed Hyperbranched PtRu Nanoparticles and Their Electrocatalytic Activity in Methanol Oxidation, ***Journal of Materials Chemistry***, DOI:10.1039/C2JM30892D (**2012**).

2. **Li, Y.**, Wang, Z., Chiu, C., Ruan, L., Yang, W., Yang, Y., Palmer, R., & Huang, Y., Synthesis of Bimetallic Pt-Pd Core-Shell Nanocrystals and Their High Electrocatalytic Activity Modulated by Pd Shell Thickness, ***Nanoscale***, 4, 845-851 (**2012**).

3. Ruan, L., Chiu, C., **Li, Y.**, & Huang, Y., Synthesis of Platinum Single-Twinned Right Bipyramid and {111}-Bipyramid through Targeted Control over Both Nucleation and Growth Using Specific Peptides, ***Nano Letters***, 11, 3040-3046 (**2011**).

4. Chiu, C., **Li, Y.**, Ruan, L., Ye, X., Murray, C., Huang, Y., Shaping Platinum Nanocrystals with Biomolecular Specificity, ***Nature Chemistry***, 3, 393-399 (**2011**).

5. **Li, Y.**, Chiu, C., & Huang Y., Biomimetic Synthesis of Inorganic Materials and Their Applications, ***Pure and Applied Chemistry***, 83, 111-125 (**2011**).

6. **Li, Y.**, & Huang, Y., Morphology-Controlled Synthesis of Platinum Nanocrystals with Specific Peptides, ***Advanced Materials***, 22, 1921-1925 (**2010**).

7. Chiu, C., **Li, Y.** & Huang, Y., Size-controlled Synthesis of Pd Nanocrystals Using a Specific Multifunctional Peptide, ***Nanoscale***, 2, 927-930 (**2010**).

8. Zhang, H., **Li, Y.**, Ivanov, I., Qu, Y., Huang Y. & Duan, X., Plasmonic Modulation of the Upconversion Fluorescence in NaYF4:Yb/Tm Hexaplate Nanocrystals Using

Gold Nanoparticles or Nanoshells, ***Angewandte Chemie International Edition*** 49, 2865-2868 (**2010**).

9. **Li, Y.**, Whyburn, G., & Huang, Y., Specific Peptide Regulated Synthesis of Ultrasmall Platinum Nanocrystals, ***Journal of the American Chemical Society***, 131, 15998-15999 (**2009**).

10. Wang, L., Bai, J., **Li, Y.**, & Huang, Y., Multifunctional Nanoparticles Displaying Magnetization and Near-IR Absorption, ***Angewandte Chemie International Edition*** 47, 2473-2476 (**2008**).

11. Whyburn, G., **Li, Y.** & Huang, Y., Protein and Protein Assembly Based Material Structures, ***Journal of Materials Chemistry***, 18, 3755-3762 (**2008**).